

Investigating the Performance of Randomly Patterned Superhydrophobic Surfaces in Laminar  
and Turbulent Channel Flows

By

Daren Wilkinson

A thesis submitted in partial fulfillment of the requirements for the degree of

Master of Science

Department of Mechanical Engineering  
University of Alberta

© Daren Wilkinson, 2018

# Abstract

Superhydrophobic surfaces (SHSs) have been investigated based on their success in water repellency, anti-fouling, and drag reducing effects seen in nature (Neinhuis & Bartlott 1997; Kreuz *et al.* 2001). SHSs utilize a low surface energy material with a microscale surface roughness to prevent water from entering cavities between the roughness elements. When a SHS is exposed to a liquid, the cavities remain filled with air, described as the air layer, which inhibits the droplet from achieving a wetted state on the surface. When exposed to flows, the water-air interface is shear-free, thus lowering the skin-friction compared to a smooth surface. Due to the number of different possible surface geometries and roughness as well as different flow characteristics, a relationship between the SHS performance and the flow parameters has not fully modeled. SHS performance characteristics include slip velocity, slip length, and drag reduction. This study aimed to finish characterizing the trend between a previously studied SHSs and the flow conditions, as well as characterize a SHS and determine its performance at a certain flow condition.

The first part of the study focused on a commercially available spray coating NeverWet (Rustoleum) which has previously been studied by Aljallis *et al.* (2014), Zhang *et al.* (2015), and Abu Rowin *et al.* (2017). The surfaces were tested in a laminar channel with 180 mm length ( $L$ ), 20 mm width ( $W$ ), and 2 mm height ( $H$ ) at bulk Reynolds numbers ( $Re_b$ ) ranging from 50-450. The drag reducing capabilities at different flow conditions were measured through a 2D shadowgraphic particle tracking velocimetry (shadow-PTV) setup. There was a linear trend between slip velocity,  $u_s$ , and  $Re_b$  determined to be  $u_s = 0.077Re_b$  up to a  $Re_b$  of 250. The surfaces showed a maximum drag reduction of 16%. The 2D shadow-PTV measurements at  $Re_b > 250$  showed a decrease in the SHS performance with the lowest being a drag reduction of 11%. The decrease in the SHS performance was attributed to a combination of the low hydrostatic pressure and the high  $Re_b$ . This agrees with the experiment of Gose *et al.* (2018) when suggested that pressures below atmospheric extract the air layer away from the surface. With gauge pressures below atmospheric and higher streamwise velocities, portions of the air layer can detach from the surface. It was believed that after  $Re_b = 250$ , the channel pressure and the flow conditions allowed for partial detachment of the air layer and therefore a reduction in the SHS performance. The slip length measurements also confirm this trend as they remained the same at  $71 \mu\text{m} \pm 1 \mu\text{m}$  while at  $Re_b = 450$  the slip length decreased to  $48.8 \mu\text{m} \pm 0.3 \mu\text{m}$ .

The second part of this study focused on comparing the performance of four randomly patterned SHSs with a varying surface roughness in turbulent channel flow. Characterizations of the surface topography through a scanning electron microscope and surface roughness through profilometer were performed. Based on their roughness value normalized by the inner scaling,  $k^+_{\text{rms}}$ , the surfaces were referred to as SHS<sub>0.35</sub>, SHS<sub>0.23</sub>, SHS<sub>0.18</sub>, and SHS<sub>0.14</sub>. The surfaces had dimensions of  $234 \times 36 \text{ mm}^2$  ( $L \times W$ ) and were tested in a closed loop channel with a rectangular cross-section of  $40 \times 6 \text{ mm}^2$  ( $W \times H$ ) and a length of 1200 mm. The  $Re_b = 8000$  flow was captured utilizing a planar micro-PTV setup operated over 6 seconds at a rate of 10 kHz. The 2D-PTV measurement showed that the normalized slip velocity by the inner scaling,  $u_s^+$ , was positively related to the surface roughness with a second-order power relationship found,  $u_s^+ = 0.051/(k^+_{\text{rms}})^2$ . It was observed that  $u_s^+$  increased exponentially with the decrease of the surface roughness. This trend was also consistent with the drag reduction measurement which was obtained from the reduction of the velocity gradient. The drag reduction over the SHSs started as the highest at 21% over SHS<sub>0.35</sub> and reached a drag increase of 19% over SHS<sub>0.14</sub>. Therefore, the drag reduction and the slip boundary condition over the SHS depends on the surface roughness where the large posts of the surface can disturb the shear-free regions and results in loss of the performance as suggested by the simulation of Alame & Mahesh (2018).

# Preface

The work of this thesis was completed under the supervision of Dr. Sina Ghaemi and Dr. Dan Sameoto from the Department of Mechanical Engineering at the University of Alberta.

The experimental setup described in chapter 3.1 was developed under the supervision of Dr. Sina Ghaemi and the experimental setup described in Chapter 3.2 was developed by Wagih Abu Rowin (PhD. student at the time) and Sina Rafiti (PhD. student at the time) under the supervision of Dr. Sina Ghaemi.

The four surfaces used in the turbulent channel experiments as described in Chapter 3.2.1 were fabricated by Abhijeet and Venkata Srikrishna Pillutla under the supervision of Dr. Wonjae Choi at the University of Texas at Dallas.

# Acknowledgements

I would like to thank Dr. Sina Ghaemi and Dr. Dan Sameoto for the opportunity to pursue my interests in academia and more importantly for their guidance and wisdom.

I am grateful for the unconditional love, support, and encouragement from my mother, father, and brother throughout my endeavors.

I also want to express my sincere gratitude towards Rafat Jami, David Serrano, Wagih Abu Rowin, Asad Asad, and Mohammad Elyasi who helped me with my research, but more importantly, in maintaining a balance between school and non-academic life. Without them I would not have been able to succeed in my work.

I would also like to thank all my friends, both old and new, for giving me the opportunity to relax when life became overwhelming.

Lastly, I am thankful for the unconditional help from the members in my research group who provided guidance and assistance throughout my work.

# Table of Contents

1	Introduction.....	1
1.1	Background .....	1
1.2	Project objectives .....	2
1.3	Outline.....	2
2	Literature review.....	4
2.1	Channel flow and terminology.....	4
2.2	Laminar flows .....	5
2.2.1	Governing equations.....	6
2.3	Turbulent flows .....	8
2.3.1	Governing equations.....	9
2.4	Drag reduction with superhydrophobic surfaces.....	13
2.4.1	Contact angle and contact angle hysteresis.....	14
2.4.2	Slip over a surface.....	16
2.4.3	Superhydrophobic surfaces.....	17
2.4.4	Estimation of drag.....	21
2.5	Measurement methods.....	26
2.5.1	Micro particle tracking velocimetry (Micro-PTV) and shadowgraphic particle tracking velocimetry (Shadow-PTV).....	26

2.5.2	Recording devices and lenses .....	29
2.5.3	Light sources and timing.....	31
2.5.4	Image quality .....	32
3	Experimental setups .....	33
3.1	Laminar flow loop setup .....	33
3.1.1	Pumping system .....	34
3.1.2	Measurement channel .....	36
3.1.3	Leakage prevention.....	40
3.1.4	Shadow-PTV.....	41
3.1.5	Surface fabrication and characterization.....	44
3.2	Turbulent flow loop.....	47
3.2.1	Turbulent channel .....	48
3.2.2	Particle tracking velocimetry .....	50
3.2.1	Surface fabrication and characterization.....	54
4	Measurement uncertainty .....	58
4.1	Wall location method for shadow-PTV .....	58
4.2	Wall location method for time-resolved PTV .....	59
4.3	Measurement uncertainties.....	60
4.3.1	Uncertainties in particle velocity .....	61

4.3.2	Uncertainty in particle position and measurement time .....	67
4.4	Repeatability of the laminar flow loop.....	68
5	Laminar channel flow over a randomly textured superhydrophobic surface .....	70
5.1	Introduction .....	70
5.2	Results and discussion.....	70
6	Turbulent channel flow over randomly patterned superhydrophobic surfaces with varying roughness .....	75
6.1	Introduction .....	75
6.2	Measurement over the smooth surface.....	75
6.3	Measurement over the superhydrophobic surfaces .....	77
7	Conclusions.....	82
7.1	Recommendations for future work.....	83
	References.....	84
8	Appendix A – Laminar channel drawing package.....	93
9	Appendix B – Other works .....	111
9.1.1	Superhydrophobic surfaces.....	111
9.1.2	Turbulent statistics analysis .....	112



# List of Figures

Figure 1: An illustrated example of channel flow with dimensions. ....	5
Figure 2: An illustrated image of laminar flow in a channel depicting the boundary layer growth. .....	5
Figure 3: An illustrated image of turbulent channel flow depicting the boundary layer growth and the three regimes of boundary layer.....	8
Figure 4: The relationship between turbulent kinetic energy and Reynolds stresses normalized by friction velocity against $y^+$ from DNS turbulent channel flow at $Re= 6666$ (Kasagi et al. 1993). .	9
Figure 5: A graphical comparison showing the relationship of $u^+$ to $y^+$ for turbulent flow.....	13
Figure 6: An image of a 30 $\mu$ L water droplet on (a) a smooth polystyrene surface with a contact angle of $86^\circ$ and (b) a SHS showing a contact angle of $153^\circ$ . ....	14
Figure 7: An illustration showing a droplet in the (a) Wenzel state and (b) Cassie-Baxter state.	15
Figure 8: An illustration of measuring contact angle hysteresis using an inclined plane. ....	16
Figure 9: An illustration showing the effect a patterned surface with low surface energy has on the liquid-solid boundary. ....	18
Figure 10: A schematic illustrating the principles of particle tracking velocimetry. ....	26
Figure 11: An illustration of the top view of a basic shadow-PTV setup.....	27
Figure 12: An illustration showing diffraction effects during imaging of particles. ....	30
Figure 13: A timing diagram of events for a typical PTV system capturing image pairs. ....	32

Figure 14: An image of the experimental setup for the testing of superhydrophobic surfaces in a laminar flow.....	33
Figure 15: An illustrated image of the channel and encompassing assemblies.....	34
Figure 16: An annotated image of the syringe pump used to drive the laminar channel flow. ....	35
Figure 17: An annotated image of the operational components controlling the syringe pump. ....	36
Figure 18: An annotated image of the channel assembly. ....	37
Figure 19: (a) Dimensioned front view of the channel. (b) Dimensioned top view of the channel. .....	38
Figure 20: A cross sectional image of the surface holding assembly used in the channel. ....	40
Figure 21: An image of calibration using the calibration target for the Shadow-PTV setup. ....	43
Figure 22: An image of the contact angle between a 10 $\mu$ L water droplet and the SHS.....	45
Figure 23: (a) SEM imaging of the SHS viewed at a magnification of 100 times showing the surface topography. (b) The SHS at a magnification of 250 times showing the particle size of the NW second coat.....	46
Figure 24: An illustration of the turbulent channel closed loop system used for testing SHSs....	47
Figure 25: An exploded view of the channel portion from the closed-loop turbulent setup. ....	48
Figure 26: Dimensioned illustration of the channel portion from the closed-loop turbulent setup. .....	49
Figure 27: An exploded view of the upstream chamber used to remove large eddies. ....	49
Figure 28: A picture of the high-speed camera and optical attachments.....	50

Figure 29: An illustration of the optics used to redirect and reform the laser beam into a laser sheet for turbulent flow characterization with a micro PTV setup. .... 51

Figure 30: (a) An unprocessed image of turbulent flow over the smooth surface. (b) The image after improvement of signal to noise ratio to be used by the PTV algorithm. .... 52

Figure 31: Profilometer measurements of the (a) SHS<sub>0.35</sub>, (b) SHS<sub>0.23</sub>, (c) SHS<sub>0.18</sub>, and (d) SHS<sub>0.14</sub> surface with their respective  $R_a$ ,  $R_{rms}$ , and  $R_{mean}$  values added for reference. .... 55

Figure 32: Top down SEM images at a magnification of 250 of (a) SHS<sub>0.35</sub>, (b) SHS<sub>0.23</sub>, (c) SHS<sub>0.18</sub>, and (d) SHS<sub>0.14</sub>. .... 56

Figure 33: Top down SEM images at a magnification of 1500 of (a) SHS<sub>0.35</sub>, (b) SHS<sub>0.23</sub>, (c) SHS<sub>0.18</sub>, and (d) SHS<sub>0.14</sub>. .... 57

Figure 34: (a) The averaged images over the smooth surface in the near wall region with colour inversion. (b) The average of the images of the smooth surface in the near wall region with the roughness structure detection applied. The SRS, ARS, and LRS is denoted by the dash-dot (blue) line, dotted (black) line, and dashed (red) line, respectively. The surface reconstruction is shown as the solid (white) line. .... 59

Figure 35: (a) The averaged images over the NW coated surface in the near wall region with colour inversion. (b) The average of the images of the NW coated surface in the near wall region with the roughness structure detection applied. The SRS, ARS, and LRS is denoted by the dash-dot (blue) line, dotted (black) line, and dashed (red) line. The surface reconstruction is shown as the solid (white) line. .... 59

Figure 36: (a) Cropped image of the average the of images over SHS<sub>0.23</sub>. (b) Intensity profile of the average of the images over SHS<sub>0.23</sub>. .... 60

Figure 37: Mean streamwise velocity profiles at  $Re_b = 250$  over a smooth surface for repeatability verification..... 69

Figure 38: (a) Mean velocity profiles over a smooth surface for half channel at  $Re_b = 40, 140, 240, 330,$  and  $400.$  (b) Mean velocity profiles over a smooth surface in the near wall region ( $y < 0.2$  mm) at  $Re_b = 40, 140, 240, 330,$  and  $400.$ ..... 71

Figure 39: (a) Velocity profiles over the SHS at  $Re_b = 50, 150, 250, 350,$  and  $450.$  (b) Near wall region with the SRS (dash dot red line), ARS (dotted black line), and LRS (dashed blue line). . 72

Figure 40: Slip velocity versus  $Re_b$  at the three wall locations (SRS, ARS, and LRS) over the SHS. A linear fit over the first three data points show the performance of the SHS with an intact air layer..... 73

Figure 41: The trend between  $DR$  and  $Re_b$  over a SHS at the three wall locations (SRS, ARS, and LRS)..... 74

Figure 42: (a) Instantaneous velocity of tracer particles over a smooth surface and the sliding average with a bin size of  $y^+ = 0.25.$  (b) Linear fit over the sliding average in the near wall region ( $y^+ < 5$ ) for the smooth surface. .... 76

Figure 43: A comparison between the experimental data over a smooth surface ( $Re_\tau = 241$ ) to the turbulent channel flow equations with DNS by Kasagi et al. (1990) at  $Re_\tau = 211$  added for reference. .... 77

Figure 44: Instantaneous velocity of individual tracers over (a) SHS<sub>0.35</sub>, (c) SHS<sub>0.23</sub>, (e) SHS<sub>0.18</sub>, and (g) SHS<sub>0.14</sub> with a sliding average using a bin size of  $y^+ = 0.25.$  Figures (b), (d), (f), (h) show the mean velocity profile with a linear fit over the sliding average in the near wall region ( $y^+ < 5$ )

for surfaces SHS <sub>0.35</sub> , SHS <sub>0.23</sub> , SHS <sub>0.18</sub> , and SHS <sub>0.14</sub> , respectively, with the mean velocity profile of the smooth surface added for comparison. ....	78
Figure 45: Semi-log plot of the averaged velocity profile of the SHSs (a) without subtraction of $u_s^+$ (b) with subtraction of $u_s^+$ .....	79
Figure 46: The nondimensional slip velocity over the SHSs as a function of the nondimensionalized root mean squared roughness.....	80
Figure 47: Drag reduction percentage as a function of the nondimensionalized root mean squared roughness. ....	81
Figure 48: A SEM image of microposts with a gas fraction of 90%. ....	111
Figure 49: A SEM image of etched microposts with a gas fraction of 90%. ....	112
Figure 50: Turbulent statistics over SHS <sub>0.35</sub> , SHS <sub>0.23</sub> , SHS <sub>0.18</sub> , and SHS <sub>0.14</sub> . ....	113
Figure 51: Convergence plot of the turbulent statistics at $y^+ = \lambda$ over SHS <sub>0.35</sub> . ....	113

# List of Tables

Table 1: Summary of the experimental setup for the laminar and turbulent tests .....	53
Table 2: A summary of the laminar experimental setup and Shadow-PTV measurement parameters used for uncertainty analysis.....	62
Table 3: Calibration uncertainty sources and magnitudes for the PTV system.....	64
Table 4: Particle displacement uncertainty sources and magnitudes for the PTV system.....	65
Table 5: Time interval and tracking uncertainty sources and magnitudes for the PTV system. ..	66
Table 6: Total velocity uncertainty and the major error sources for the Shadow-PTV setup. ....	66
Table 7: Position and time uncertainty sources and magnitudes for the PTV system.....	67
Table 8: Total experimental uncertainty of the Shadow-PTV measurement system.....	68
Table 9: PTV measurement results over the SHS at $Re_b = 50, 150, 250, 350,$ and $450$ . ....	73
Table 10: Summarized results of the four SHSs in turbulent flow. ....	81

# 1 Introduction

## 1.1 Background

Flow of a fluid over a surface or body will produce pressure drag, and skin friction drag, which oppose the motion of the flow (Cengel & Cimbala 2014). This is true for flow over a fluid-fluid interface as well as a fluid-solid interface. This drag force has impacts on ground, air, and marine vehicles, and the transportation of liquids including water and oil. In vehicles, most of the energy produced for propulsion is used to overcome the drag force that is continuously slowing the vehicle (ABS 2014). In the transportation of liquids, most of the pumping energy required is spent overcoming the drag force. The study of drag reduction between a liquid and solid is important to countless businesses and nations because 90% of the world trade is done through transportation with the international shipping industry (International Chamber of Shipping 2017) and transportation of water by means of industrial and residential piping networks is common worldwide. Reducing the drag has impacts on a global level as drag reduction leads to a decrease in emissions, resources used, erosion rates, and operational costs.

Aside from aerodynamically and hydrodynamically streamlining the bodies to minimize the pressure drag, skin friction reduction methods have been introduced by changing the fluid properties as well as methods to alter the interaction between the liquid-solid surface. Methods that change the fluid properties are not ideal in most cases because it is impractical to alter the properties of the liquid in the case of marine vehicles and additives typically have environmental and health risks (Hellsten 2002) when used in large quantities which present too many risks to use in transportation of water. A promising field of study is drag reduction through means of surface modification. It is well known that smoother surfaces have less drag than relatively rough surfaces but studies have shown that through specific surface modifications the drag producing mechanisms in the flow can be directly reduced (Walsh & Lindemann 1984). Drag reduction through the use of superhydrophobic surfaces (SHSs) are an area of interest for this reason. Current manufacturing methods allow precise fabrication of surface structures, on the order of  $\mu\text{m}$ 's, with a high degree of repeatability, giving SHSs the potential to be mass produced with consistent properties and performance. Different methods of manufacturing surfaces have been studied but mostly focus on surfaces at a small scale as production of large scale surfaces is not done currently. Additionally,

due to the customizability of the surface pattern, the relationship between surface pattern, surface characteristics, fluid flow parameters, and the drag reducing performance are not fully understood.

## 1.2 Project objectives

Since SHSs are generally fabricated on a small scale ( $< 10$  cm), the first objective of the study was to design a laminar flow loop for testing SHSs as a preliminary measure. This would allow for an increased testing rate of SHSs to filter out designs with a lower drag reduction before fabrication on a larger scale for testing in the preexisting turbulent channel loop, which simulates more practical flow conditions.

The second goal of this study was to characterize and study the performance of a SHS produced by coating an aluminum surface with a commercially available hydrophobic spray. Specifically, the trend between the flow conditions and the drag reducing performance of the surface. This was achieved by varying the channel pressure and therefore the bulk flow rate while simultaneously characterizing the flow through particle imaging velocimetry to obtain the slip velocity, and slip length.

The third goal of the study was to determine the drag reducing abilities of SHSs with varying roughness under common flow conditions in the turbulent regime. Four SHSs were fabricated with the same method to produce identical surfaces save the surface roughness. The velocity profile over the SHSs was measured through particle tracking velocimetry and the drag reduction was determined.

## 1.3 Outline

To achieve the project objectives, the study was broken down into two sections. The first section involves measuring the performance of a SHS under the laminar flow regime, and the second section investigated, in the turbulent flow regime, a SHS design that has the surface roughness changing while the other surface parameters were constant.

This thesis is divided into the following chapters:



Chapter 2 – Literature review: A review of channel flow in the laminar and turbulent flow regimes, and their governing equations followed by a detailed explanation of both drag reduction via SHSs and the measurement methods used in this study.

Chapter 3 – Experimental setups: A breakdown of the testing facilities design, characterization of the surfaces, measurement equipment used, and measurement techniques.

Chapter 4 –Measurement uncertainty: A detailed breakdown of the uncertainty sources and their effect on the total uncertainty in the measured velocity in the laminar and turbulent channel.

Chapter 5 – Laminar channel flow over a randomly textured superhydrophobic surface: A discussion of the results from experiments with a SHS in the laminar flow regime. The slip length, slip velocity, and drag reduction of the SHS is compared to the bulk Reynolds number.

Chapter 6 –Turbulent channel flow over randomly patterned superhydrophobic surfaces with varying roughness: A discussion about the influence of the surface roughness on the slip velocity and drag reduction of a SHSs.

## 2 Literature review

### 2.1 Channel flow and terminology

Flows are categorized into two groups, external and internal. Bodies immersed in a fluid that is unbounded are classified as external flows while internal flows are classified as flows that have solid surfaces completely bounding them. Transportation of a fluid in pipes, ducts, and channels are all examples of internal flows. Both internal and external flows can operate in three regimes, laminar, transition, and turbulent. With the use of Reynolds number,  $Re$ , a critical nondimensional value determines the flow regime (Cengel & Cimbala 2014).

This study focuses on internal flows, more specifically channel flows. Channel flows, shown in Figure 1, are flows bounded by four walls with channels typically having a rectangular cross-section and dimensioned based on the length ( $L$ ), width ( $w$ ), height ( $h$ ), and aspect ratio ( $w/h$ ). Channel flow is a common area of study due to the simplistic geometry allowing for easier experimental and numerical investigations of the complex turbulent nature and near-wall interactions. When studying channel flow, the position vector is denoted in standard Cartesian coordinates as  $x_i = (x, y, z) = (x_1, x_2, x_3)$  where the positive  $x$ ,  $y$ , and  $z$  coordinates are the positive streamwise, wall-normal and spanwise directions respectively. The instantaneous velocity vector is denoted as  $U_i = (U, V, W) = (U_1, U_2, U_3)$  with  $U$ ,  $V$ ,  $W$  representing velocity in the  $x$ ,  $y$ ,  $z$  directions respectively. For channel flow the  $Re$  can be expressed as

$$Re = \frac{\rho U_{avg} D_h}{\mu}, \quad 2.1$$

where  $\rho$  is the fluid density,  $U_{avg}$  is the mean flow velocity, and  $\mu$  is the dynamic viscosity of the fluid.  $D_h$  is the hydraulic diameter of the channel which can be expressed as  $D_h = 2wh/(w+h)$ . Similarly, the bulk Reynolds number,  $Re_b$ , is defined based on the full channel height,  $h$ , instead of  $D_h$ . At each wall location ( $y = 0$ ,  $y = h$ ,  $z = 0$ ,  $z = w$ ) exists a no-slip boundary condition where  $U = V = W = 0$ . For channels with  $w/h < 10$ , the flow is fully developed in the streamwise direction ( $\partial U/\partial x = 0$ ) after a minimum distance of  $90h - 150h$  (Coulson et al. 1995; Lien et al. 2004). If the channel has a  $w/h \gg 1$ , at the  $w/2$  location, the flow is free of boundary effects caused by the side

walls. With these constraints, a minimum downstream distance and center width location is ideal for taking measurements of the flow.

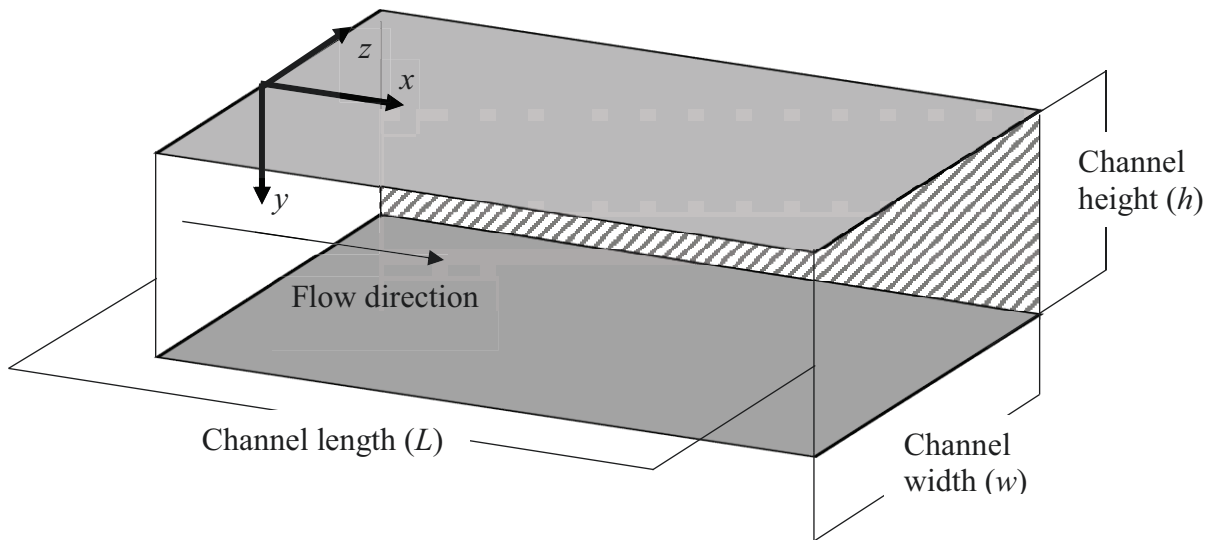


Figure 1: An illustrated example of channel flow with dimensions.

## 2.2 Laminar flows

For internal flows the laminar regime exists at  $Re < 1500$  (Pritchard & Leylegian 2011). Laminar flows are considered calm and smooth in motion with the fluid flowing in layers having no macroscopic mixing between adjacent layers (Pritchard & Leylegian 2011). Laminar flow through a channel, shown in Figure 2, has a maximum velocity,  $U_\infty$  and upon entering the channel forms a boundary layers on each of the walls. These boundary layers grow in the wall-normal direction until they converge, after which the flow is said to be fully developed.

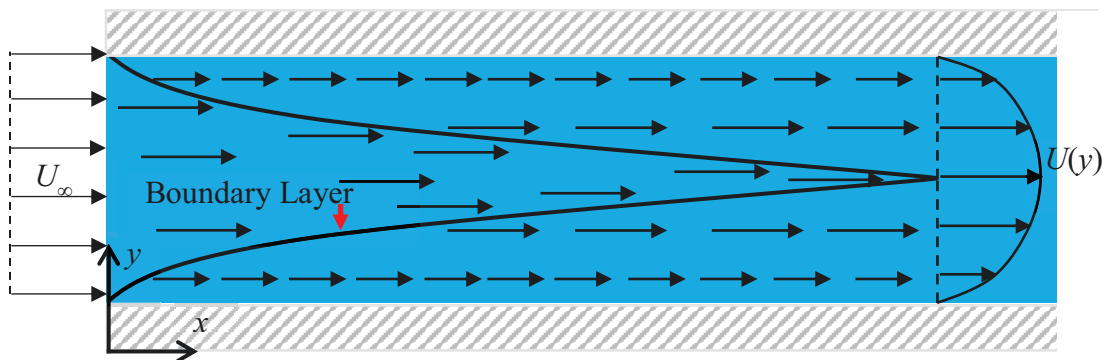


Figure 2: An illustrated image of laminar flow in a channel depicting the boundary layer growth.

### 2.2.1 Governing equations

Laminar flows can be fully modelled with conservation of mass equations, and conservation of momentum equations, also known as the Navier-Stokes equations (NSE). Equations 2.2 and 2.3 respectively show the conservation of mass and the three dimensional (3-D) NSE in index notation.

$$\frac{\partial U_i}{\partial x_i} = 0 \quad 2.2$$

$$\left( \frac{\partial}{\partial t} + U_j \frac{\partial}{\partial x_j} - \nu \frac{\partial^2}{\partial x_j \partial x_j} \right) U_i = -\frac{1}{\rho} \frac{\partial P_i}{\partial x_i} + F_i \quad 2.3$$

$P$ ,  $F$ , and,  $\nu$  are the net pressure forces, net external forces, and fluid kinematic viscosity respectively with  $\partial U/\partial t + U_j \partial U_i/\partial x_j$  representing the effect of inertial forces on the fluid, and  $\nu \partial^2 U_i/\partial x_j \partial x_j$  representing the effect of viscous forces on the fluid.  $\partial P/\partial x_i$  represents the effect of net pressure forces on the fluid, and  $F_i$  represents the effect of the net external forces applied to the fluid.

Modelling of the flows is used for direct numerical simulations (DNS) and also provides a standard for measurements of the velocity profile to be compared with. From the governing laws, the velocity profile in laminar channel flow can be derived through a simplification of 2.3 using 2.2, a flow that is fully developed, steady state, two dimensional, and bounded by two parallel plates, that is,

$$\frac{\partial U}{\partial x}, \frac{\partial}{\partial t}, W, U|_{y=0}, \text{ and } V|_{y=0} = 0. \quad 2.4$$

The conservation of mass equation can be reduced to

$$\frac{\partial V}{\partial y} = 0 \quad 2.5$$

while the  $x$ -component of the 3-D NSE simplifies to

$$0 = G + \mu \left( \frac{\partial^2 U}{\partial y^2} \right), \quad 2.6$$

where  $G = -\partial P/\partial x$ .

From 2.4 the  $z$ -direction of the NSE is eliminated, from 2.4 and 2.5,  $V = 0$ , therefore the  $y$ -component of the NSE is eliminated as well. Integrating 2.6 across the full channel height results in

$$-\frac{Gy}{\mu} + C_1 = \frac{\partial U}{\partial y}. \quad 2.7$$

and finally

$$U(y) = \frac{Gy}{2\mu} (2\delta - y). \quad 2.8$$

Equation 2.8 allows the modelling of a velocity profile with known pressure gradient or for determination of the pressure gradient in visualized flows.

There exists a slip-condition where the tangential velocities of the flow are not equal to that of the wall whereby the velocity at the wall, denoted as slip velocity,  $u_s$ , is described with Navier's model

$$u_s = l_s \left. \frac{\partial U}{\partial y} \right|_{wall}. \quad 2.9$$

Where the slip length,  $l_s$ , is defined as the imaginary distance into the solid surface required before the velocity profile reaches zero after extrapolating the profile in the near boundary region. The slip mechanism will be discussed in further detail in Chapter 2.4.2. The velocity profile for laminar channel flow with the top wall exhibiting a slip condition is derived in a similar fashion to the no-slip scenario. Equation 2.6 integrates to give

$$U(y) = \frac{y^2 G}{2\mu} + C_1 y + C_2 \quad 2.10$$

with boundary conditions of

$$U(0) = 0 \text{ and } U(-l_s) = 0, \quad 2.11$$

resulting in a velocity profile expressed as

$$U(y) = \frac{G}{2\mu} \left[ (y^2 - \delta^2) - \frac{(y - \delta)(\delta^2 - l_s^2)}{\delta + l_s} \right]. \quad 2.12$$

## 2.3 Turbulent flows

The second part of this study focuses on turbulent flow of an incompressible fluid between two parallel plates shown in Figure 3. Turbulent channel flows by nature have fluctuations that are random, unpredictable, and typically occur when  $Re > 3000$  (Pritchard & Leylegian 2011). The growth of the turbulent boundary layer in the wall normal direction is hindered due to the confinement of the fluid by the two parallel walls. Due to the wall confinement and length of the channel, after the boundary layers converge the turbulent flow will be statistically independent from the spanwise direction. When studying drag reduction over a surface in turbulent channel flows there are three main regions of interest; the linear viscous sublayer where viscous effects dominate, the buffer layer which is a transitional layer, and the overlap region where momentum effects dominate.

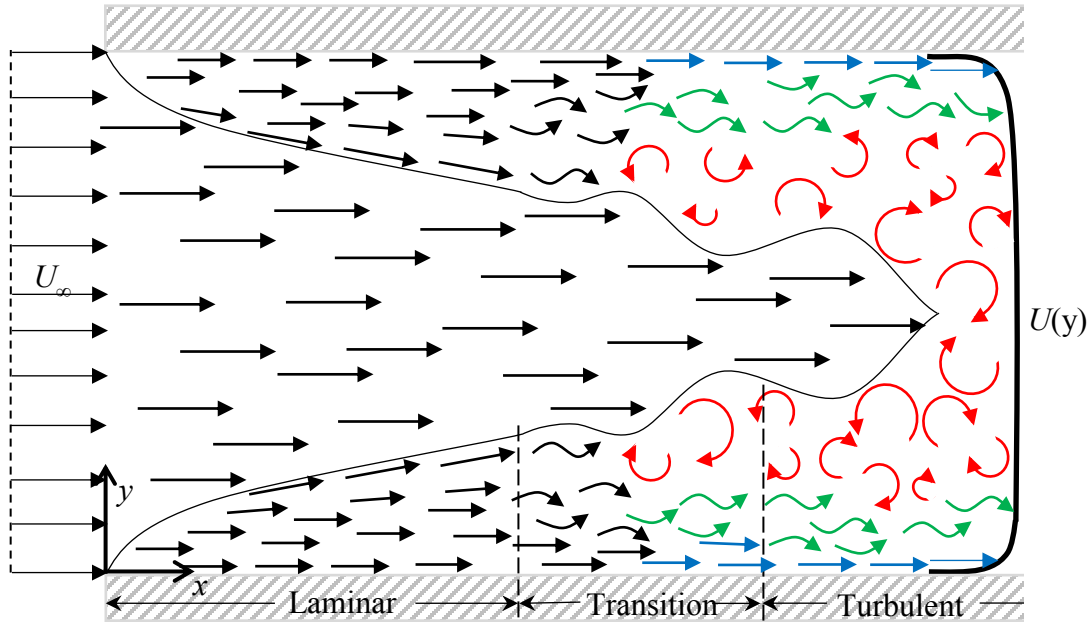


Figure 3: An illustrated image of turbulent channel flow depicting the boundary layer growth and the three regimes of boundary layer.

In the study of turbulent flows, a Reynolds decomposition method is used which is defined as

$$U_i = \bar{U}_i + u_i, \quad 2.13$$

where  $u_i = (u, v, w) = (u_1, u_2, u_3)$  are the fluctuation of the velocity vector in the  $x, y, z$  direction and values denoted by overbar are the time average of the quantities. Two fluctuating terms multiplied together are referred to as Reynolds stresses. For 2D flow, the Reynolds stresses are  $u^2$ ,

$v^2$  and  $uv$ . Turbulent kinetic energy,  $k$ , is defined as  $k = 0.5(\langle u^2 \rangle + \langle v^2 \rangle + \langle w^2 \rangle)$  where  $\langle \rangle$  denotes averaging in space and time. Figure 4 below shows a DNS study highlighting the relationship each component of the 2D Reynolds stress plays on  $k$  as a function of nondimensionalized distance from the wall,  $y^+$ .

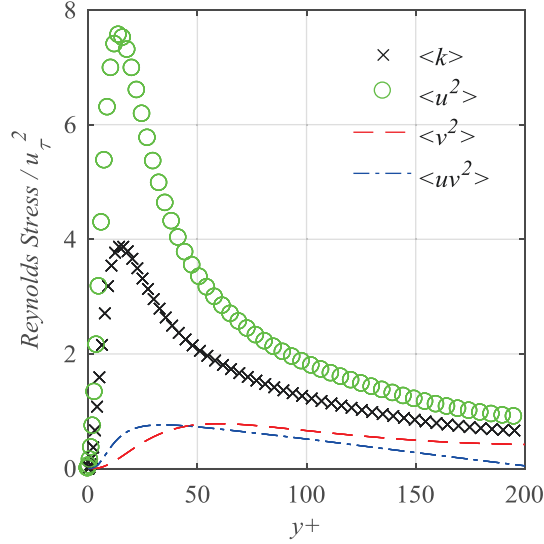


Figure 4: The relationship between turbulent kinetic energy and Reynolds stresses normalized by friction velocity against  $y^+$  from DNS turbulent channel flow at  $Re=6666$  (Kasagi et al. 1993).

### 2.3.1 Governing equations

Most of the discussion of this section evolves from Pope (2000) and Kundu et al. (2012). The governing equations of turbulent flow are the same as for laminar flow, conservation of mass and conservation of momentum. However, they must undergo the Reynolds decomposition followed by taking the mean. Applying this to the mass conservation equation (2.2) yields

$$\frac{\partial \bar{U}}{\partial x} + \frac{\partial \bar{V}}{\partial y} = 0, \quad 2.14$$

and knowing that  $U$  and therefore  $\bar{U}$ , is independent of  $x$ , the mass conservation equation can be reduced to

$$\frac{\partial \bar{V}}{\partial y} = 0. \quad 2.15$$

After integration and application of the boundary condition  $V|_{y=0} = 0$  it can be determined that  $\overline{V} = 0$ .

Applying the Reynolds decomposition to the momentum equation (2.3) it results in

$$\frac{\partial \overline{U}_i}{\partial t} + \overline{U}_j \frac{\partial \overline{U}_i}{\partial x_j} = -\frac{1}{\rho} \frac{\partial \overline{P}}{\partial x_i} - \frac{\partial \overline{u_i u_j}}{\partial x_j} + \nu \frac{\partial^2 \overline{U}_i}{\partial x_i \partial x_j}. \quad 2.16$$

Applying the assumptions that the flow is 2D and fully developed

$$\frac{\partial}{\partial t} = 0, \frac{\partial}{\partial z} = 0, \overline{W} = 0, \quad 2.17$$

the  $y$  component of the decomposed momentum equation, 2.16, can be then reduced to

$$\frac{1}{\rho} \frac{\partial \overline{p}}{\partial y} - \frac{d}{dy} \overline{v^2} = 0. \quad 2.18$$

With the boundary condition of  $\overline{v^2}|_{y=0} = 0$ , applying an integration about the wall-normal direction results in,

$$\overline{v^2} + \frac{\overline{P}}{\rho} = \frac{P_w(x)}{\rho} \quad 2.19$$

where  $P_w$  is the mean pressure at the wall and

$$\frac{\partial \overline{P}}{\partial x} = \frac{dP_w}{dx}. \quad 2.20$$

In a similar fashion, the  $x$  component of the momentum equation reduces to

$$\frac{1}{\rho} \frac{\partial \overline{p}}{\partial x} + \frac{d\overline{uv}}{dy} - \nu \frac{d^2 \overline{U}}{dy^2} = 0. \quad 2.21$$

By defining total shear stress as the sum of Reynolds shear stress and the viscous stress

$$\tau = -\rho \overline{uv} + \mu \frac{d\overline{U}}{dy}, \quad 2.22$$

2.21 can be rewritten as,

$$\frac{d\tau}{dy} = \frac{dP_w}{dx}. \quad 2.23$$



In the viscous sublayer the term  $\mu d\bar{U}/dy$  dominates and the shear stress at the wall,  $\tau_w$ , is defined as

$$\tau_w = \mu \left. \frac{\partial \bar{U}}{\partial y} \right|_{y=0}. \quad 2.24$$

Two scales are used to define the velocity and length in the viscous sublayer, friction velocity,  $u_\tau$ , and the wall unit,  $\lambda$ . Friction velocity is the velocity associated with the viscous forces and is defined as

$$u_\tau = \sqrt{\frac{\tau_w}{\rho}} \quad 2.25$$

whereas the wall unit is defined as

$$\delta_v \equiv \nu \sqrt{\frac{\rho}{\tau_w}} = \frac{\nu}{u_\tau}. \quad 2.26$$

In the study of turbulent flow, values nondimensionalized by  $u_\tau$  and/or  $\lambda$  are expressed with superscript +.

In the viscous sublayer the mean velocity profile is a function of the fluid properties, the distance from the wall in the wall normal direction, and the wall shear stress,

$$\bar{U} = f(\mu, \rho, y, \tau_w). \quad 2.27$$

Two nondimensionalized parameters are used to describe the relationship between the variables,

$$u^+ = \frac{\bar{U}}{u_\tau}, y^+ = \frac{y}{\delta_v}. \quad 2.28$$

Equation 2.27 can be rewritten as

$$\frac{\bar{U}}{u_\tau} = f\left(\frac{y}{\delta_v}\right), \quad 2.29$$

and through a Taylor-series expansion a 1:1 linear relationship exists between the left hand side and right hand side of 2.29, thus it can be stated that

$$\frac{\bar{U}}{u_\tau} = \frac{y}{\delta_v} \text{ or } u^+ = y^+. \quad 2.30$$

This region of the boundary layer is the linear viscous sublayer which obeys 2.30, also referred to as the law of the wall. The linearity continues up to a distance  $y^+ = 5$  after which the contribution drops down to 50% at  $y^+ = 12$  and by  $y^+ = 50$  contributes to less than 10% of the total stress (Pope 2000). The region in which neither effect dominates the other is known as the buffer layer and continues up to a distance  $y^+ = 40$  from the wall. In this region, the majority of the production and dissipation of turbulent kinetic energy occur. After the buffer layer viscous forces are negligible thus the velocity is no longer a function of  $\mu$  but instead dominated by the large eddies which are on the scale of boundary layer thickness  $\delta_b$ . The equation for the velocity profile is given as

$$\frac{U_{avg} - \bar{U}}{u_\tau} = g\left(\frac{y}{\delta_b}\right). \quad 2.31$$

where  $g$  is a function dependent of Reynolds number. In this region, once the distance from the wall satisfies the condition  $\lambda \ll y \ll \delta_b$ , the length scale  $\delta_b$  is no longer important and the dependence on  $\lambda$  vanishes. This sub region is known as the overlap region with a defining equation as follows,

$$\frac{du^+}{dy^+} = \frac{1}{\kappa y^+}. \quad 2.32$$

Integration of 2.32 leads to the equation known as the logarithmic law of the wall (log law) equation

$$u^+ = \frac{1}{\kappa} \ln y^+ + B, \quad 2.33$$

where  $\kappa$  is the von Karman constant and  $B$  is a constant. From experimental data the values for  $\kappa$  and  $B$  have are determined to be 0.41 and 5.2 respectively over smooth surfaces. Figure 5 below shows the relationship between  $u^+$  and  $y^+$  in three regimes.

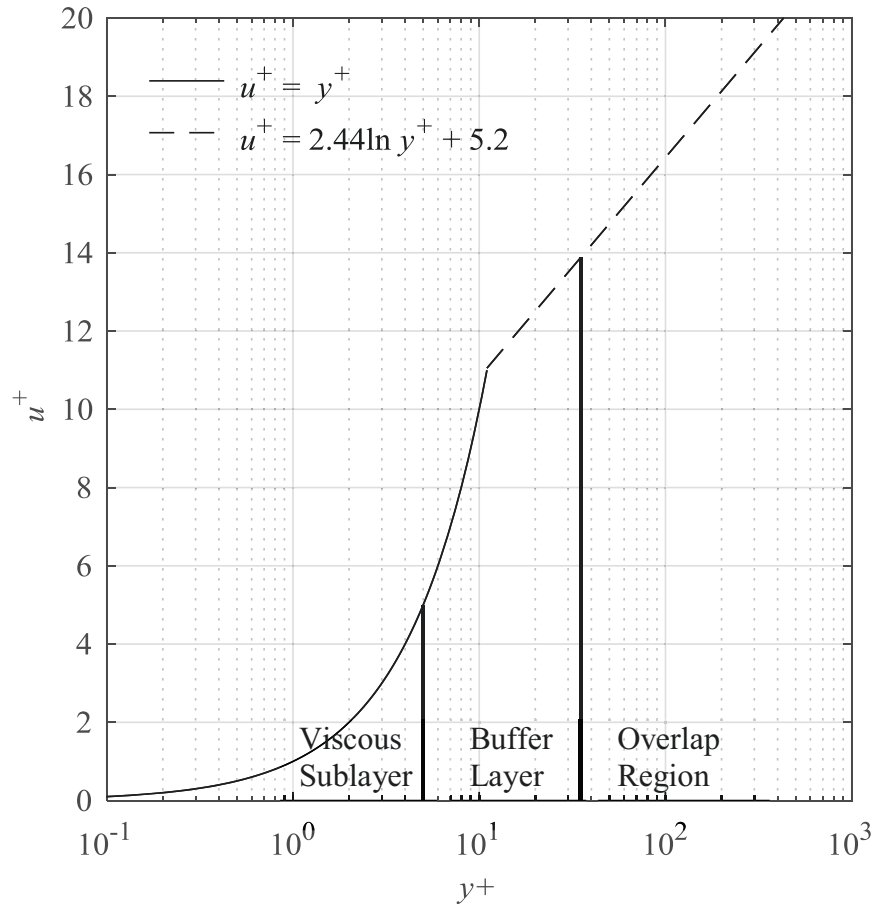


Figure 5: A graphical comparison showing the relationship of  $u^+$  to  $y^+$  for turbulent flow.

## 2.4 Drag reduction with superhydrophobic surfaces

Drag is a function of the fluid properties and the surface properties of the solid. By increasing the surface roughness, the effective contact area between the liquid and solid surface increases thereby increasing the drag (Flack & Shade 2004). This is why smoother and more polished materials have a lower friction coefficient than surfaces with high roughness. Therefore, a solution to reducing drag is through decreasing the contact area between the liquid-solid interface. This study focuses only on drag reduction via SHSs. The fundamentals of drag reduction via SHSs and the slip phenomena is reviewed before a discussion and a brief background of what constitutes as a SHS. The section ends with a derivation of equations for drag and drag reduction in laminar and turbulent channel flows.

### 2.4.1 Contact angle and contact angle hysteresis

Classification of SHSs is typically based on their surface pattern and contact angle with water,  $\theta$ . The surface pattern and surface chemistry (heterogeneity) both influence  $\theta$  (Chau et al. 2009). During wetting, the liquid contacts the surface at a contact angle determined by the shape that minimizes the droplet surface area through balancing the interfacial forces between the liquid-air and liquid-solid surfaces (Cassie & Baxter 1944). The  $\theta$  provides a measure of the favourability for a surface to be wetted (Shafrin & Zisman 1960). A highly favourable surface will have a  $\theta < 90^\circ$  and a  $\theta > 90^\circ$  shows the surface has a low favourability to wetting. Figure 6 shows two surfaces with a 30  $\mu\text{L}$  water droplet illustrating the hydrophobic effect where one surface is wetted,  $\theta = 86^\circ$ , and the second is not,  $\theta = 153^\circ$ . For visual clarity, only one surface is annotated to show the contact angle. Typically,  $\theta$  is determined with equipment that can obtain or estimate the curvature of the droplet and find the angle with respect to a baseline. The contour of a droplet with a  $\theta < 10^\circ$  fits the shape of a circle or arc while at  $\theta > 20^\circ$  the contour has a more elliptical shape. As the contact angle increases towards  $180^\circ$  the shape returns to a better fit with a circle ( $\theta > 170^\circ$ ) than an ellipse (Thomsen 2008). A droplet volume between 1  $\mu\text{L}$  and 10  $\mu\text{L}$  is said to have negligible effect on the contact angle while at higher volumes the apparent contact angle is reduced (Krüss 2004).

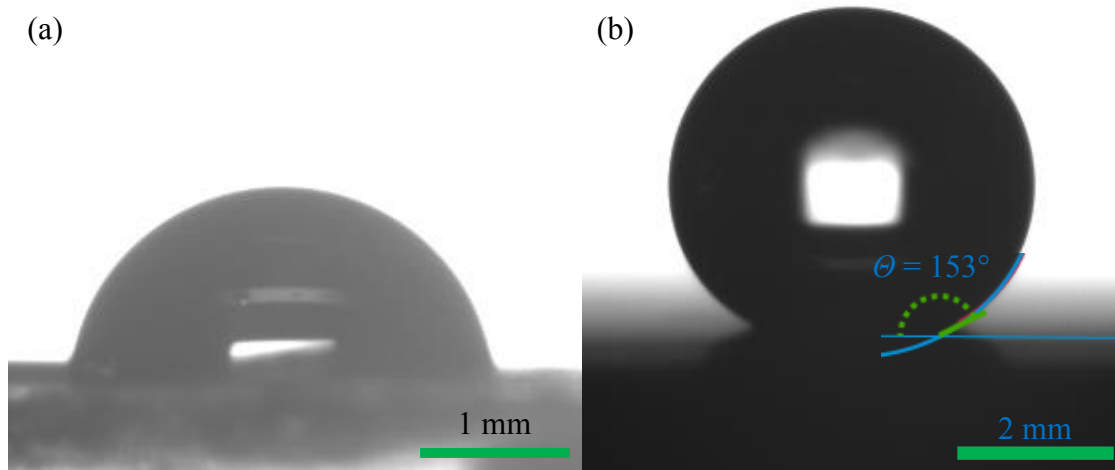


Figure 6: An image of a 30  $\mu\text{L}$  water droplet on (a) a smooth polystyrene surface with a contact angle of  $86^\circ$  and (b) a SHS showing a contact angle of  $153^\circ$ .

In 1805, Young described wetting of a liquid on a solid surface and the equation which relates the interfacial surface energy (the associated energy of the intermolecular forces at the interface) per

unit area of the liquid, solid, and gas interfaces with the angle between the droplet and the surface. For an ideal smooth surface, Young's equation can be expressed as

$$\gamma_{LV}\cos\theta = \gamma_{SV} - \gamma_{LS}, \quad 2.34$$

where  $\gamma_{LV}$ ,  $\gamma_{SV}$ , and  $\gamma_{LS}$  are the surface energies between the liquid-vapour interface, solid-vapour interface, and liquid-solid interface, respectively (Young 1805). When taking into consideration surface roughness there are two wetting regimes; homogenous and heterogeneous. Wenzel said that the surface roughness factor,  $r$ , plays a role in the resulting contact angle because water fills the voids between the roughness resulting in homogeneous wetting. The roughness factor is the ratio of the actual surface area wetted to the geometric surface area such that  $r > 1$  (Wenzel 1936). The Wenzel equation of wetting is

$$\cos\theta^* = \frac{r(\gamma_{SV} - \gamma_{LS})}{\gamma_{LV}}, \quad 2.35$$

where  $\theta^*$  is the apparent contact angle and  $\cos(\theta^*) = r\cos(\theta)$ . The heterogeneous wetting case, modelled by the Cassie-Baxter equation (Cassie & Baxter 1944), occurs when the droplet does not wet between the roughness and gas remains in the voids between the roughness structures under the droplet. In this case, the apparent contact angle depends on the ratio of the wetted area to the actual surface area,  $\phi_s$ .

$$\cos\theta^* = \phi_s(\cos\theta + 1) - 1. \quad 2.36$$

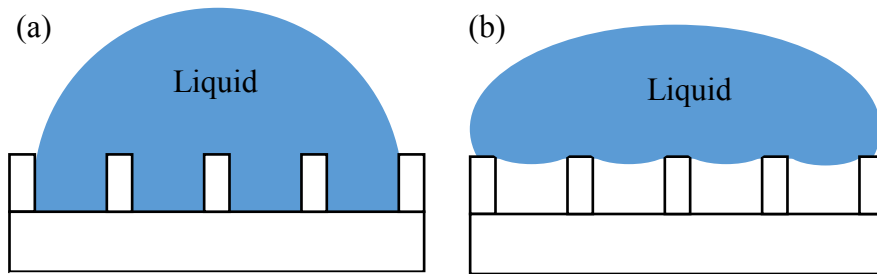


Figure 7: An illustration showing a droplet in the (a) Wenzel state and (b) Cassie-Baxter state.

The second characteristic of a superhydrophobic surface is contact angle hysteresis. Contact angle hysteresis,  $\Delta\theta$ , is the difference between the advancing contact angle,  $\theta_{adv}$ , and receding contact angle,  $\theta_{rec}$ , (Joanny & De Gennes 1984) which can be seen in Figure 8. A lower  $\Delta\theta$  parameter will have a droplet rolling off of a surface as opposed to sliding off (Aussillous & Quéré 2004).

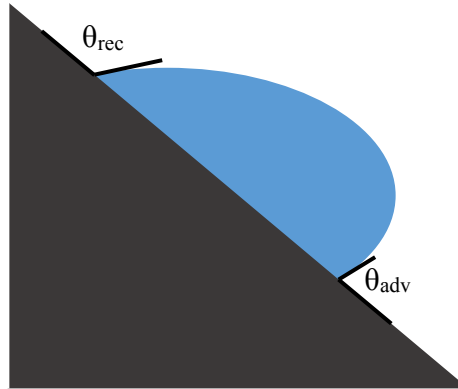


Figure 8: An illustration of measuring contact angle hysteresis using an inclined plane.

A droplet in the Wenzel state will have a larger  $\Delta\theta$  because the measurement is taken from the pinned point of the solid-liquid contact which is located between the roughness whereas in the Cassie state the solid-liquid contact is on the peaks of the roughness. From equation 2.36 above, decreasing the solid fraction increases the contact angle and decreases the hysteresis, however, there is a limit to the allowable space between the structures as the hydrodynamic equilibrium will not be maintained and the droplet will eventually collapse and fully wet the surface as shown by Park et al. (2009). The rolling of a droplet and the ability to maintain the Cassie-Baxter state are important to superhydrophobic surfaces but do not directly relate to the determination of drag reduction. From the studies discussed in Chapter 2.4.3, and through the work of Gose et al. (2018) it is known that higher contact angles and lower hysteresis parameters at ambient pressures do not translate into higher drag reduction. Instead the drag reduction in turbulent flows is a function of the contact angle hysteresis at higher pressures as well as the surface roughness (Gose et al. 2018).

### 2.4.2 Slip over a surface

There are two categories of slip, intrinsic and apparent. Intrinsic (or molecular) slip is the slippage of a liquid over a solid surface while in complete contact. In order for this to occur on a scale significant to the study of drag reduction on a macroscale, it would require large hydrodynamic forces in the form of a tremendous shear rate ( $10^{12} \text{ s}^{-1}$ ) (Lauga et al. 2005). Molecular dynamic simulations by Martini et al. (2008) and Sendner et al. (2009) showed that slip lengths are  $<10 \text{ nm}$  while studies by Cottin-Bizonne et al. (2003), and Cottin-Bizonne et al. (2004) showed slip lengths of  $100\text{-}200 \text{ nm}$  are achievable depending on the surface roughness. Again, these studies have an

application in the field of microfluidics but not for drag reduction on a larger scale (Tuteja et al. 2007).

Apparent slip occurs when the flow follows the no-slip condition on a smaller length scale while when viewed on a larger length scale the no-slip condition does not appear to be held. An example of this is sand translating inside a pipeline at the wall. Although the velocity at the contact between the sand and the pipe is zero, the sand will roll along the surface showing an apparent velocity at the wall. The “gas cushion model” first proposed by Vinogradova in 1995 described the solid-liquid slip over a hydrophobic surface due to a lubricating gas film. The slip length is the distance from the wall where the tangential velocity would reach zero based on the extrapolated velocity profile. The equation to determine the slip length is given by

$$l_s = e \left( \frac{\eta}{\eta_g} - 1 \right) \quad 2.37$$

where  $\eta_g$  is gas viscosity,  $\eta$  is the bulk liquid viscosity, and  $e$  is the air layer thickness. If the apparent or molecular slip is estimated through the averaging of the flow over the length scale of the experimental setup the resulting slip length is referred to as the effective slip.

### 2.4.3 Superhydrophobic surfaces

Superhydrophobic surfaces, by definition, are surfaces that have a  $\theta > 150^\circ$  and a roll-off/contact angle hysteresis less than  $10^\circ$  (Wang & Jiang 2007). SHSs achieve this through two mechanisms; the first is by having a low attraction to polar molecules and the second is by having a surface roughness that minimizes the contact area between the surface and the water droplet. With a combination of these two mechanisms, when water comes into contact with a SHS, the polar water molecules are more attracted to one another than to the surface resulting in a formation of spherical beads that minimize the surface area to volume ratio. The low attraction between the polar molecules and the surface combined with the minimal contact area allow the beads roll off leaving the surface unwetted. SHSs reduce skin friction by decreasing the contact area between the liquid and solid interface. Figure 9 shows that the trapped air between the surface roughness coupled with the low surface energy of the solid prevents water from entering the cavities and in turn reduces the total contact area. Direct numerical simulations by Rastegari & Akhavan (2015) showed that there are two contributions from SHSs that reduce drag in the turbulent regime. The

first is the change in the velocity profile of the bulk flow due to the slip velocity over the surface which makes up at least 80% of the drag reduction. The second is due to the change in the turbulent dynamics and structures produced in the flow which only attributes to 20% of the drag reduction.

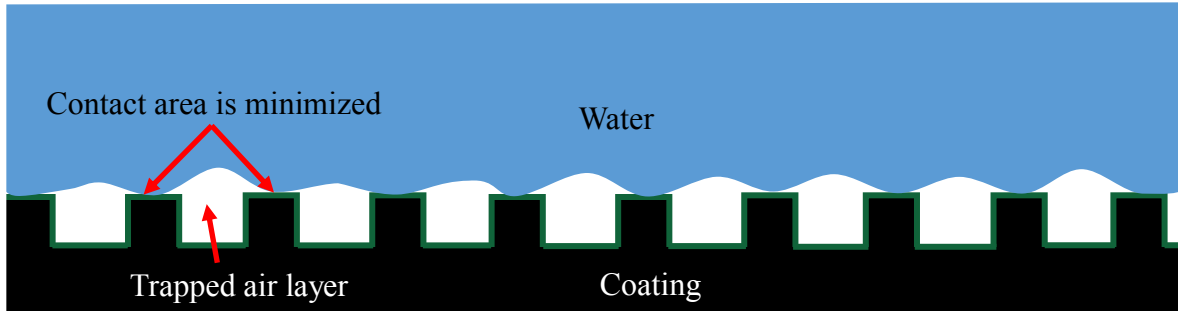


Figure 9: An illustration showing the effect a patterned surface with low surface energy has on the liquid-solid boundary.

Within the last 15 years artificial SHS technology has emerged, however, they were inspired by natural surfaces. The lotus leaf is a classic SHS in nature where the surface roughness and coating have been heavily studied and reproduced (Barthlott & Neinhuis 1997; Koch et al. 2006; Bhushan et al. 2009). Hundreds of other plant leaves have been studied and their surface structures and coatings categorized (Neinhuis & Bartlott 1997; Barthlott et al. 1998; Koch et al. 2008). Insect wings can have superhydrophobic properties and many studies have been done to replicate the structures and the coatings (Kreuz et al. 2001; Perez Goodwyn et al. 2009; Byun et al. 2009; Sun & Bhushan 2012; Nguyen et al. 2013). The use of SHSs for drag reduction is commonly studied experimentally by measuring the velocity field, the slip length, slip velocity, and ultimately, the drag reduction.

Bio-inspired surfaces have been tested by Kavalenka et al. (2015) who fabricated a nanofur design that had thin hair-like features 56  $\mu\text{m}$  in height and in clusters 53  $\mu\text{m}$  in diameter. The drag reduction abilities of the nanofur surface showed a pressure drop reduction of 50% compared to a smooth polycarbonate surface in the  $Re$  range of 20-120. The surface performance was compared with lotus leaves, which are known for their hydrophobic and air retaining properties. The nanofur surfaces achieved 50% air plastron stability under 0.5 bar above atmospheric while the lotus leaf only retained the air plastron below 0.135 bar above atmospheric.

The easiest method for creating a SHS is to use a low surface energy material. A study by Tretheway & Meinhart (2002) used particle image velocimetry (PIV) to study slip velocity in a 30  $\mu\text{m} \times 300 \mu\text{m}$  channel which was fully coated with octadecyltrichlorosilane (OTS) of a thickness



of 2.3 nm. The OTS surface produced a slip velocity which was 10% of the free stream velocity, corresponding to slip length of 1  $\mu\text{m}$ .

Kashaninejad et al. (2012) used microhole arrays fabricated from polydimethylsiloxane (PDMS) keeping a constant height of 10  $\mu\text{m}$  while varying the hole diameter, wall thickness, and row offset distance. The surface achieved a maximum contact angle of  $146^\circ$ . They operated the channel ( at a constant hydrostatic pressure and measured the increase in flowrate when compared to a smooth surface. The channel dimensions were  $41.25 \text{ mm} \times 220 \mu\text{m} \times 20 \mu\text{m}$  ( $L \times w \times h$ ). At hydrostatic pressures between 500 - 1500 Pa the average velocity through the channel was seen to increase by 40% corresponding to a slip length of 2.49  $\mu\text{m}$ . Song et al. (2014) studied the naturally hydrophobic Teflon strips by sanding them in the streamwise and transverse directions and also with circular patterns with varying grits of sand paper. The Teflon surfaces were tested in a PDMS microchannel using two pressure ports 45 mm apart to measure the pressure difference at  $Re < 100$ . The channel dimensions were  $60 \text{ mm} \times 3.4 \text{ mm} \times 137 \mu\text{m}$  ( $L \times w \times h$ ). The highest measured drag reduction was 27% with a slip length of 20  $\mu\text{m}$  achieved from sanding in the streamwise direction with 240 grit sandpaper.

Surfaces fabricated through photolithography allow for customizable repeating designs on the surface of the SHS. Ou et al. (2004) studied structured SHSs designed with repeating patterns of microposts and microridges. The contact angle with water on these surfaces were greater than  $160^\circ$ . A series of microchannels were used with varying heights between 76  $\mu\text{m}$  to 254  $\mu\text{m}$  while keeping the aspect ratio and length of the microchannel constant at 20 mm and 50 mm, respectively. All flows had a  $Re < 1000$  with a maximum pressure drop reduction of 40 % corresponding to a slip length of 21  $\mu\text{m}$  at a flow rate of 16.5  $\text{mm}^3/\text{s}$  and channel height of 127  $\mu\text{m}$ . Choi et al. (2006a) experimented with surfaces that had closely-spaced, repeating nanogrooves in laminar flows. The surfaces had a contact angle with water of  $145^\circ < \theta < 150^\circ$ . The SHS was tested with the grooves orientation parallel to the flow as well as transverse to the flow in microchannels with heights ranging from 2  $\mu\text{m}$  to 12  $\mu\text{m}$ . The surfaces showed slip lengths between 100-200 nm with no visible decrease in the slip length after a few hours. The corresponding pressure drop reductions were between 20% - 30% compared to a smooth surface. The results showed that the nanograting pattern gave a larger effective slip when oriented parallel to the flow as opposed to transverse in the flow.

Hierarchically designed SHSs fabricated via photolithography have also been studied by Jung & Bhushan (2010) who used hierarchical micro pillar structures 14  $\mu\text{m}$  in diameter and 30  $\mu\text{m}$  in height. The pillars were fabricated from an epoxy resin with the nanofeatures coated through thermal evaporation and deposition of lotus wax which naturally forms tubular structures 100-150  $\mu\text{m}$  in diameter and 1.5-2  $\mu\text{m}$  in length. The channel had the upper and lower surfaces composed of the SHS while the side wall material had a no-slip boundary condition. A syringe pump provided flowrates up to  $Re = 300$ . The drag reduction was measured through pressure differential using a differential manometer. The hierarchical structure provided more drag reduction than both the lotus wax and micro pillars without the lotus wax coating. The highest drag reduction measured was 30% when compared to flow over a smooth surface. The hierarchical structure also showed a higher slip length (103  $\mu\text{m}$ ) than the uncoated microposts (50  $\mu\text{m}$ ) and only the lotus wax (91  $\mu\text{m}$ ). Zhang et al. (2016) tested a square micropost design with and without silica nanoparticles added to the surface to increase the surface roughness. The surface solid fraction and height were held constant at 25% and 30 $\mu\text{m}$  respectively while the spacing and size of the posts was varied. The effect the surface roughness had on the surfaces' ability to keep the air plastron layer at a Reynolds number of 4700 was also studied showing the largest difference of a 38% increase in the air plastron area while the surface was under flow conditions. In the laminar flow regime, a maximum of 38.5% drag reduction was achieved with the silica nanoparticles compared to 31.1% when there were no silica particles present.

Other methods of fabricating SHSs are still of interest as there is no definitive method that works best on a large scale. Wang et al. (2015) studied one-step solution-immersion surfaces that produced nanoribbon features 1-2 $\mu\text{m}$  long and 70-130nm thick. This process had the ability to alter the size of the nanoribbons through solution developing time and showed the capability of recovering from abrasive damage when placed back in the solution. The surfaces were tested under external flow conditions with a range of  $Re$  from  $1.1 \times 10^6$  -  $2.2 \times 10^6$ . The maximum drag reduction achieved was 45% at the lowest  $Re$ . Gogte et al. (2005) studied SHSs created by a variation of the low temperature/pressure aerogel thin film process developed by Prakash et al. (1995). The surfaces had a contact angle with water of  $\theta = 156^\circ$ . At a Reynolds number of 1500, a slip velocity of 0.5 cm/s was measured with a free stream velocity of 3.7 cm/s, corresponding to a drag reduction of 15%.

Still, the optimal surface organization and size has not been determined. Much work needs to be done to advance the technology before it can be implemented on a large scale commercially. Developing a relationship between the surface characteristics and the performance plays a key role in the future of this technology. The other aspect of fabricating SHSs still faces challenges as surfaces have not been made for practical large scale applications as of yet.

#### 2.4.4 Estimation of drag

Work by Fukagata, Iwamoto, and Kasagi (FIK) (Fukagata et al. 2002) introduced a relationship between skin friction,  $C_f$ , and Reynolds stresses for wall-bounded turbulent flows. The following discussion is adapted from their work.

The Reynolds Average of the Navier Stokes equations in the streamwise direction is,

$$-\frac{\overline{\partial P}}{\partial x} = \frac{\partial}{\partial y} \left( -\frac{1}{Re_b} \frac{\partial \bar{U}}{\partial y} + \overline{uv} \right) + \bar{I}_x + \frac{\partial \bar{U}}{\partial t} \quad 2.38$$

where the overbar represents averaging of a quantity in the homogenous direction ( $z$ ) and the pressure is normalized by the density. The dimensionless variables hereafter are those that have been nondimensionalized by the channel half width,  $h^*$ , and twice the mean bulk velocity,  $2U_{avg}^*$  while dimensional variables are superscripted with a \*. In equation 2.38, the bulk Reynolds number,  $Re_b$ , is defined as

$$Re_b = \frac{2U_{avg}^* h^*}{\nu^*} \quad 2.39$$

and the  $\bar{I}_x$  term contains the terms that appear when the flow is nonhomogeneous in the streamwise direction where

$$\bar{I}_x = \frac{\partial(\overline{UU})}{\partial x} + \frac{\partial(\overline{UV})}{\partial y} - \frac{1}{Re_b} \frac{\partial^2 \bar{U}}{\partial x^2}. \quad 2.40$$

The derivation uses the following assumptions; a constant flow rate, symmetry with respect to the center plane, no streamwise and spanwise velocity at the wall ( $U = W = 0$ ), and homogeneity in the spanwise ( $z$ ) direction. This equation allows for suction and blowing at the wall in the wall-normal direction with the mean being zero ( $\bar{v}(x,0,z,t) = 0$ ) while the fluctuating term is not

necessarily zero. Integration of 2.38 in the  $y$  direction from 0 to 1 gives the relation between the pressure gradient and skin friction as

$$-\frac{\partial \bar{P}}{\partial x} = \frac{1}{8} C_f(x, t) + \tilde{I}_x \quad 2.41$$

where

$$C_f \equiv \frac{2\langle u_\tau \rangle^2}{(U_{avg})^2} = \frac{8}{Re_b} \left. \frac{d\bar{U}}{dy} \right|_{y=0}, \quad 2.42$$

and the overtilde denotes the integration

$$\tilde{f}(x, t) = \int_0^1 \bar{f}(x, y, t) dy. \quad 2.43$$

A substitution of 2.41 into 2.38 gives

$$\frac{1}{8} C_f = \frac{\partial}{\partial y} \left[ \overline{uv} - \frac{1}{Re_b} \frac{d\bar{U}}{dy} \right] + I_x'' + \frac{\partial P''}{\partial x} + \frac{\partial \bar{U}}{\partial t} \quad 2.44$$

with

$$f''(x, y, t) = \bar{f}(x, y, t) - \tilde{f}(x, y, t). \quad 2.45$$

The final relationship between skin friction and the Reynolds stresses can be determined with the use of integration by parts, the definition of the bulk mean velocity  $\tilde{u} = \int_0^1 \bar{u} dy = 1/2$ , and by taking a triple integration of 2.44, twice by  $\int_0^y dy$  to obtain the force balance and the mean velocity profile and lastly from  $\int_0^1 dy$  to obtain the flow rate from the velocity profile. The equation then becomes,

$$\frac{1}{2} = Re_b \left[ \frac{C_f}{24} - \int_0^1 (1-y)(-\overline{uv}) dy + \frac{1}{2} \int_0^1 (1-y)^2 \left( I_x'' + \frac{\partial P''}{\partial x} + \frac{\partial \bar{U}}{\partial t} \right) dy \right], \quad 2.46$$

and by isolating for  $C_f$ ,

$$C_f = \frac{12}{Re_b} + 12 \int_0^1 2(1-y)(-\overline{uv}) dy - 12 \int_0^1 (1-y)^2 \left( I_x'' + \frac{\partial P''}{\partial x} + \frac{\partial \bar{U}}{\partial t} \right) dy \quad 2.47$$

where the term  $12/Re_b$  is the contribution of the laminar flow, the second term is the turbulent contribution, and the last term is the contribution from the inhomogeneous and transient flow. For fully developed turbulent channel flow the equation reduces to,

$$C_f = \frac{12}{Re} + 12 \int_0^1 -2(1-y)(\overline{uv}) dy. \quad 2.48$$

Following the procedure presented by FIK, Rastegari & Akhavan (2015) developed the equation for skin friction in a turbulent channel with slip conditions at both the upper and lower wall. The bulk of the following discussion is built from their work with the addition of intermediate steps for clarity of derivation of the final solution.

The Reynolds Averaged Navier Stokes equation in the streamwise direction has a few additional terms when compared to the one over the smooth surface. This is because, in the immediate proximity of the wall, due to micro-textures of the SHS, Reynolds-averaged quantities have non-zero gradients in the streamwise direction. Pairs of streamwise and spanwise counter rotating vortices exist in proximity of the wall due to these non-zero gradients in the Reynolds stresses, thus  $\bar{V}$  and  $\bar{W}$  are non-zero in these regions (Perkins 1970; Rastegari & Akhavan 2013; Türk et al. 2014; Jelly et al. 2014).

$$\frac{1}{\rho} \frac{\partial \bar{P}}{\partial x} = \frac{\partial}{\partial x} \left( \nu \frac{\partial \bar{U}}{\partial x} - \overline{uu} - \bar{U}\bar{U} \right) + \frac{\partial}{\partial y} \left( \nu \frac{\partial \bar{U}}{\partial y} - \overline{uv} - \bar{U}\bar{V} \right) + \frac{\partial}{\partial z} \left( \nu \frac{\partial \bar{U}}{\partial z} - \overline{uw} - \bar{U}\bar{W} \right) \quad 2.49$$

For laminar flows, the equation is valid but the Reynolds stresses as well as  $\bar{V}$  and  $\bar{W}$  are zero due to the absence of fluctuating velocities.

Taking the average over the periodic pattern of the SHS microtextures in the streamwise and spanwise directions, denoted by  $\langle \rangle$ , and by integrating in the wall normal direction, 2.49 becomes

$$\langle u_\tau^2 \rangle \left( 1 - \frac{y}{\delta} \right) = \nu \left\langle \frac{\partial \bar{U}}{\partial y} \right\rangle - \langle \overline{uv} \rangle - \langle \bar{U}\bar{V} \rangle, \quad 2.50$$

where  $\langle u_\tau^2 \rangle$  is the average wall-friction velocity

$$\langle u_\tau^2 \rangle \equiv \sqrt{-\left\langle \frac{\partial \bar{P}}{\partial x} \right\rangle \frac{h}{\rho}}. \quad 2.51$$

A term by term integration of 2.50 from 0 to  $y$  and then from 0 to  $h$  and the use of the new boundary condition  $\langle \bar{U} \rangle|_{y=0} = U_s$  is applied.

Integrating the first term yields

$$\int_0^h \int_0^y \langle u_\tau^2 \rangle \left(1 - \frac{y}{h}\right) dy dy = \langle u_\tau^2 \rangle \int_0^h \left(y - \frac{y^2}{2h}\right) dy = \frac{c_f}{6} U_{avg}^2 h^2, \quad 2.52$$

and the second term yields

$$\int_0^h \int_0^y \nu \frac{\partial \langle \bar{U} \rangle}{\partial y} dy dy = \nu \int_0^h \langle \bar{U} \rangle dy = \nu h U_{avg} \left(1 - \frac{U_s}{U_{avg}}\right). \quad 2.53$$

Integrating the third term gives

$$\int_0^h \int_0^y -\langle \bar{u}\bar{v} \rangle - \langle \bar{U}\bar{V} \rangle dy dy, \quad 2.54$$

and by applying a substitution

$$a = -\langle \bar{u}\bar{v} \rangle - \langle \bar{U}\bar{V} \rangle \quad 2.55$$

and integration by parts where

$$b = \int_0^y a dy, db = a, dc = y, dc = dy, \quad 2.56$$

2.54 simplifies to

$$y \int_0^y a dy \Big|_0^h - \int_0^h ya dy = h \int_0^h a dy - \int_0^h ya dy = h \int_0^h \left(1 - \frac{y}{h}\right) a dy = h \int_0^1 (1 - \xi) a d\xi \quad 2.57$$

with  $\xi = y/h$ .

Combining the three solutions together give,

$$\frac{C_f}{6} U_{avg}^2 h^2 = \nu h U_{avg} \left(1 - \frac{U_s}{U_{avg}}\right) + h^2 \int_0^1 (1 - \xi) a \, d\xi, \quad 2.58$$

which can be simplified to

$$C_f = \frac{6}{Re} \left(1 - \frac{U_s}{U_{avg}}\right) + 3C_f \int_0^1 [-\langle \overline{uv} \rangle - \langle \overline{UV} \rangle]^+ (1 - \xi) \, d\xi. \quad 2.59$$

Isolating for  $C_f$  gives,

$$C_f = \frac{6}{Re} \left(1 - \frac{U_s}{U_b}\right) \left(\frac{1}{1 - 3I^+}\right) \quad 2.60$$

where  $I^+ = \int_0^1 [-\langle \overline{uv} \rangle - \langle \overline{UV} \rangle]^+ (1 - \xi) \, d\xi$ . For a smooth surface there is no slip velocity so the equation reduces to

$$C_f^0 = \frac{6}{Re(1 - 3I^{+0})} \quad 2.61$$

where  $I^{+0} = \int_0^1 [-\langle \overline{uv} \rangle^{+0}] (1 - \xi) \, d\xi$ .

Drag reduction is defined as,

$$DR = \frac{\Delta C_f}{C_f^0} = \frac{C_f^0 - C_f}{C_f^0} \quad 2.62$$

where  $C_f^0$  is the skin friction over a smooth surface,  $C_f$  is the skin friction over the tested surface.

Substituting 2.60 and 2.61 into 2.62, the drag reduction of a surface can be expressed as

$$DR = \frac{U_s}{U_b} + \left(1 - \frac{U_s}{U_b}\right) \left(\frac{3\epsilon}{1 - 3I^+}\right) \quad 2.63$$

Where  $\epsilon = I^{+0} - I^+$ .

This equation accounts for the contributions of the slip at the wall,  $(U_s/U_b)$ , and the contributions from the change in the turbulent dynamics and mean flows. This means that in laminar flows, the drag reduction is due entirely to the slip at wall,  $DR = U_s/U_b$ , as  $\epsilon = I^{+0} - I^+ = 0$ .

## 2.5 Measurement methods

### 2.5.1 Micro particle tracking velocimetry (Micro-PTV) and shadowgraphic particle tracking velocimetry (Shadow-PTV)

Particle tracking velocimetry (PTV) is an Euclidian method of using a particle position and a known time interval to determine its velocity. PTV, as the name suggests, tracks the location of a single particle across consecutive frames and uses the defined time interval (imaging frequency) to determine its velocity (Baek & Lee 1996), contrary to other visualization techniques such as PIV, which tracks a group of particles and their average displacement to yield the velocity. Figure 10 below shows the basic working principles of PTV. A recording device captures a region of interest illuminated by a laser sheet. Afterwards, the images are processed to increase the signal to noise ratio before a PTV algorithm is applied which tracks only particles with a specific size and intensity to ensure the tracking only occurs on the in focus particles. Over time various algorithms have been developed (Adamczyk & Rimai 1988; Hassan & Canaan 1991) that track and predict search locations for particles but before the algorithms can be deployed the images are typically processed to improve particle detection. The equipment required for a PTV setup involve tracer particles, camera(s) and lens(es), a light source, timing unit, PTV algorithm, optics, and a testing facility. Experiment may require different equipment for an optimal setup based on the principles of each of the equipment.

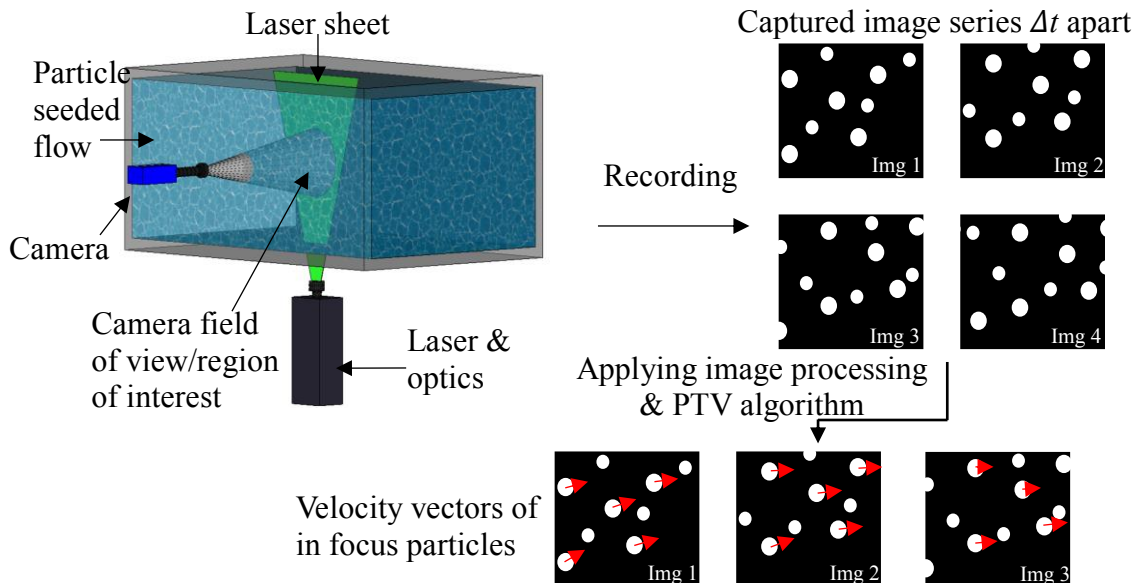


Figure 10: A schematic illustrating the principles of particle tracking velocimetry.



Shadow-PTV uses the same concepts as any other type of PTV but utilizes a different method of illumination. Instead of a laser sheet illuminating a thin region of interest, the region of interest is illuminated through backlight illumination. The captured images have a high intensity white background with low intensity black dots where the particles block the light. Figure 11 shows a simple shadow-PTV setup with the illumination source placed far enough away so the viewing plane has similar intensities across the image.

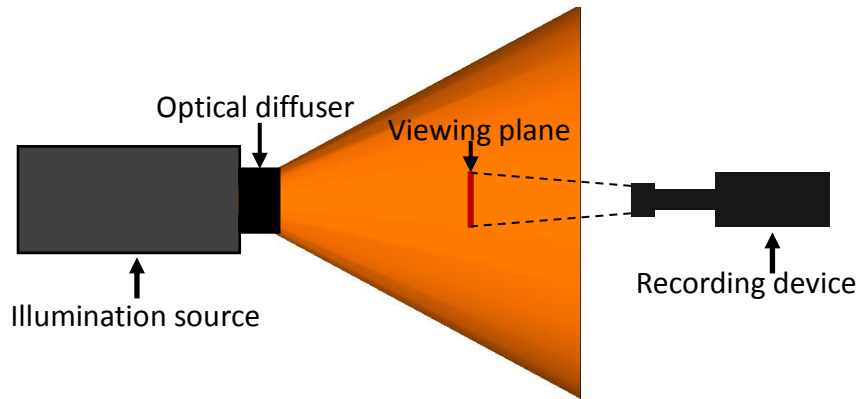


Figure 11: An illustration of the top view of a basic shadow-PTV setup.

### Tracer Particles

Tracer/tracing particles are used to represent the motion of the flow but they must have the correct properties to follow the fluids motion. Tracing particles should be chosen based on four main criteria; density, material, size, and shape, in conjunction with their application seeding density requirements. PTV measurements are best performed with a low seeding density while medium seeding density is more optimal for particle image velocimetry measurements and a high seeding density for use in laser surface velocimetry (Stegeman 1995).

### Density of Tracer Particles

The density of the particle is important because in the near wall region if the particles have a density greater than that of water, due to their own inertial effects the particles will continue a motion that does not match the motion of the fluid. At the wall locations this will result in seeing a velocity when one should not exist. Assuming perfectly spherical particles with a diameter,  $d_p$ , the velocity due to gravity,  $U_g$ , can be expressed as

$$U_g = d_p^2 \frac{\rho_p - \rho_f}{18\mu} g, \quad 2.64$$

where  $\rho_p$  and  $\rho_f$  are the density of the particle and fluid respectively, and  $g$  is acceleration due to gravity (Raffel et al. 2007).

#### Material of tracer particles

There are three factors worth considering when choosing the tracer particle material. The first is the materials refractive index as the ability to scatter light is a function of the refractive index of both the particle and surrounding fluid (Raffel et al. 2007). The second is the materials transmittance, the ability to allow light through. The transmittance and refractive index ratio affect the scattering of light through the particle. When the light hits a particle, scattering of light in every direction occurs which can lead to multi-scattering effects. The recording device must be positioned appropriately to mitigate these effects. The last factor is the material compatibility with the surrounding test domain. A particle harder than the material of the testing domain will wear or damage it over time depending on the fluid velocity and duration. Likewise, a softer material may be damaged during collisions causing its shape and size to change over time.

#### Shape and size of tracer particles

The shape and size of the tracer particles are important because if they are not the correct size they will not follow the flow as shown by equation 2.64. Additionally the particle size directly affects the spatial resolution of the system. An ideal particle should be as small as the experiment permits, preferable at least one order of magnitude smaller than the structures of study in the flow. The particles must also be neutrally buoyant to be suspended in the flow without rising to the top or sinking to the bottom due to lift and drag effects based on their surface area (Stegeman 1995). Another limitation on the shape and size of the particle is that they both affect the intensity of the reflection towards the sensor. Particles which are too small may cause low illumination while larger particles could saturate the image or have multi-scattering effects. Spherical tracer particles should be used when applying Mie's scattering theory to determine the intensity of reflected light on the sensor.

The tracing particle size should also take up 3 to 8 pixels on the sensor because if the shift of the particles between two images is smaller than one pixel the processing method can perform poorly due to the inability to detect the displacement of the particles. However, newer tracking algorithms and methods can have subpixel accuracy (Nobach 2004) . A rule of thumb for tracking particles is that the displacement between two frames should be greater than the diameter of the particle

(Kurada et al. 1993). Lastly, to ensure the correct particles are being matched between the two frames, the spacing between particles should be 2-3 times the displacement of the particles between the two frames (Stegeman 1995).

#### Mixing of tracing particles into system

The tracer particles in the system should be of equal size and shape to give a more consistent image for algorithm detection. Larger particles reflect more light causing the correlation methods to be skewed if it is surrounded by smaller particles. It is favourable to mix the particles in a solution of the working fluid and left to sit to allow larger particles to settle at the bottom. This allows for more consistent particle size and density as heavier particles are not added into the experiment.

#### Concentration of tracing particles

The concentration of the particles determines the special resolution of the measurements. However, the concentration should not be high enough to affect the properties and flow characteristics of the fluid. Having a particle concentration between  $10^9$  and  $10^{12}$  particles per cubic meter of fluid will change the flow characteristics or fluid properties (Raffel et al. 2007).

### 2.5.2 Recording devices and lenses

Imaging systems primarily use charge coupled device (CCD) cameras. A CCD has an array of single elements called pixels that make up the sensor. Each pixel of a CCD cameras converts light to an electric charge. The performance of CCDs depend on its resolution, exposure time, and spectral quantum efficiency (Jahanmiri 2011). The recording device was chosen in accordance with the Reynolds number and the size of the region of interest. Two sensors of the same size can have different resolutions depending on the size of the pixels. Smaller pixels result in higher resolution as the information will have greater detail. The exposure time of the camera should be short enough that a fluid element can be captured multiple times before exiting the region of interest. Lastly, the spectral quantum efficiency (SQE) for a given wavelength is the rate at which incoming photons are converted to electrons. When the SQE is low, a longer exposure time is required to separate the signal from the noise.

The location of the camera with respect to the imaging plane will affect the magnification,  $M$ , field of view (FOV), and depth of field (DOF). Lens attachments can correct and adjust the incoming light to meet the desired parameters  $M$ , FOV, and DOF. The diffraction of light from a small

particle on a pixel is not uniform therefore the particle will appear bigger than in reality. Figure 10 below shows the effects of diffraction on the sensor as well as the dimensions for determining  $M$ , FOV and DOF shown in equations 2.65 to 2.67 below.

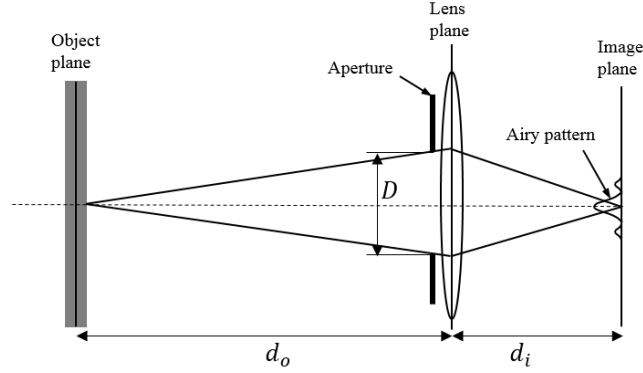


Figure 12: An illustration showing diffraction effects during imaging of particles.

$$M = \frac{d_i}{d_o} \quad 2.65$$

$$d_i = (1 + M)f \quad 2.66$$

$$d_o = \left(1 + \frac{1}{M}\right)f \quad 2.67$$

where  $d_o$  is the object distance to the lens,  $d_i$  is the image distance from the lens, and  $f$  is focal length.

Due to diffraction the effective diameter of the particle seen on the sensor,  $d_e$ , is a function of both the magnification and diffraction effects. The effective diameter can be determined as

$$d_e = (M^2 d_p^2 + d_{diff}^2)^{1/2} \quad 2.68$$

where  $d_p$  is the particle diameter and  $d_{diff}$  is determined by

$$d_{diff} = 2.44 f_{\#} (M + 1) \lambda \quad 2.69$$

with  $\lambda$  being the wavelength of light and  $f_{\#}$  is the aperture setting defined as  $f_{\#} = f/D$ .

The DOF is the thickness in which particles will be determined to be in focus. It can be determined using the equation,

$$DOF = 4 \left(1 + \frac{1}{M}\right)^2 f_{\#} \lambda. \quad 2.70$$

To avoid out of focus particles, the DOF should be less than the thickness of the laser sheet.

### 2.5.3 Light sources and timing

A typical PTV setup uses a laser because of the ability to emit high energy density monochromatic light which can easily be formed into thin sheets and the reflected light from tracer particles avoid the issue of monochromatic aberrations (Raffel et al. 2007). As mentioned before, the wavelength of the emitted light plays a large factor based on the spectral quantum efficiency of the recording device. A wavelength not in the optimal band will result in a lower signal to noise ratio. The intensity of the light source should be varied depending on the exposure time as a single pixel in a CCD has a maximum amount of electrons it can produce in one picture. Too high of an intensity (or exposure time) will lead to saturation of the image. Achieving a quality image required timing the laser pulses to align with the camera shutters so the overall image brightness was constant between image pairs. A typical timing diagram for a PTV system operating in dual frame mode is shown in Figure 13. There exists a minimum particle displacement in the boundary layer between the image pairs for accurate measurements. If the particles in the boundary layer do not have at least one pixel of displacement between the frames, the velocity is hard to detect with PTV algorithms and is subjected to subpixel tracking which can have errors on the same magnitude as the detected displacement. Ensuring both frames have equal intensity helps the PTV algorithm accurately track particles. This is done by reducing the laser power on the second pulse as the exposure time of the second frame is larger than the first and will collect more light.

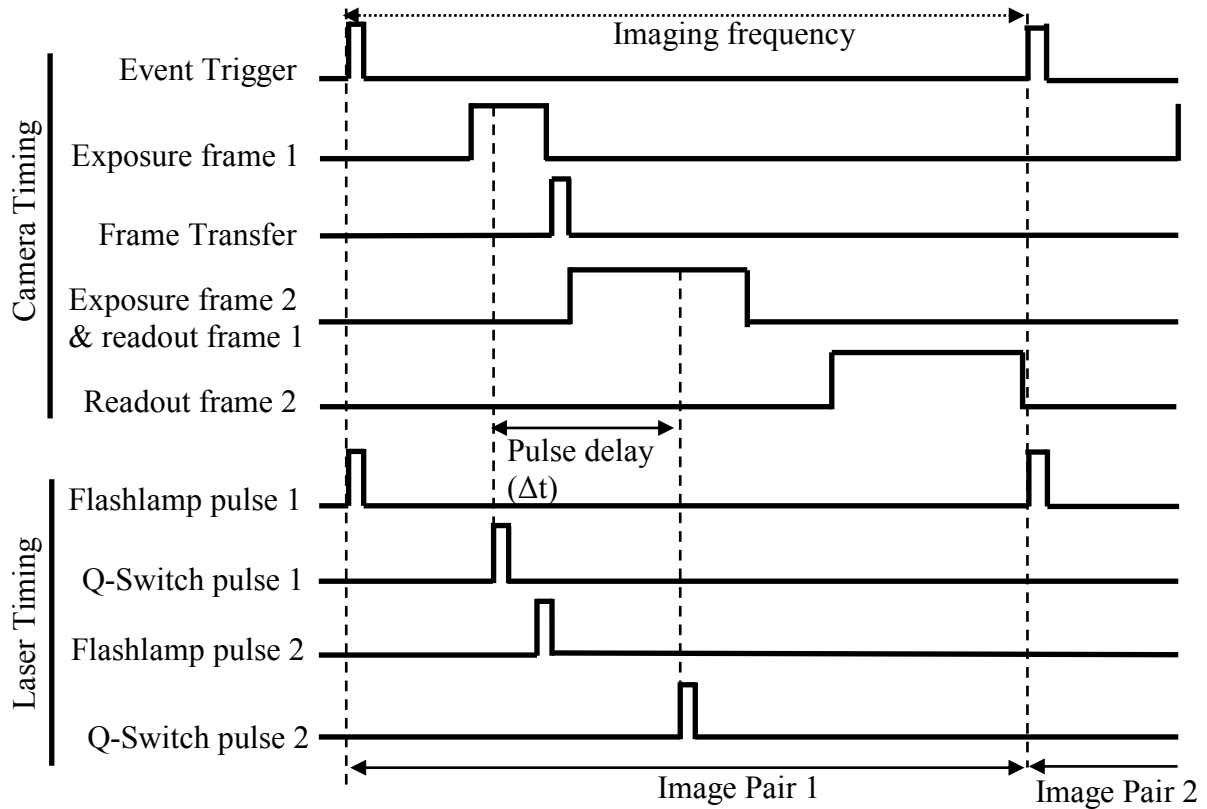


Figure 13: A timing diagram of events for a typical PTV system capturing image pairs.

#### 2.5.4 Image quality

Preceding operation of the PTV algorithm, the images must be processed to improve image quality to help the algorithm locate and track individual particles, as there are a myriad of factors that affect the quality of the results. The brightness, contrast, illumination uniformity, and image sensor noise are factors that need to be looked for image quality. The processing method and parameters also required extensive testing through trial and error to find the parameters that work the best together. Ideally, the images will have a black background with only the light reflected by the particles showing as white pixels. However, laser flare and thermal effects of the camera produce electrons which are captured by the sensor and affect the background brightness (Raffel et al. 2007). A second source of noise is the readout-noise, which is introduced during the charge-to-voltage conversion of each image. These sources of noise will appear on the images as a constant noise on each pixel. Noise from thermal effects can be reduced with improved cooling methods such as cryogenic cooling while the readout noise is lower at lower scan rates.

### 3 Experimental setups

The experimental setup for measuring the performance of SHSs in both the laminar and turbulent flow regime are discussed below. This section is as follows; an overview of the laminar channel, a breakdown of the components, an overview of the turbulent channel, a breakdown of the components, and a description of the PTV processing parameters.

#### 3.1 Laminar flow loop setup

The laminar flow loop shown in Figure 15 was a closed loop system comprised of; a millimeter-scale channel with a test section, a pumping mechanism, and a reservoir. A motorized syringe pump applied a suction force that drew the working fluid from the reservoir, through the channel and measurement domain, into the syringe. Measurements were carried out at a bulk Reynolds number,  $Re_b$ , of 50 - 450 corresponding to pressures of 1373 - 1435 Pa below atmospheric. A shadow-PTV system was used to characterize the flow. Data acquisition lasted between one to nine minutes depending on the flow conditions required.

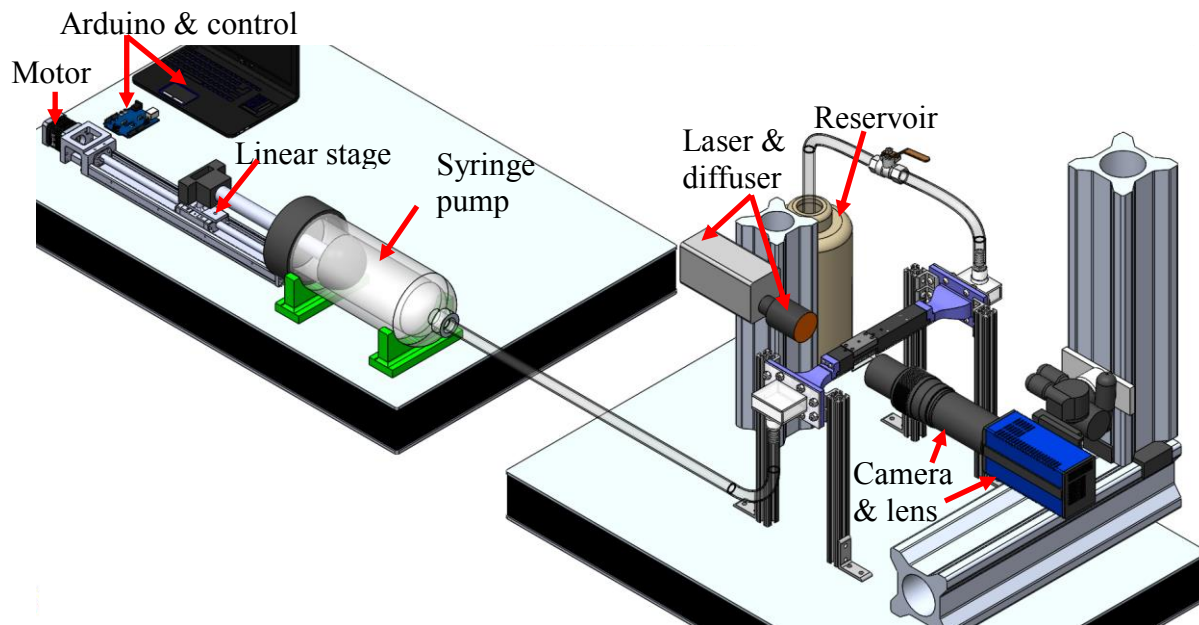


Figure 14: An image of the experimental setup for the testing of superhydrophobic surfaces in a laminar flow.

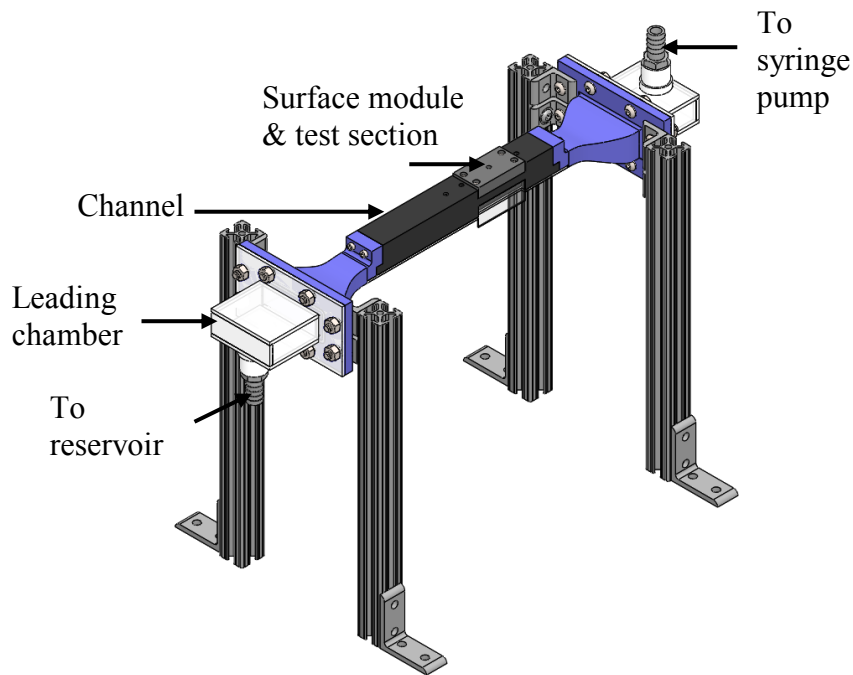


Figure 15: An illustrated image of the channel and encompassing assemblies.

### 3.1.1 Pumping system

Typically, electric pumps drive and circulate the flow in water channels. Due to the size of the channel and the necessity to be in the laminar regime, an electric pump was not ideal. Small pulsations from the impellor of the pump would be significantly magnified in the channel due to its cross sectional area. Secondly, vibrations from the electric pump interfere with the imaging quality because small vibrations of the camera cause shifting of the plane of focus meaning particles will be lost or appear out of focus between images. The design instead used a large plastic syringe controlled by a stepper motor. The syringe, shown in Figure 16, had an inner diameter of 87.4 mm and a working distance of 250 mm, corresponding to a working volume of 1.5 L and a maximum channel flowrate of 15.4 mL/s ( $Re = 600$ ) for two minutes. Silicone was applied to the outside of the rubber plunger which created a tight seal between the plunger and inside of the cylinder. A waterproof grease was lightly coated onto the inside of the cylinder allowing for smoother travel of the plunger while maintaining the airtight seal. The syringe tip had an inside diameter of 31.75 mm and was joined with hosing connected to the exit chamber of the channel. Two custom 3D printed syringe holders with a radius of 46.5 mm, designed for preventing the syringe unit from moving during activation of the plunger, were placed at both the front and back



of the outside cylinder. The front support prevented motion when the plunger was pulled while the back support prevented motion when the syringe was pushed.

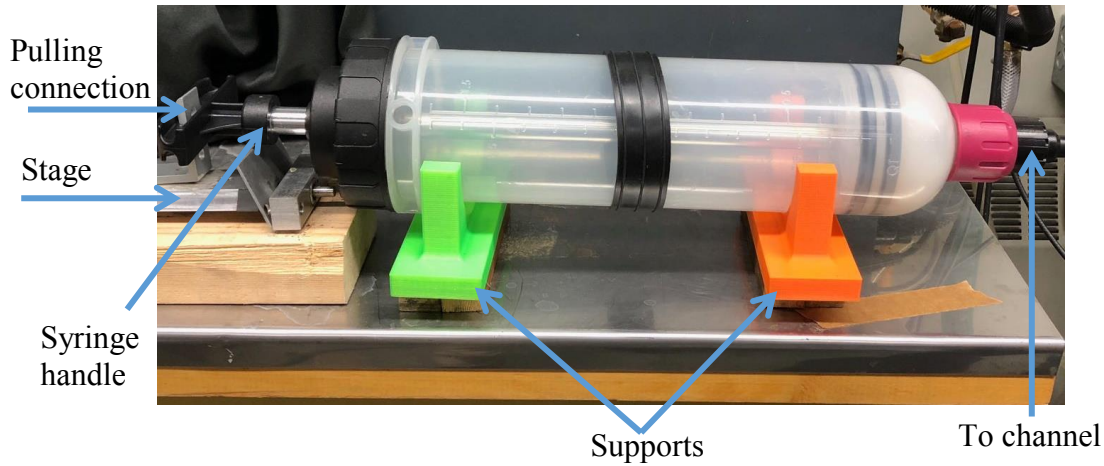


Figure 16: An annotated image of the syringe pump used to drive the laminar channel flow.

Driving the syringe was a 128 oz-in NEMA-23 unipolar stepper motor wired through a breadboard to an Arduino UNO R3 microcontroller, shown in Figure 17. A CX 430, Corsair power supply wired to the breadboard, powered the system. The Arduino IDE software was used to develop a code that controlled both the number of rotations, and the speed of the rotations of the motor. There were limitations between the NEMA motor and the Arduino IDE program that gave a minimum rotation speed that provided a smooth and consistent rotation of the motor. The slowest rotation speed provided a flow of  $Re_b = 10$ . The motor shaft was fit into a lead screw mechanism, shown below in Figure 17, by a series of set screws. The lead screw had a stage that traversed the double threaded rod and had a working length of 270 mm. A custom 3D printed part fastened into the stage and was fit into the handle of the plunger. Depending on the direction of the motor rotation, the handle pushed or pulled the plunger to drive the flow. The motor was fastened into a wooden block that was firmly clamped onto a separate table. This prevented vibrations from the motor from affecting the measurement equipment. A single rotation of the motor resulted in a linear displacement of 1.27 mm of the plunger, which equated to a displacement of 7.62 mL.

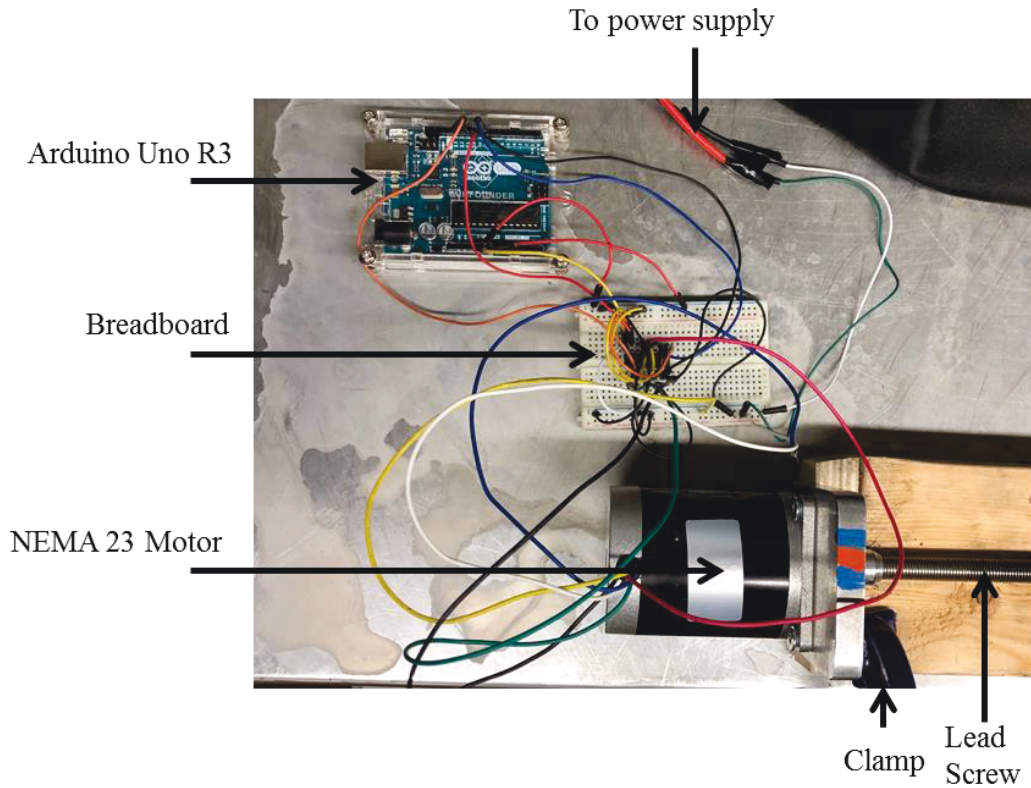


Figure 17: An annotated image of the operational components controlling the syringe pump.

### 3.1.2 Measurement channel

The channel, shown in Figure 18, was designed for flows in the laminar regime. During experiments, the channel was oriented so that the surface module was a part of the top wall. For visual clarity, Figure 18 shows the channel with the surface module as part of the bottom wall. The channel consisted of an anodized aluminum base, and clear scratch-resistant glass on the top and sides. The aluminum base was chosen for its cost effectiveness as aluminum has a low weight and the channel did not support any load. Machining of the aluminum was done to provide a smooth surface finish to keep the channel height even along the full length of the channel. The anodized coating was added to prevent the aluminum from rusting while the material of the two sidewalls to measure the flow through were made from microscopic slides based on their excellent optical properties. The glass top was made from one inch thick clear glass to allow the user to see if air bubbles or other debris were present and/or interrupting the flow during experimentation. The thickness of the glass prevented bending or deformation of the channel in both positively or negatively pressurized conditions. Lastly, the glass top allowed for other measurement techniques

that require a laser sheet perpendicular to the surface. The hosing connected to the leading chamber and exit chamber was made of clear transparent PVC for the benefit of allowing the user to see if any large debris was in the flow loop. The clear PVC also allowed the user to see if the tracer particles had started to settle in the hosing which notified the user to re-mix the particles into the water. To flush the system, the motorized syringe pumped distilled water between the reservoirs at a high speed which removed settled particles from the hosing, channel, and connections.

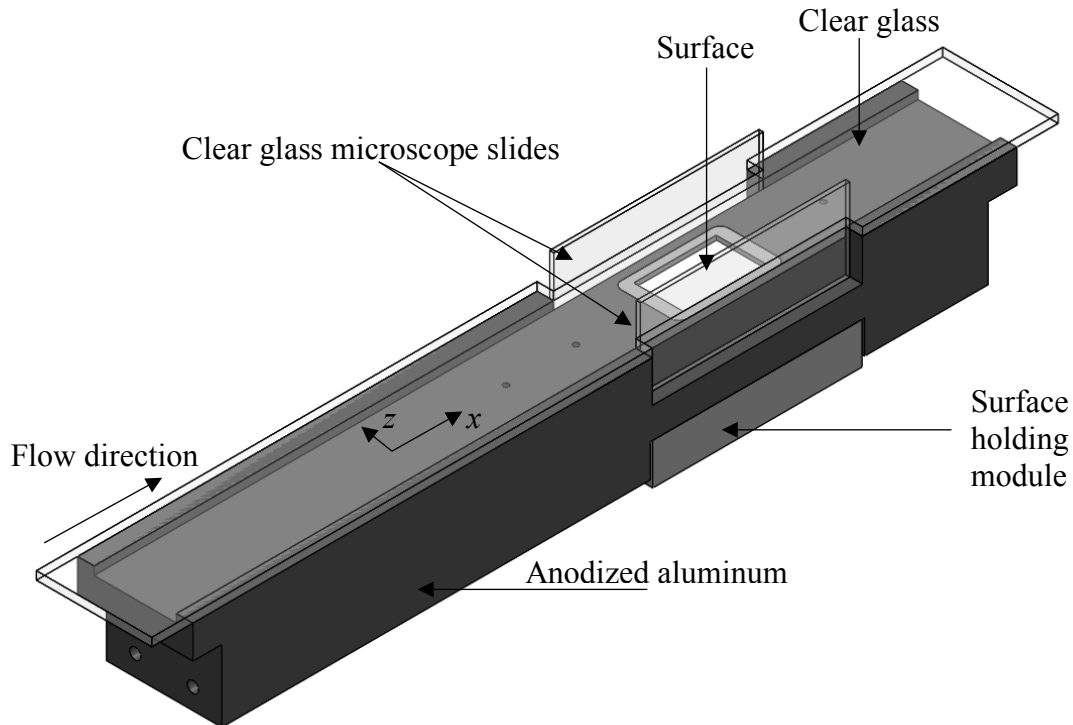


Figure 18: An annotated image of the channel assembly.

Figure 19 shows the dimensions of the channel. The channel was  $20 \text{ mm} \times 2 \text{ mm}$  ( $w \times h$ ), giving an aspect ratio of 10. The channel length was  $280 \text{ mm}$  ( $140h$ ) with an entrance length of  $124 \text{ mm}$  ( $62h$ ). The channel supports flowrates ranging from  $1.1 \text{ mL/s}$  to  $15.4 \text{ mL/s}$  corresponding to a bulk Reynolds number of 100 to 500. Prior to the entrance of the microchannel was a mesh grating made from plastic drinking straws to remove vortices, turbulent motion, and fluctuations from the flow due to the sudden expansion from the hosing to the leading chamber. The channel had a  $26 \text{ mm} \times 16 \text{ mm}$  ( $L \times W$ ) opening where a surface holding module was inserted. The module fastened with socketed screws into the anodized aluminum base. The surfaces were placed far enough downstream from the inlet to ensure the flow was fully developed. The surfaces were also

located far enough away from the exit of the channel to prevent exit effects from interfering with the performance of the surfaces.

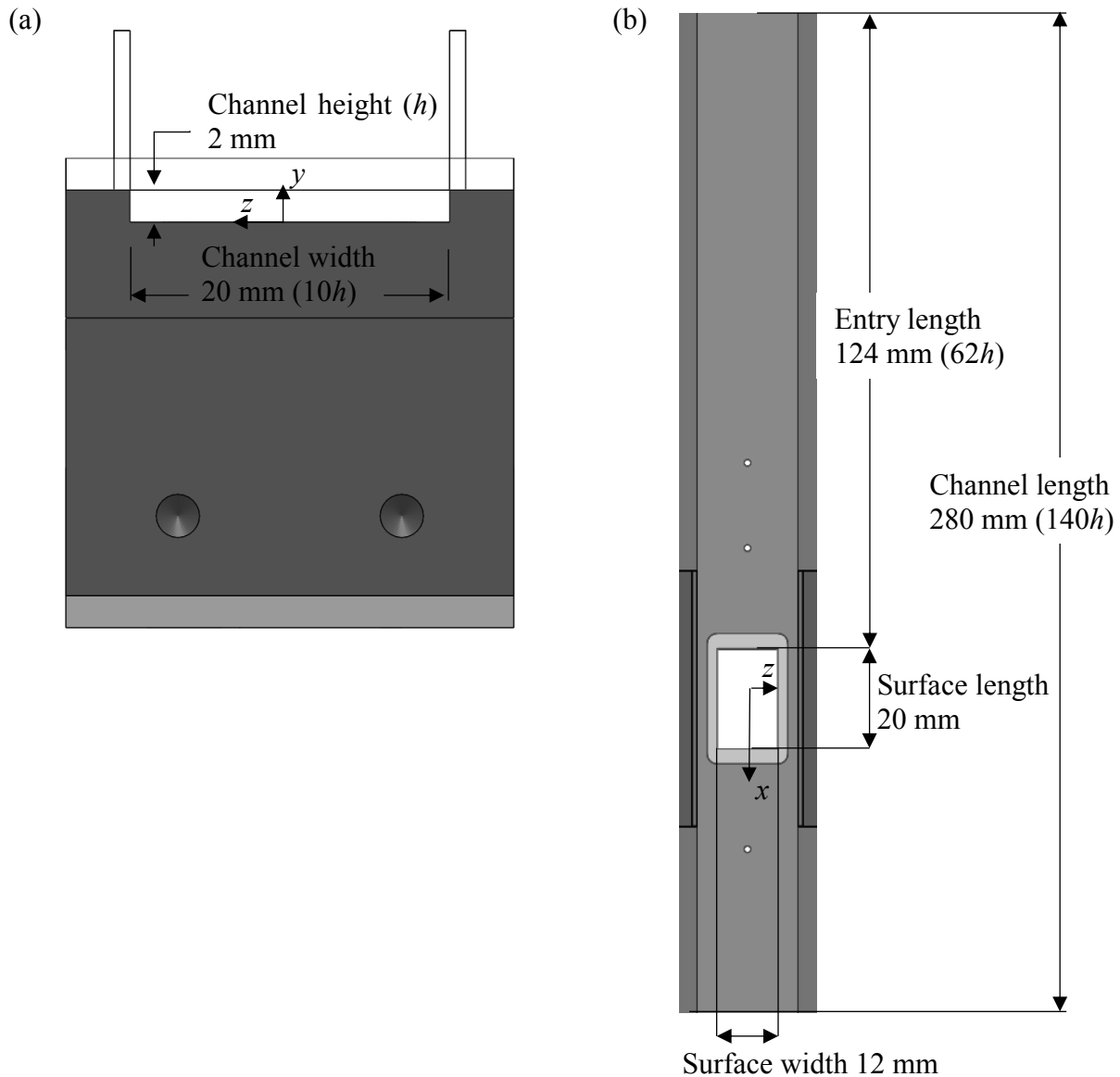


Figure 19: (a) Dimensioned front view of the channel. (b) Dimensioned top view of the channel.

Ensuring the flushness between the test surface and the channel surface was of major importance for two reasons. Firstly, if the transition between the channel to the surface was not even, the edge would trip the flow causing it to no longer remain a fully developed laminar flow. Secondly, an uneven transition would mean there was an uneven channel height and therefore the velocity will change in the  $x$  direction, as the flow will accelerate or decelerate which changes the tracer particles' velocity vector over the lengths of the surface. Both of these reasons meant that the utmost care

was to be taken when aligning a surface for testing. To solve these problems, an adjustable surface carrier was designed, as shown in Figure 20. The holding module was 3D printed (J735, Stratasys) and made from translucent RGD720, a multi-purpose PolyJet photopolymer that is translucent.

The translucent material allowed for preliminary viewing of the surface to check it was level and flush before insertion into the channel. The surface module was sanded with ultrafine, 600 grit sandpaper to remove roughness on the leading and trailing edges around the test surface. There was a 0.02 mm tolerance between the outside walls of the surface carrier and the inside of the channel. After aligning of the surface inside the channel, a rubber plug was inserted into the hole on the bottom of the holding module to maintain a closed loop system. Inside the holding module was a 20 mm × 12 mm plate (surface carrier) attached to a screwing mechanism that allowed for adjustability of height. The adjustability allowed for a test surface with a maximum thickness of 3.15 mm to sit flush in the holding module. Double-sided, waterproof M3 tape secured the test surfaces to the surface carrier. To keep the surface level on the carrier, two strips of the tape were evenly spaced across the carrier. The surface carrier was printed with the same material as the holding module and was sanded with the same ultrafine sandpaper. This was important because a small amount of buildup on the carrier would cause the surface to sit unevenly. The bottom of the carrier had a conical opening to slide in the lifting mechanism with a tolerance of 0.25 mm on any side. The conical shape maximized the contact area between the lifting mechanism and the carrier, and the opening allowed for easy separation and replacement of parts when they wore. The shape and tight tolerance between the lifting mechanism and surface carrier minimized the degrees of freedom between the two so the pressures in the channel would not move the surface carrier during data acquisition. The lifting mechanism was 3D printed with translucent RGD720. It was designed as a threaded base that screwed into the holding module and had a conical head that slid into the surface carrier. The bottom of the threaded base had a 3 mm deep hexagonal hole that allowed for height adjustment using a hex key. A single rotation of the screw shifted the carrier a distance of 0.5 mm. The lifting mechanism had a height of 9 mm and a maximum head diameter of 9 mm.

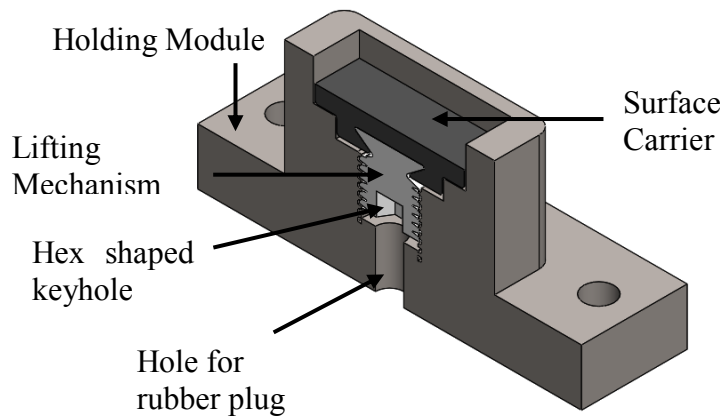


Figure 20: A cross sectional image of the surface holding assembly used in the channel.

### 3.1.3 Leakage prevention

Leakage was a major challenge the design faced. A gap or broken seal between two members caused the introduction of air bubbles and loss of the pressure in the channel. Keeping the channel free of these air bubbles was important for a few reasons. Due to the size of the channel, an air bubble with a diameter of 0.5 mm would take up 25% of the image during the data acquisition stages. In addition, the air bubbles had the ability to attach to the anodized aluminum or worse, the test surface. This prevented collection of data near the wall over test surfaces and caused a reflection of the light preventing data acquisition around the air bubble due to uneven lighting intensities and in some cases, image saturation. Most importantly, having a bubble in the channel interrupts and changes the flow field. Preventative measures were taken to reduce the possibility of air bubbles being introduced to the flow. All hosing was sealed airtight with Teflon tape and a hose clamps. Connecting components were fastened together using bolts and nuts with an O-ring between them. The outsides of the pieces were additionally sealed using clear Silicone I (GE) as a secondary seal in the case of O-ring failure. The one inch clear glass had additional clamps pressing it into the anodized aluminum, which kept it airtight and provided additional support from the pressure in the channel. The only component with the ability to be removed was the surface holding module. It was fastened with screws into the aluminum, sealed with an O-ring, and had a rubber plug inserted to prevent leaks through the holding module.

Due to the small field of view, any vibrations of the camera or channel were noticeable due to the system magnification. Mitigation of vibrational effects during experimentation was taken into

consideration by mounting and fastening both the experimental setup and the PTV setup on an optical tabletop 1.75 m long, 0.75 m wide, and 0.15 m thick. Sources of vibrations were the motor driving the syringe, the other laboratory experiments, and the cooling fan of the camera. The first two sources were mitigated by placing the motor and syringe on a separate table and only collecting data when no other equipment was running. Mitigation of the camera fan vibrations was much more challenging. The fasteners on the camera were tightened as much as possible to reduce the motion caused by the fan.

#### 3.1.4 Shadow-PTV

Backlight illumination of the channel was done with the Solo III (New Wave Research) and image recording was done with the FlowMaster3S (FM3S) (LaVision). The CCD had  $1280 \times 1024$  pixels with an individual pixel size of  $6.7 \mu\text{m} \times 6.7 \mu\text{m}$  which gave an aspect ratio of 5:4. Each pixel had a large well depth (25,000 electrons) which was important in the prevention of sensor saturation and damage because the majority of the backlight illumination went directly to the sensor and with a minor portion being impeded by the particles. The CCD also featured a 2-stage Peltier cooling coupled with forced air cooling, a scan rate of 12.5 MHz, a 12-bit data depth, and a readout frequency of 8 fps. The 12-bit data depth provided 4096 counts of light intensity to allow for better contrast between noise, out of focus particles, and in focus particles. The larger counts were also advantageous as there was a lower noise to signal ratio arising from thermal effects, and readout noise ( $7e^-$ ). The FM3S had two modes of operation, standard, and double shutter mode. The double shutter feature was used for PTV measurements and had a minimum delay of 200 ns. The FM3S was triggered by an external trigger event controlled by the Davis 7.3 software giving the user the ability to set the timing between frames as well as the frame acquisition rate. The FM3S was fitted with a “C” Mount coupler followed by a 2.0 X adapter (Navitar 1-6030) and finally a 12 X zoom, 12 mm fine focus lens (Navitar 1-50486). The focal length was 12 mm at an aperture setting of  $f/11$  based on the thin lens assumption (Steck 2015). The field of view was  $3.07 \text{ mm} \times 2.46 \text{ mm}$  in the streamwise and wall-normal direction respectively with a digital resolution of  $2.41 \mu\text{m}/\text{pix}$ , a magnification of 2.77, and a DOF of  $49.4 \mu\text{m}$ .

The laser type was an Nd:YAG operated in pulsed mode. The pulse separation time,  $\Delta t$ , was varied between  $380 \mu\text{s}$  to  $3100 \mu\text{s}$  in order to achieve a midstream displacement of 50 pixels at each  $Re$ . At the primary wavelength of the laser, the FM3S operated with a spectral quantum efficiency of

40%; however, the beam diameter produced by the laser was only 4 mm. The laser was fitted with an orange (620 nm) tinted optical diffuser at which the FM3S operated with a SQE of 23%. The optical diffuser was tested to have a divergence of at least 20°. Due to a Gaussian intensity distribution of the laser beam, the laser was positioned 227 mm from the center of the channel, resulting in a final beam diameter at the region of interest of 165 mm. This allowed the incident light on the region of interest to have negligible changes of intensities across the entire image.

The particles used for tracing were VESTOSINT 2070 natural color particles. These particles were also chosen based on their cost, material, and shape. The chosen particles have a density of 1.016 g/cm<sup>3</sup>, within the density of the working fluid by 2%, and was made from a polyamide-12 fine powder. The polyamide material was softer than metal and was less abrasive to improve the lifetime of the test surfaces. The polyamide powder was opaque and had an average particles diameter of 5 µm (2.1 pix) which provided a spatial resolution to capture the flow in the near wall region. For optimal PTV tracking, the center-to-center distance between particles should be two times the maximum particle displacement between frames (100 pix). For the sensor size an optimal seeding density should have a maximum of 132 in focus particles evenly spaced. The maximum seeding density was therefore 9.2 mg/L, or 13.8 mg total. To avoid over seeding the flow, 7 mg of the tracer particles were added. The particles were mixed into the working fluid using a blender and afterwards were poured into a 2 L glass beaker and left for 4 hours which allowed particles of larger density to settle towards the bottom.

Calibration of the PTV system was important to ensure the camera was in focus at the mid channel width, provide the conversion from physical to image space, and to ensure each frame of the images had similar illumination intensities. During the calibration steps, the laser power was always on low power to avoid permanent damage of the camera sensor and/or the users' eyes from having too high a power. This was especially important for the shadow PTV setup because the laser was directly across from the camera and the light was fired directly at the sensor. A reference target with 0.100 mm ± 0.005 mm diameter points separated a distance of 0.500 mm was used (make model) shown in Figure 21. The target was mounted in the surface module and lowered into the center (spanwise) of the channel, and elimination of refractive effects was done by filling of the channel to simulate viewing of particles. Having the target in the center of the channel ensured the boundary effects of the side walls did not play a role in the flow in the viewing plane. Distortion



effects caused by oblique viewing were mitigated by checking the camera and channel for levelness with respect to the mounting table and one another. Levelness of the camera reduced oblique viewing errors from and ensured the viewing plane was in the same spanwise location across the entire image. In addition, by ensuring the channel was level, gravitational effects in the flow caused from one end being raised compared to the other were removed preventing additional hydrostatic pressure at the test section.

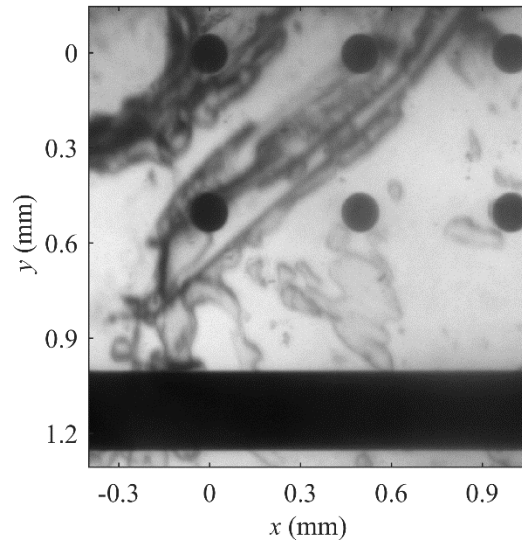


Figure 21: An image of calibration using the calibration target for the Shadow-PTV setup.

The shadow PTV setup collected 500 image pairs at a rate of 4 Hz with a frame separation between  $380 \mu\text{s}$  to  $3100 \mu\text{s}$  depending on the  $Re$ . The images were processed in Davis 7.3 (LaVision GmbH). The image intensities were inverted before processing to remove constant background noise. The minimum of the ensemble of the images was found and subtracted from each individual image. To further increase the signal to noise ratio, a multiplication of each pixel by a constant value (600) was performed before division by the average of the ensemble. On each of the images, a sliding minimum with a kernel of 3 pixels was applied, followed by intensity normalization by the average over a kernel size of 100 pixels. To reduce peak locking effects, a Gaussian smoothing with a kernel size of  $3 \times 3$  pixels was applied. The PTV algorithm that was performed consisted of two steps, particle detection, and particle tracking. A minimum intensity threshold as well as a pixel size threshold was applied to improve detection of in focus particles versus noise or out of focus particles. The minimum intensity requirement of a group of pixels was 425 counts and the particle size restriction was 3 - 7 pixels. The size restriction was applied based on the results from Kähler et al. (2012) who showed that particles with a smaller size than 3 pixels can cause a peak

locking effect while the particles larger than 7 pixels are a result from being out of focus. The maximum displacement seen was 51 pixels in the streamwise direction and  $< 1$  pixel in the wall-normal direction at the center of the channel between image pairs. To remove erroneous particle tracking, a restriction of particle displacement was set to  $30 \pm 30$  pixels in the streamwise direction and  $0 \pm 2$  pixels in the wall normal direction. These limits were verified based on the spatial resolution of the camera (0.0024 mm/pix), the bulk flowrate of the channel (0.3 m/s), and the frame separation (380  $\mu$ s) which show an expected 47 pixel maximum displacement in the streamwise direction.

### 3.1.5 Surface fabrication and characterization

NeverWet (NW) (Rustoleum) is an aerosol based superhydrophobic coating that was applied through direct spray coating onto a surface. NW has two layers, a primary base layer, and a top coat. The base layer acts as an adhesive layer between the top coat and the desired surface and contains large particles which agglomerate when the solvent evaporates forming a solid layer. The top coat is a silicone based coating which contains smaller particles than the base layer. The chemicals in the top coat contain the antifouling and hydrophobic properties (Gupta et al. 2016). It was seen that the performance of the NW surfaces changed based on the coating procedure used. A coating procedure was developed to improve the repeatability of NW by spraying similar topographies for each test surface. One pass of the base layer was sprayed over the aluminum from left to right at a height of 20 cm and allowed to dry for 30 minutes. Three passes of the top coat were sprayed at a height of 20 cm with 5 minute intervals between each pass. The surface was allowed a minimum of 12 hours to dry and was tested within 24 hours of coating.

The contact angle of the surface was determined using the sessile drop technique (Dimitrov et al. 1991) with a drop shape analyzer (DSA-100 KRÜSS GmbH). Figure 22 shows an image of a 10 $\mu$ L droplet on a SHS at 23°C. The needle was descended 1 mm from the surface before the droplet was formed at the tip, after which was lowered until the droplet was in contact with the surface. The needle was then raised from the surface until the droplet was no longer on the tip of the needle. Due to the low surface energy of the SHS, the droplet often times did not leave the needle tip because the capillary forces were larger than the affinity between the droplet and the surface. In these cases the volume of the droplet was increased until the gravitational forces overcame the capillary forces; however, the additional kinetic energy stimulates an increase in apparent wetting

(Krüss 2004). Mitigation of the additional kinetic energy effects was done by minimizing the distance between the droplet and the surface. The contact angle shown has been fitted with the parameters of an ellipse shaped drop with a tangent line from the ellipse to the flat surface. The average contact angle from 10 measurements at varying locations on the SHS and smooth surface was  $153.5^\circ$  and  $91.1^\circ$ , respectively.

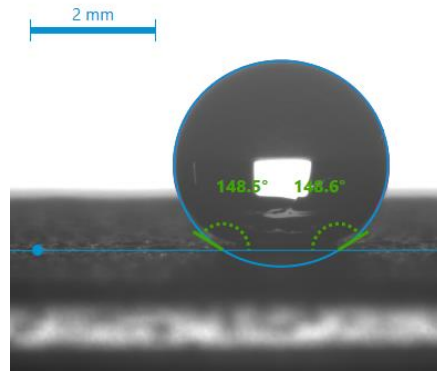


Figure 22: An image of the contact angle between a  $10\mu\text{L}$  water droplet and the SHS.

The particle size of the SHS was examined through scanning electron microscopy (SEM) using a EVO MA10, Zeiss. Figure 23 shows the SHS at a magnification of 100 and 250 times. The surface consists of an underlying layer, the base coat of the NW spray, which has cracks throughout. The smaller particles are randomly dispersed and bonded to this layer and provides a varying roughness across the surface. While viewing the surface, individual particles as small as  $5\ \mu\text{m}$  and clusters of particles with a grouping diameter of up to  $80\ \mu\text{m}$  were seen. To preserve the surface topology while viewing the surface there was no metal sputtered on the surface. This results in viewing areas where charge accumulates and appears brighter than the surrounding areas. This accumulation of charge on a surface under the SEM, if not careful, could melt or deform the surface itself.

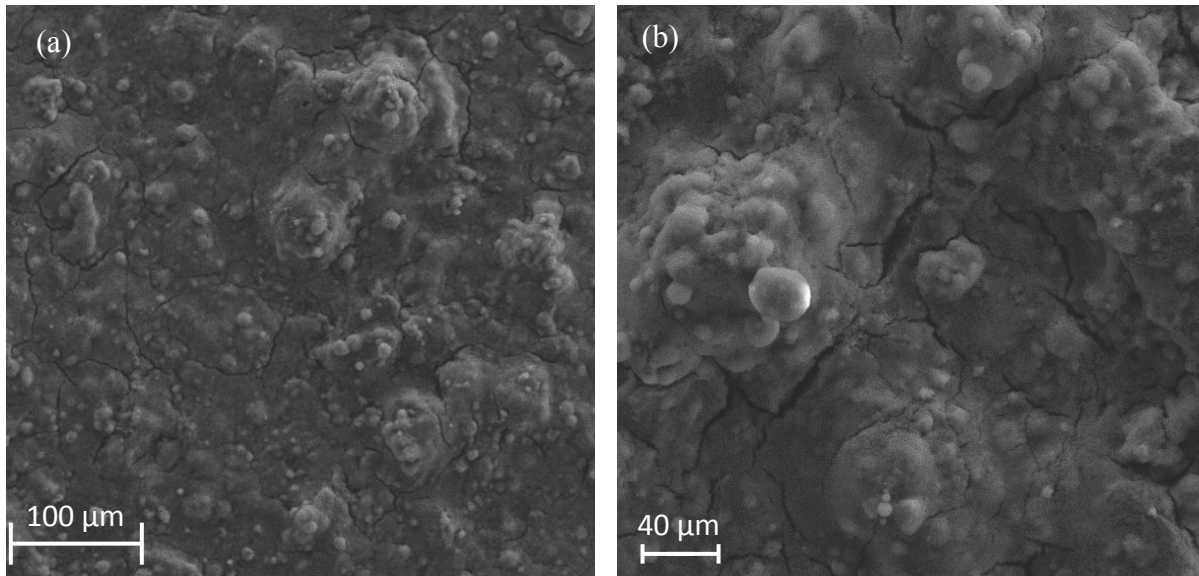


Figure 23: (a) SEM imaging of the SHS viewed at a magnification of 100 times showing the surface topography. (b) The SHS at a magnification of 250 times showing the particle size of the NW second coat.

### 3.2 Turbulent flow loop

The turbulent flow experiments were carried out in a closed loop channel used previously by Abu Rowin et al. (2017) shown in Figure 24. The setup was comprised of a rectangular cross section channel, a centrifugal pump, a laser, a camera, optical lenses, and a flow control system. The channel was at a height of 1.5 m above the pump and had inlet and outlet chambers. A centrifugal pump drove the flow and was controlled with a variable frequency driver connected to LabView. A PID controller monitored and automatically altered the voltage supplied to keep the pump impeller speed and the flowrate of the channel constant. The laser and camera timing were controlled with Davis 7.2.

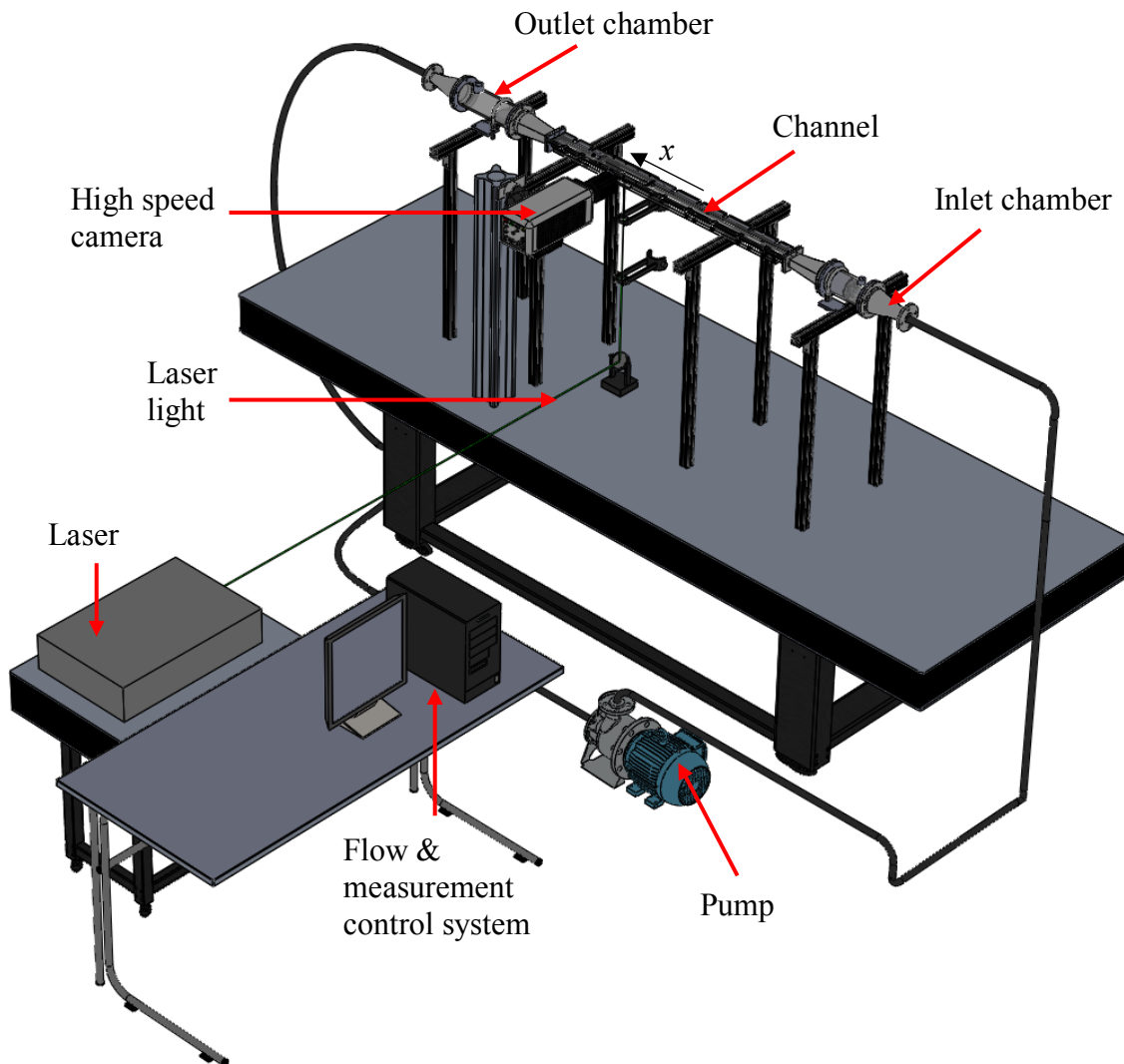


Figure 24: An illustration of the turbulent channel closed loop system used for testing SHSs.

### 3.2.1 Turbulent channel

Testing of the surfaces was done in the channel that features a rectangular cross-section ( $W \times H$ ) of  $40 \times 6 \text{ mm}^2$ , and a channel length of 1200 mm ( $200H$ ) shown in Figure 25 and Figure 26. The placement of the surfaces was at a distance of 720 mm ( $120H$ ) from the entrance ensuring fully developed flow in the region of interest. The channel has an aspect ratio and a hydraulic diameter of 6.7, and 10.4 mm respectively. The top and bottom of the channel are made from acrylic while the sides are made from glass for better optical properties. The smooth and SHS were held in the channel with a replaceable acrylic module, shown in Figure 25, that was tightened over an o-ring seal. The module can hold surfaces  $234 \text{ mm} \times 36 \text{ mm}$  in the streamwise and spanwise directions, respectively. Three pressure ports surround the module to measure the relative and absolute pressure inside the channel. The relative ports are 265 mm apart and the absolute port was located 45 mm after the surface. Upstream of the channel there was a chamber that contains a release port, a honeycomb, and fine mesh before a contraction (22:1) to the channel which can be seen in Figure 27. The release port connects to a line to de-air the loop while the honeycomb and fine grid mesh remove any large eddies caused by the pump. Downstream of the channel, another port for de-airing exists in a chamber connected to the return line to the pump.

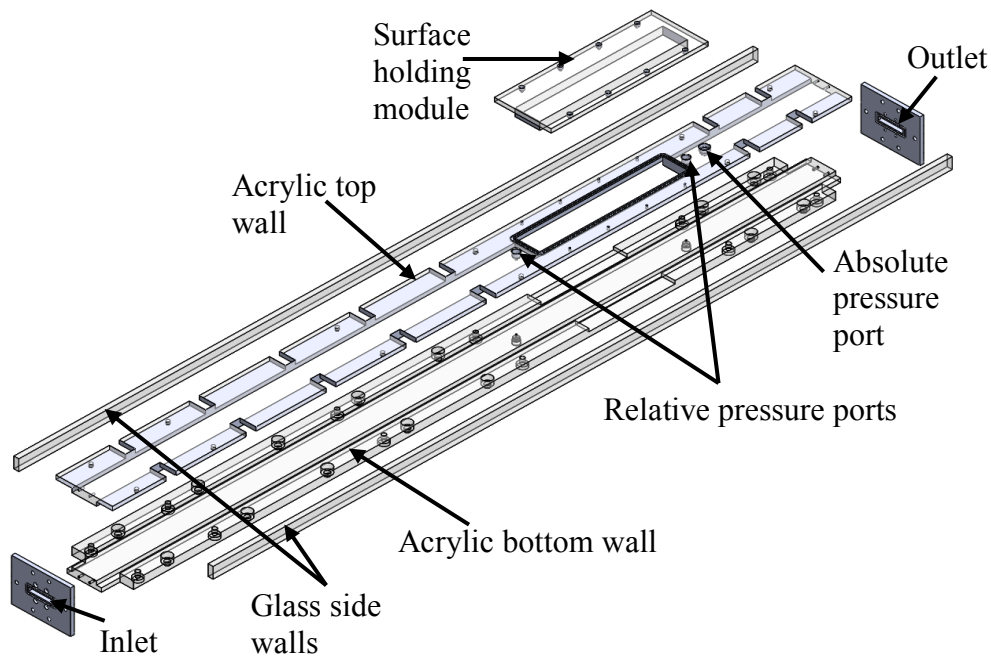


Figure 25: An exploded view of the channel portion from the closed-loop turbulent setup.

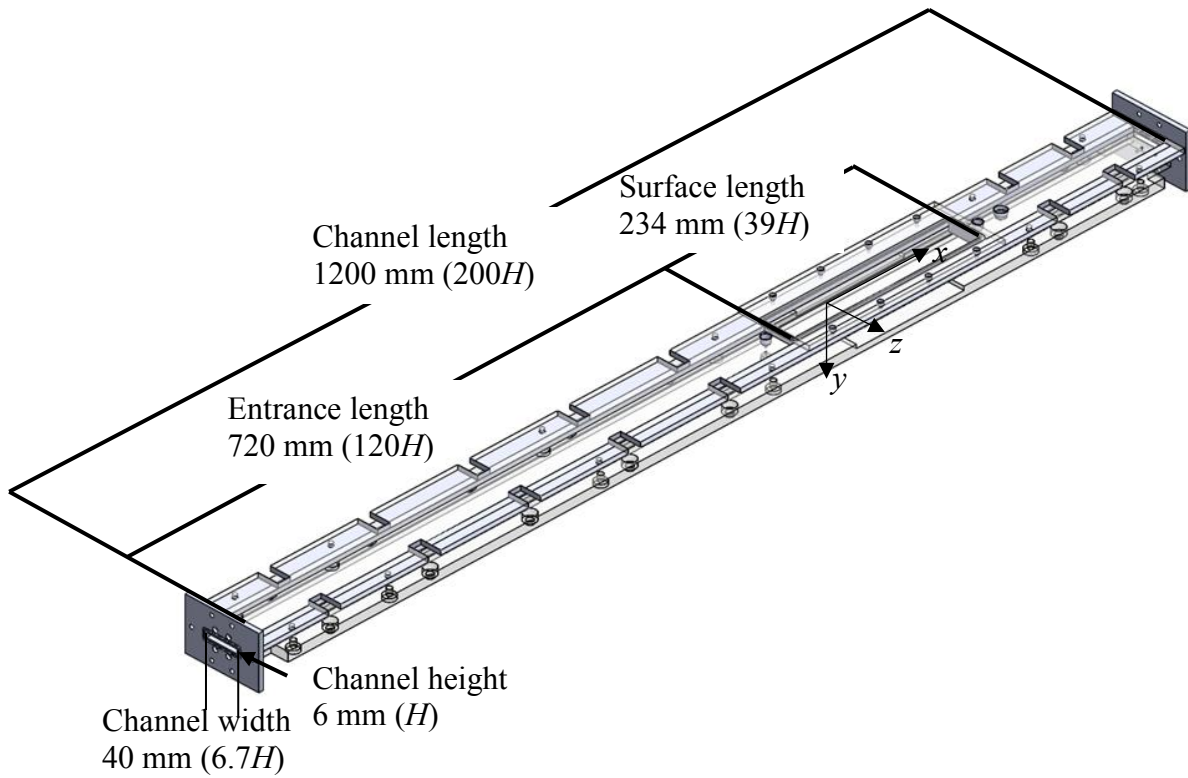


Figure 26: Dimensioned illustration of the channel portion from the closed-loop turbulent setup.

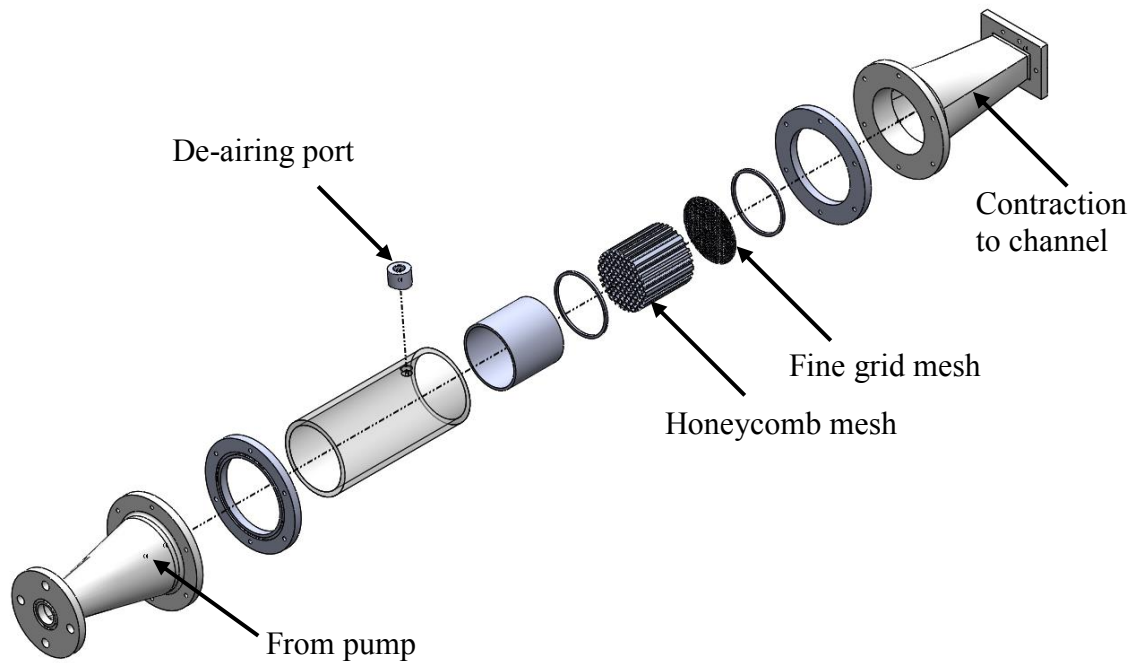


Figure 27: An exploded view of the upstream chamber used to remove large eddies.

### 3.2.2 Particle tracking velocimetry

Characterization of the turbulent flow over the surfaces was carried out with a planar PTV setup. A Phantom V611 high-speed camera collected 2000 images at a frequency of 10 kHz, every second for six cycles totaling 12,000 images over the span of five seconds. The Phantom has a sensor size of  $1280 \times 800$  pixels<sup>2</sup> ( $25.6 \times 16.0$  mm<sup>2</sup>) with pixel dimensions of  $20 \times 20$   $\mu\text{m}^2$ . The camera was fitted with a 60 mm Nikkor lens (AF Micro-Nikkor) connected to an 80 mm extension tube (Figure 28). The measurement setup had a magnification of 2.27 with a digital resolution of  $8.8\mu\text{m}/\text{pix}$  at an aperture setting of  $f/11$ . The field of view was  $6.27$  mm  $\times$   $4.79$  mm ( $712$  pix  $\times$   $544$  pix,  $504^+ \times 383^+$ ) in the  $y$  and  $x$  direction respectively with a DOF of  $0.05$  mm (I.T.Young et al. 1993). The wall unit over the smooth surface was  $12.44$   $\mu\text{m}$ . Cropping the images from the original sensor size was done to reduce the size of the image files as the field of view in the  $y$  direction was larger than the 6 mm channel height. The Phantom had a bit depth of 12 bit, a well depth of  $23,000e^-$  with a readout noise of  $29e^-$ .

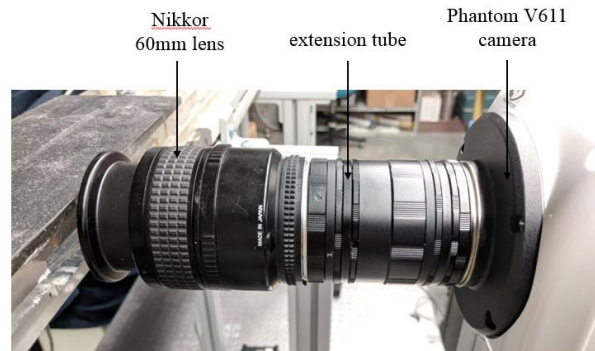


Figure 28: A picture of the high-speed camera and optical attachments.

To illuminate the region of interest a dual-head Nd:YLF laser (DM20-527, Photonics Industries) was used in conjunction with mirrors and collimating optics to redirect and expand the laser beam light into a laser sheet directed upward through the bottom of the channel. Specifications for the laser can be found in Table 1. The laser operated with a laser pulse separation,  $\Delta t = 1$  ms, a pulse energy of 20 mJ, and a pulse duration of 20 ns. The laser pulse separation allows for a maximum particle displacement of 18 pix between frames at the center of the channel and a 2 – 3 pixel displacement near the wall. The initial beam had a nominal diameter of 5.0 mm and a wavelength of 527 nm and the final laser sheet had width of 5 mm ( $x$ -direction) and thickness of 1 mm ( $z$ -



direction). Figure 29 below shows the series of mirrors used to redirected the light upwards into a spherical lens converging the beam before entering a cylindrical lens which expanded the beam into a sheet of light directed upward though the bottom of the channel.

The working fluid was deionized water seeded with VESTOSINT 2070 polyamide tracers. These tracers have an average diameter of  $5\ \mu\text{m}$  and a density of  $1.016\ \text{g/cm}^3$ . Polyamide tracers were chosen to help improve the longevity of the surfaces for testing as polyamide tracers would likely cause less damage to surfaces when collisions occur compared to tracers made of glass or metal.

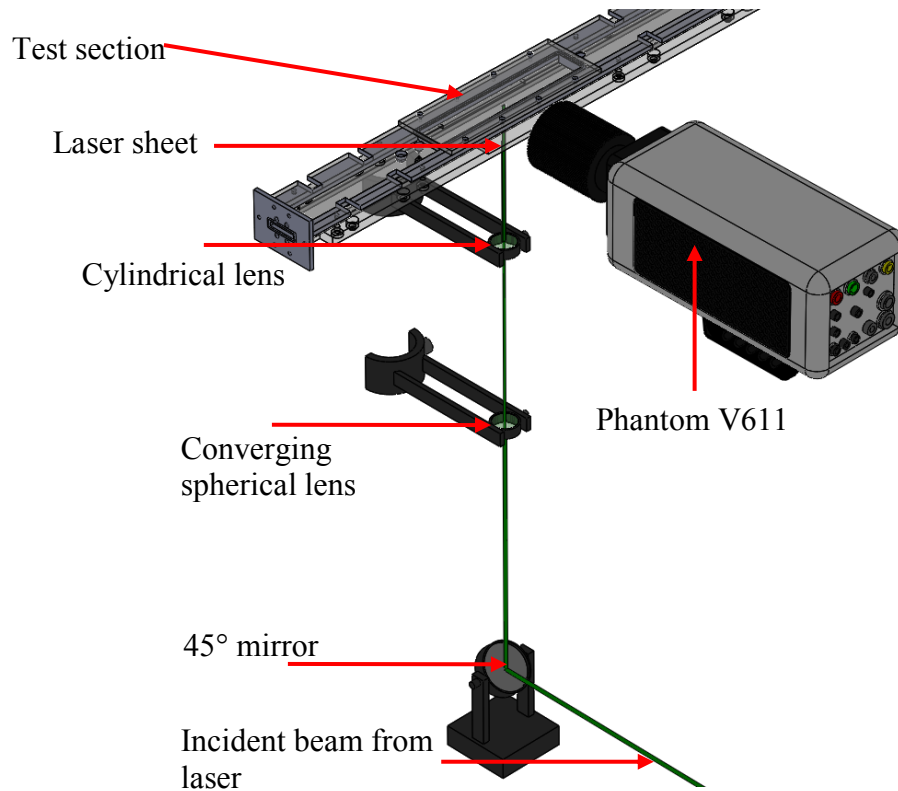


Figure 29: An illustration of the optics used to redirect and reform the laser beam into a laser sheet for turbulent flow characterization with a micro PTV setup.

Six cycles of 2,000 images were captured with a cycle frequency of 1 Hz and a frame separation of  $100\ \mu\text{s}$ . The images were processed in Davis 7.3 (LaVision GmbH) with the same noise removal method applied as the Shadow-PTV measurements. A multiplication constant of 500 and a minimum intensity for particle detection of 100 was applied for the time-resolved images due to the different lighting intensity compared to the double-frame experiments. There was a maximum displacement of 15 pixels in the streamwise direction and  $< 1$  pixel in the wall-normal direction at the center of the channel between consecutive images. The restriction of particle displacement was

$10 \pm 10$  pixels in the streamwise direction and  $0 \pm 2$  pixels in the wall normal direction. The estimated displacement was 15 pixels based on the spatial resolution (0.0088 mm/pix), bulk flowrate (1.3 m/s), and the imaging frequency (10 kHz). A side by side comparison of the original image and the image after preprocessing can be seen below in Figure 30. The PTV algorithm used a time-resolved PTV method allowing a minimum track length threshold of 10 which to removed data from particles that were lost during tracking after less than 10 consecutive images. Information about the particles pixel location in the  $x$  and  $y$  coordinates, as well as the particles identification number and track length was exported into MATLAB where the streamwise and wall normal velocity, friction velocity, and Reynolds stress terms were determined. The summary of the turbulent and laminar experimental setups can be seen in Table 1.

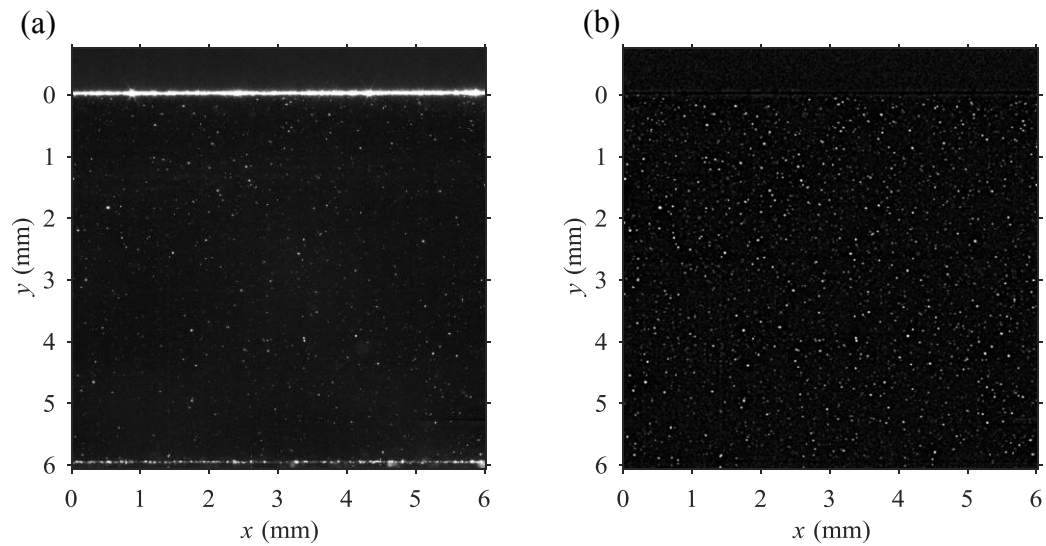


Figure 30: (a) An unprocessed image of turbulent flow over the smooth surface. (b) The image after improvement of signal to noise ratio to be used by the PTV algorithm.

Table 1: Summary of the experimental setup for the laminar and turbulent tests

Flow regime	Turbulent	Laminar	
Camera and Optics	Camera	Phantom V611 high-speed camera	FlowMaster3S
	Lens	60 mm Nikkor lens (AF Micro-Nikkor)	12 X zoom, 12 mm fine focus lens (Navitar 1-50486)
	Pixel Size	20 $\mu\text{m} \times 20 \mu\text{m}$	6.7 $\mu\text{m} \times 6.7 \mu\text{m}$
	Imaging frequency	1 s between cycles	4 image pairs per second
	Bit depth	12 bit	12 bit
	$f\#$	11	11
Laser	Laser type	Nd: YLF	Nd: YAG
	Pulse Delay	100 $\mu\text{s}$	380 $\mu\text{s}$ – 3100 $\mu\text{s}$
	Pulse energy	20 mJ	50 mJ
	Wavelength of light	527 nm	620 nm
	Illumination style: Size at channel	Light Sheet: 5 mm $\times$ 1 mm ( $x \times z$ direction)	Backlight: 165 mm in diameter
Measurement Domain	System magnification	2.27	2.77
	Depth of Field	50.8 $\mu\text{m}$	49.4 $\mu\text{m}$
	Digital resolution	8.8 $\mu\text{m}/\text{pix}$	2.42 $\mu\text{m}/\text{pix}$
	Field of view ( $y$ direction $\times$ $x$ direction)	6.27 mm $\times$ 4.76 mm 712 pix $\times$ 544 pix 504 <sup>+</sup> $\times$ 383 <sup>+</sup>	2.46 mm $\times$ 3.07 mm 1018 pix $\times$ 1271 pix
	Wall unit	12.44 $\mu\text{m}$	-
	Re	$\sim 8000$	$\sim 100 - 500$
	Mid-channel displacement	15 pix	50 pix
	Measurement Type	Time-resolved PTV	Double-frame PTV

### 3.2.1 Surface fabrication and characterization

The University of Texas fabricated four SHSs and transferred them for evaluation of their performance. The surfaces were fabricated by sandblasting a metal surface and performing an acid etch before a coating of PTFE was applied. The sandblasting parameters varied between surfaces to create surfaces with varying roughness. To classify the surfaces the surface roughness,  $R$ , was measured using a XP-300 stylus profilometer (Ambios) over three different locations on each surface. The measurement distance, stylus speed, and stylus force were held constant at 0.03 mm/s, 1.8 mm, and 5 mg, respectively. Figure 31 shows a cropped region of the roughness profile with the arithmetic roughness,  $R_a$ , and root mean square roughness,  $R_{rms}$ . The surface roughness were determined as

$$R_a = \frac{1}{L} \int_0^L |Z(x) - \bar{Z}| dx \quad 3.1$$

and

$$R_{rms} = \sqrt{\frac{1}{L} \int_0^L |Z(x) - \bar{Z}|^2 dx} \quad 3.2$$

where  $Z(x)$  is the wall-normal measurement of the surface,  $L$ , is the total profile measurement length and  $\bar{Z}$  is the mean of the measured profile (Farshad & Pesacreta 2003). Division of the roughness parameters by the respective wall unit gave the nondimensionalized roughness parameter,  $k^+$ , and the surfaces were named based on their  $k^+_{rms}$  values and hereafter will be referred to as SHS<sub>0.35</sub>, SHS<sub>0.23</sub>, SHS<sub>0.18</sub>, and SHS<sub>0.14</sub>. The  $R_{rms}$  values in  $\mu\text{m}$  were 3.9, 2.7, 2.3, and 1.9 for SHS<sub>0.35</sub>, SHS<sub>0.23</sub>, SHS<sub>0.18</sub>, and SHS<sub>0.14</sub>, respectively. The peak to trough roughness,  $R_{PT}$ , was determined as the average of the maximum peak-to-trough distance of the roughness profile within five consecutive sampling subsections (Farshad & Pesacreta 2003). The  $R_{PT}$  in  $\mu\text{m}$  was 11.6, 10.5, 8.0, and 7.5 for SHS<sub>0.35</sub>, SHS<sub>0.23</sub>, SHS<sub>0.18</sub>, and SHS<sub>0.14</sub>, respectively.

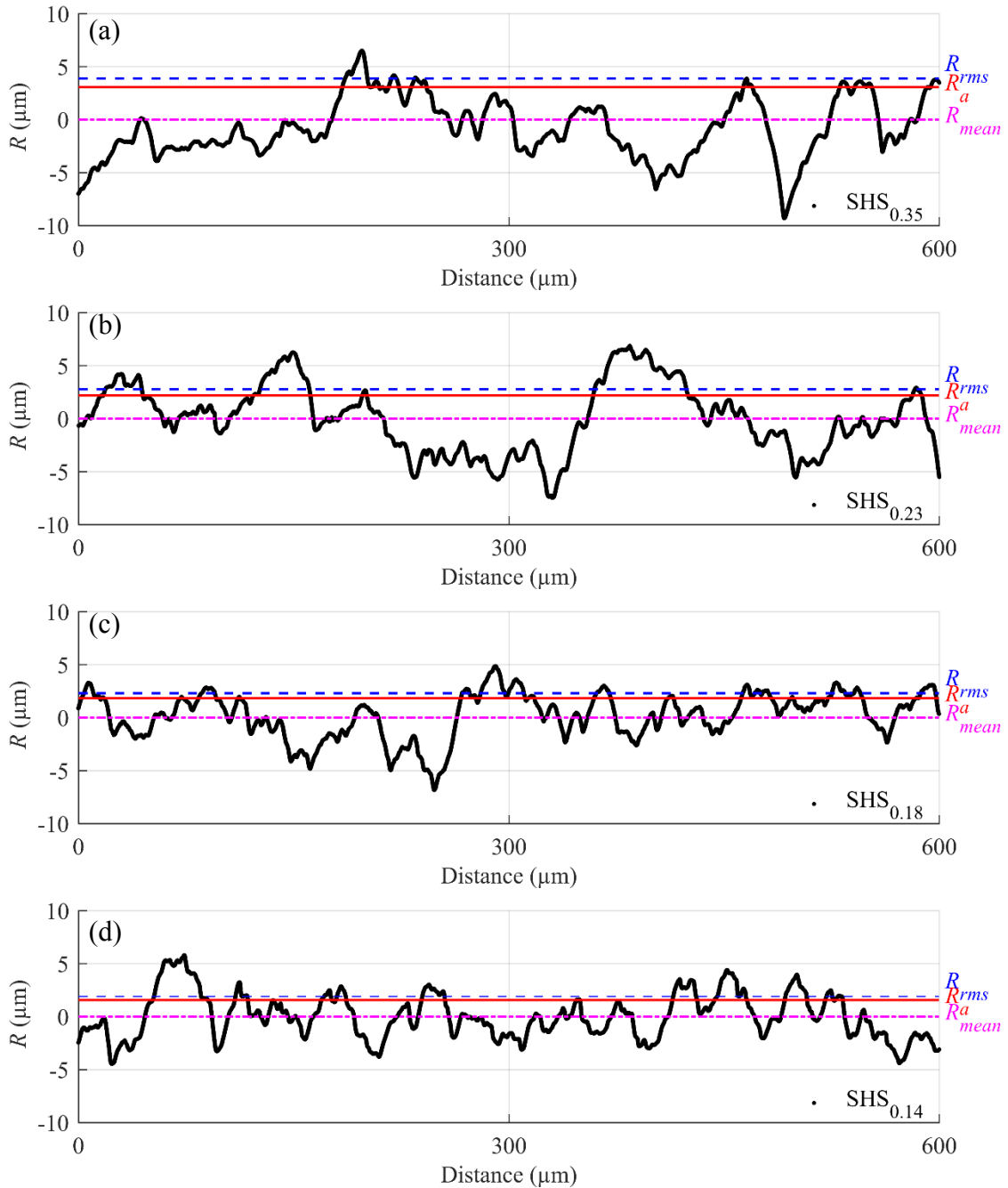


Figure 31: Profilometer measurements of the (a) SHS<sub>0.35</sub>, (b) SHS<sub>0.23</sub>, (c) SHS<sub>0.18</sub>, and (d) SHS<sub>0.14</sub> surface with their respective  $R_a$ ,  $R_{rms}$ , and  $R_{mean}$  values added for reference.

The surface topography was visualized using a SEM (Sigma 300 VP, Zeiss). A top down view of the surfaces at a magnification of 250 times are shown in Figure 32. The surfaces were not coated for the SEM images and were therefore susceptible to charge accumulation which appear as bright white spots on the image, most noticeable as the magnification increases. Each surface has a

similar pattern of voids, pits from the sandblasting process, separating roughness elements of varying heights. The roughness elements and voids, darker regions in the images, have been annotated in Figure 32a for clarity. As expected from the profilometer measurements, there was a visible trend of the roughness topography between surfaces. The SHS<sub>0.35</sub> surface had the largest roughness elements while SHS<sub>0.14</sub> had the smallest. The spacing between the voids on SHS<sub>0.35</sub> were the largest at 15  $\mu\text{m}$  to 20  $\mu\text{m}$  while the voids on SHS<sub>0.14</sub> were mostly  $< 10 \mu\text{m}$  and more closely spaced. Viewing the surfaces at a magnification of 1500, Figure 33, allowed inspection of the individual features that comprise the roughness elements. There was evidence of the pits caused by the sandblasting process but more importantly, the individual features were of similar sizes ( $< 5 \mu\text{m}$ ) across all surfaces. From the profilometer measurements and SEM images, it was conclusively determined that the only change between the surfaces was the void spacing and height of the roughness structures showing an increase of  $R_a$  related to an increase in void size and roughness height.

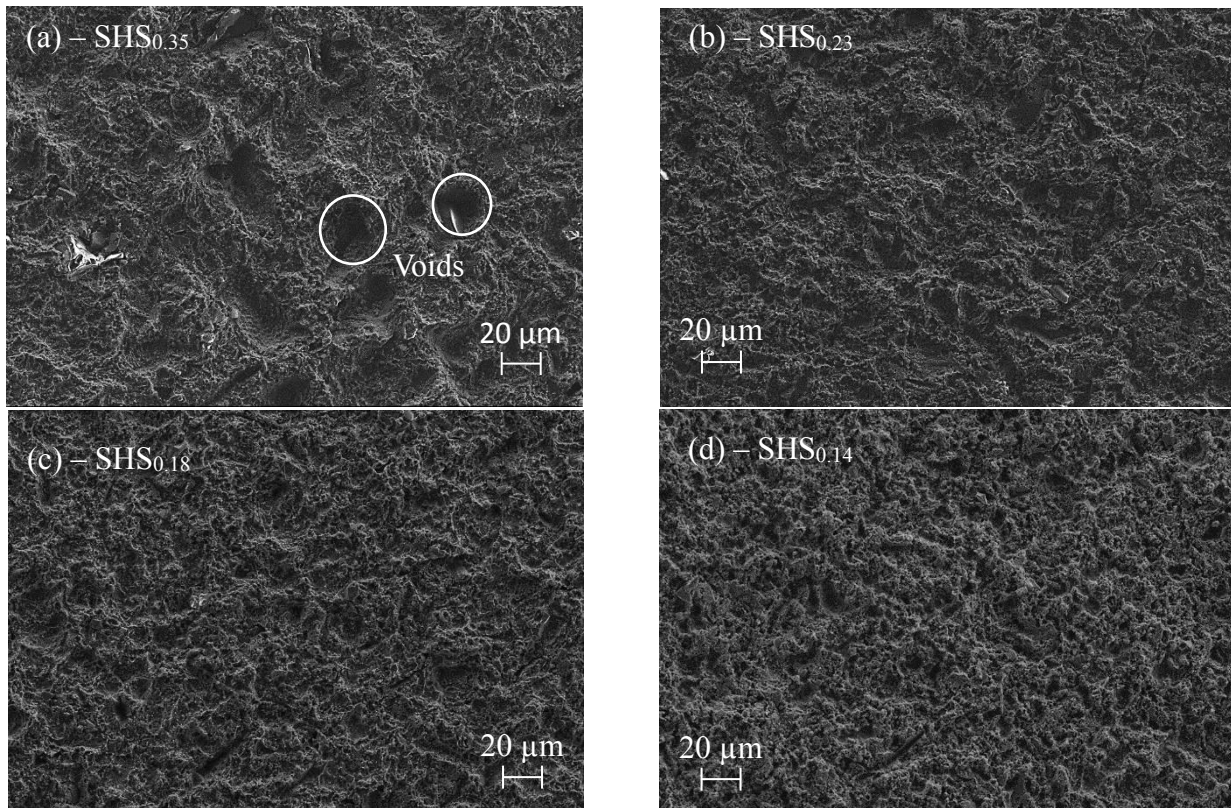


Figure 32: Top down SEM images at a magnification of 250 of (a) SHS<sub>0.35</sub>, (b) SHS<sub>0.23</sub>, (c) SHS<sub>0.18</sub>, and (d) SHS<sub>0.14</sub>.

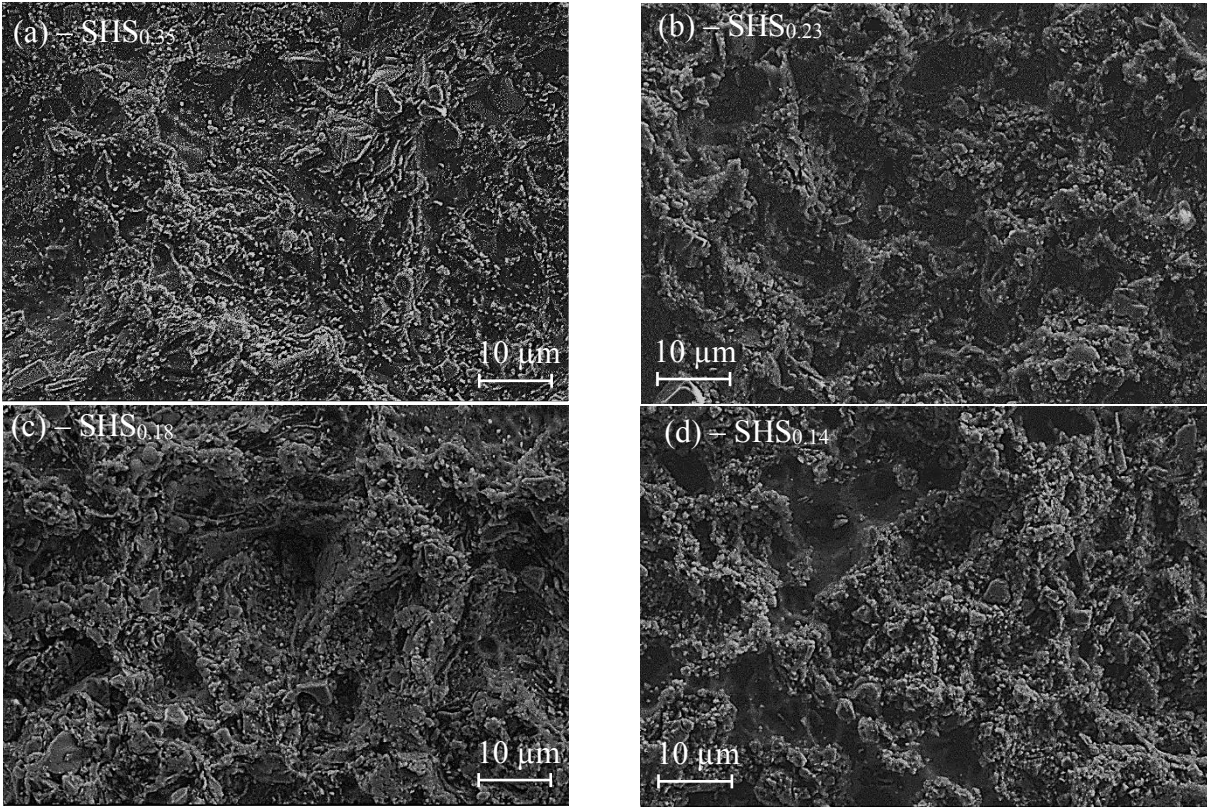


Figure 33: Top down SEM images at a magnification of 1500 of (a) SHS<sub>0.35</sub>, (b) SHS<sub>0.23</sub>, (c) SHS<sub>0.18</sub>, and (d) SHS<sub>0.14</sub>.

Each of the surfaces contact angles were determined with a drop shape analyzer (DSA-100, KRÜSS) using the sessile drop technique. A 10 $\mu$ L droplet of water was placed on the surfaces in varying locations and the average contact angle was found before and after the experiment. The contact angle before the experiments over SHS<sub>0.35</sub>, SHS<sub>0.23</sub>, SHS<sub>0.18</sub>, and SHS<sub>0.14</sub> were and 147.7°, 151.1°, 146.8°, 151.6°, respectively. Afterwards, each surface had a contact angle reduction ranging from 2° – 2.5°.

## 4 Measurement uncertainty

This chapter is composed of four subchapters; the first two discuss the detection method for the wall location with the shadow-PTV and time-resolved PTV systems, respectively. The third subchapter discusses the uncertainties in the experimental results. It provides a brief background on errors and their sources followed by the errors that were present during the experiment and the total uncertainty of the results. The final subchapter looks at the repeatability of the laminar flow conditions and the measurement system.

### 4.1 Wall location method for shadow-PTV

Identification of the wall was critical when examining flows over SHSs as it directly affects the presented slip velocity and slip length. The wall location of the smooth surface was clearly identifiable from the images, however, for the SHS there was a surface structure from the coating. Determination of the wall location was done with the average of the ensemble of images. At each  $x$  position, the largest detected location of surface topography ( $y$  position) was determined using a MATLAB code that detected the highest pixel intensity within the expected wall range. The range of the expected wall location was larger for the SHS as the surface roughness was larger when compared to the smooth surface. Detecting the longest peak locations was possible due to a reflection of light that came from the peaks, and is denoted as the Longest Roughness Structure (LRS). The shortest detected location of surface topography is denoted as the Shortest Roughness Structure (SRS) and the Average Roughness Structure (ARS) is determined as the mean of the LRS and SRS as opposed to weighted mean of the full profile (Joseph et al. 2006).

Figure 34a shows a cropped image of the near wall region for the smooth surface. Figure 34b shows the detected LRS, ARS, and SRS locations over the smooth surface. The LRS and SRS are 0.006 mm (3 pix) from the ARS. For visual clarity, the colors in Figure 34 have been inverted so that the black pixels represent the highest intensity and the white pixels represent lower intensities. Figure 35a shows the cropped image of the near wall region over the SHS which show a distinct roughness profile. Figure 35b shows the detected LRS, SRS and ARS as well as the reconstructed wall location. Over the SHS, the LRS and SRS are 0.027 mm (12 pix) from the ARS.



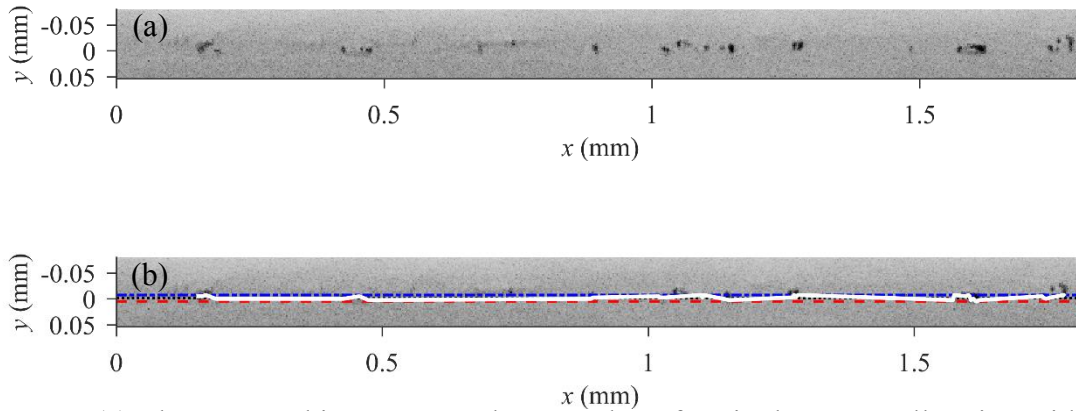


Figure 34: (a) The averaged images over the smooth surface in the near wall region with colour inversion. (b) The average of the images of the smooth surface in the near wall region with the roughness structure detection applied. The SRS, ARS, and LRS is denoted by the dash-dot (blue) line, dotted (black) line, and dashed (red) line, respectively. The surface reconstruction is shown as the solid (white) line.

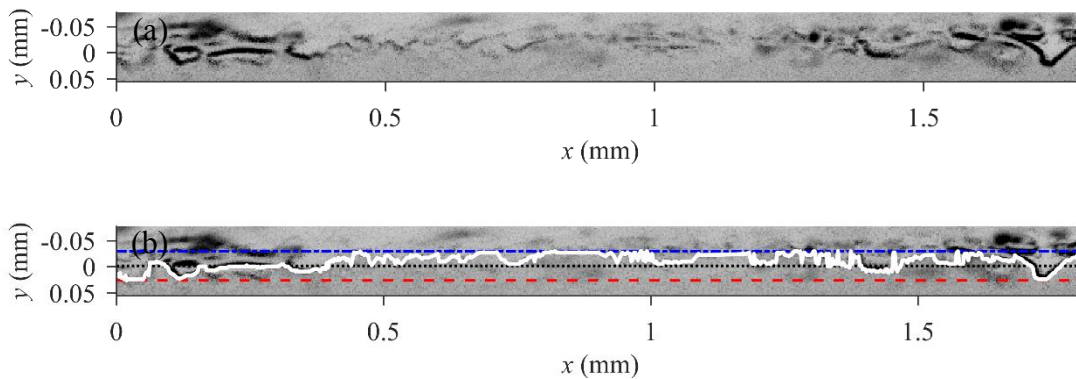


Figure 35: (a) The averaged images over the NW coated surface in the near wall region with colour inversion. (b) The average of the images of the NW coated surface in the near wall region with the roughness structure detection applied. The SRS, ARS, and LRS is denoted by the dash-dot (blue) line, dotted (black) line, and dashed (red) line. The surface reconstruction is shown as the solid (white) line.

## 4.2 Wall location method for time-resolved PTV

For the turbulent flow experiments, the wall location was determined through an intensity detection algorithm developed using MATLAB. This was possible because the surface reflected a portion of the laser light. Figure 36a shows the average of the images from the SHS<sub>0.23</sub> test after removal of noise in the images as mentioned in Chapter 3.2.2. There was a thin bright line, which was the surface as well as some reflection from near the surface. The intensity profile of the image

was determined with the maximum intensity indicating the location of the surface as shown in Figure 36b. The uncertainty in the location of the wall is a function of the diameter of the beam where the beam diameter,  $d_b$ , is defined as  $d_b = I_m/e^2$ , where  $I_m$  is the maximum intensity of the beam. The wall location uncertainty was determined to be  $\pm 0.03$  mm ( $\pm 1.5$  pix,  $\pm 1.10y^+$ ).

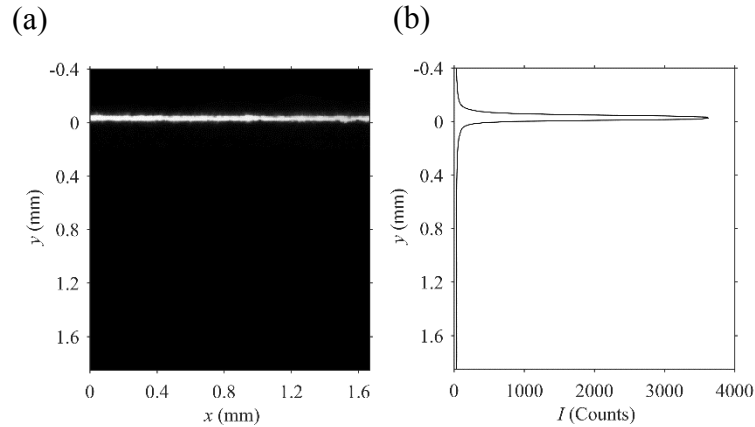


Figure 36: (a) Cropped image of the average of images over SHS<sub>0.23</sub>. (b) Intensity profile of the average of the images over SHS<sub>0.23</sub>.

### 4.3 Measurement uncertainties

The uncertainties associated with the reported values for the laminar flow are of importance due to the magnitude of the reported values. Most of this discussion is adapted from ITTC (2008) and Lazar et al. (2010). The sample analysis that follows was for the Shadow-PTV setup at a  $Re_b = 250$ .

Measurement errors typically lie within two categories, biased errors (systematic) and precision errors (random). The biased errors are repeatable, consistent errors based on the experimental system and the measurement equipment. Systematic errors do not vary when the same measurement system observes the same measurand. The first major sources of systematic errors arise from calibration. Calibration errors are not avoidable and are present in any experiment. Visualization techniques that use tracer particles require a sensor that converts electrons to voltages. The aging of equipment can change the linearity of an input to the output over time and is difficult to detect. The second source of systematic error is due to a change of the measurand due to the measurement equipment. This typically occurs when using an intrusive measurement system. PTV is a nonintrusive technique and the seeding particle concentration was kept low enough to prevent

the working fluid from behaving as a two-phase flow. The last source of systematic error arise from variables other than the measurand affecting the measuring system. For all experiments, the water temperature was measured before each experiment and afterwards to verify the water properties used to characterize the flow stayed constant between each test. Additionally, the tests were ran the same day to prevent other factors such as water acidity and O<sub>2</sub> content, whose effects on the performance of SHSs are not known, from varying between trials. Random errors come from a lack of repeatability in the measurement output. For flow visualization techniques of laminar flow, this is seen as by a scatter of measured velocities at the same wall-normal location. The random error can be minimized through methods such as averaging and other statistical methods to eliminate data points that lie outside of a certain expected interval.

The total uncertainty of a parameter can be evaluated using propagation of uncertainty where a function,  $f(x_1, x_2, x_3)$  can have its uncertainty determined based on the uncertainties  $\epsilon_{x1}$ ,  $\epsilon_{x2}$ ,  $\epsilon_{x3}$  shown in equation 4.1.

$$\epsilon_f = \sqrt{\left(\epsilon_{x_1} \frac{\partial f}{\partial x_1}\right)^2 + \left(\epsilon_{x_2} \frac{\partial f}{\partial x_2}\right)^2 + \left(\epsilon_{x_3} \frac{\partial f}{\partial x_3}\right)^2} \quad 4.1$$

An important factor when considering the measurement system and the desired measurand is the sensitivity,  $c_i = \partial f / \partial x_i$ , of the measuring system. For PTV measurements, the velocity of a tracer particle is considered as

$$u = \alpha \left( \frac{\Delta X}{\Delta t} \right) + \delta u \quad 4.2$$

where  $\alpha$  is the magnification factor in mm/pix,  $\Delta X$  is the change in the tracer particle position in mm,  $\Delta t$  is the time step of the two images in seconds, and  $\delta u$  is an uncertainty factor in the flow speed in mm/s. The total uncertainty in the particle velocity,  $\epsilon_u$ , particle position  $\epsilon_x$ , and the time increment,  $\epsilon_t$ , was determined separately based on their own error sources and the use of 4.1.

#### 4.3.1 Uncertainties in particle velocity

The uncertainty in the particles velocity depended on the calibration target, optical system, experimental conditions, illumination, image detection, data processing, time interval, and particle

trajectory. The uncertainties are directly related to the experimental setup and PTV measurement parameters, shown in Table 2.

Table 2: A summary of the laminar experimental setup and Shadow-PTV measurement parameters used for uncertainty analysis.

Parameter	Value	Units
Measurement area	$2.5 \times 2$	mm $\times$ mm
Uniform flow speed	0.16	m/s
<b><u>Calibration</u></b>		
Physical distance to reference point ( $l_r$ )	0.5	mm
Image distance to reference image ( $L_r$ )	207	pix
Diameter of reference point	100	$\mu\text{m}$
Magnification factor	2.77	
Spatial resolution ( $\alpha$ )	0.0024	mm/pix
<b><u>Flow visualization</u></b>		
Average diameter ( $d_p$ )	5	$\mu\text{m}$
Standard deviation of diameter ( $s_p$ )	0.5	$\mu\text{m}$
Laser power	50	mJ
Time interval ( $\Delta t$ )	0.7	ms
Particle displacement at wall	3	pix
<b><u>Image detection</u></b>		
Sensor size	$1280 \times 1024$	pix $\times$ pix
Sampling frequency	4	Hz
Pixel size	$6.7 \times 6.7$	$\mu\text{m} \times \mu\text{m}$
<b><u>Optical system</u></b>		
Working distance ( $l_t$ )	105	mm
Focal length, $f$	12	mm
$f\#$	11	
<b><u>Data processing</u></b>		
Pixel unit analysis	Shadow-PTV	

### Calibration

Calibration allowed the conversion from pixel space to physical space and was completed with the use of a calibration target. The target was placed at the location of the viewing plane and the

distance between the reference points in physical space,  $l_r$ , was converted to the distance seen in the pixel space,  $L_r$ , to determine the magnification factor,  $\alpha$ . The magnification factor can be determined with the equation

$$\alpha = \frac{l_r \cos(\theta)}{L_r} \quad 2.1$$

where the perspective angle,  $\theta$ , accounts for angle misalignment between the target plane and the viewing plane.

The uncertainties from calibration are based on the calibration target used. Table 3 below shows the error source, the uncertainty and the sensitivity to the source for calibration of the PTV system. In the PTV setup, the calibration target (LaVision) had a reference point separation of 500  $\mu\text{m}$  with a reference point diameter of 100  $\mu\text{m}$ . The uncertainty of the distance between reference points depended on the number of reference points used. Calibrating with a single reference point by using the left and right edge of a reference point gave an uncertainty of 0.7 pix. The calibration of the PTV system used two reference points increasing the uncertainty to 0.98 pix. The uncertainty of the physical size of the reference point was not listed and assumed to be at most 5% of the point diameter.

The optical system produced uncertainties due to distortional effects attributed to lens aberrations. These effects were assumed to be less than 0.5% (0.2 px) of the total point diameter. Errors associated with the CCD are typically small and negligible compared to the magnitude of the other calibration uncertainties. The position of the reference target compared to the viewing plane could be different and therefore affect the magnification factor and accuracy. Using the pinhole camera model assumption,  $L_r = l_r \times f / l_t$  where  $l_t$  is the distance from the target and  $f$  is the focal length of the system in pixels respectively. The sensitivity coefficient with respect to the reference target position can be expressed as

$$\frac{\partial \alpha}{\partial l_t} = \frac{1}{f} = -\frac{l_r}{L_r l_t} \quad 2.2$$

Lastly, the potential difference between the reference target plane and the viewing plane was, at most, 0.035 rad ( $2^\circ$ ).

Table 3: Calibration uncertainty sources and magnitudes for the PTV system.

Parameter	Category	Error Source	$\varepsilon(x_i)$	$c_i$	$c_i\varepsilon(x_i)$
$\alpha$	Calibration Target	Reference image	2.07 pix	1.17E-5 mm/pix <sup>2</sup>	2.42E-5
		Physical distance	0.0050 mm	4.83E-3 1/pix	2.42E-5
	Optical System	Image distortion by lens	1.04 pix	-1.17E-5 mm/pix <sup>2</sup>	-1.21E-5
		Image distortion by CCD	0.0056 pix	3.80E-4 mm/pix <sup>2</sup>	2.13E-6
		Reference target position	0.50 mm	-2.30E-5 1/pix	-1.15E-5
	Experimental condition	Parallel reference board	0.035 rad	-8.45E-5 mm/pix	-2.96E-6

Combined Uncertainty (nm/pix) 38

### Displacement of particle image

The uncertainties associated with the change in the particles position between frames are attributed to the illumination source, image detection, and data processing. The error in the displacement of the particle image is shown in Table 4 along with the error source, uncertainty and the sensitivity to the source. PTV systems use a laser whose spatial and temporal fluctuations directly affect the detection of the particles image position. For the laminar flow condition experiments, the laser power fluctuations are not considered in the uncertainty of the particle displacement as the tracers blocked the light instead of the reflecting. Typically, the maximum uncertainty associated with the laser power fluctuation is on the order of the particle diameter but can be as low as 1/10<sup>th</sup> of the

particle diameter. The image detection uncertainties came from the distortion caused by the optical system, distortion caused by the CCD, and the uncertainty in the viewing angle. The uncertainty caused by the distortion in the optical system have been accounted for during calibration. The CCD distortion error source was the same as the error source in the calibration and therefore has the same uncertainty value. The perpendicularity of the camera to the test region was measured through digital levels and angle finders. To remain conservative, the uncertainty from these measurements were at most 2°. The uncertainties in data processing must be directly determined as there are detection limitation for each PTV algorithm. Okamoto et al. (2000) and Nishio & Murata (2003) showed that by using an artificial image the uncertainty of the PTV algorithm can be directly determined. The sub-pixel analysis of tracing a particle depend on factors such as the particle diameter, the signal to noise ratio, and the particle concentration. Again, the systematic error of the sub-pixel analysis can be determined through means of a standard image (Okamoto et al. 2000) and was assumed to be 0.03 pixels for the PTV algorithm.

Table 4: Particle displacement uncertainty sources and magnitudes for the PTV system.

Parameter	Category	Error Source	$\varepsilon(x_i)$	$c_i$	$c_i\varepsilon(x_i)$
$\Delta X$	Image detection	Image distortion by CCD	0.0056 pix	1	0.0056
		Normal view angle	0.035 rad	0.0024 mm/pix	8.00E-5
	Data Processing	Sub-pixel analysis	0.03 pix	1	0.03
Combined Uncertainty (pix)					0.03

### Time interval and flow tracking

The uncertainty in the delay generator of the laser and the pulse timing both affect the uncertainty in  $\Delta t$  while the uncertainty of the particle tracking fluid motion depended on the particle density and size. The uncertainty of the time interval and in tracking by the tracers are shown in Table 5. The jitter of the Solo-III reported in the user manual was 1 ns and the pulse timing accuracy was assumed to be 5 ns. The gravitationally induced velocity of the particle was less than 0.01% of the flow velocity (Equation 2.64).

Table 5: Time interval and tracking uncertainty sources and magnitudes for the PTV system.

Parameter	Category	Error Source	$\varepsilon(x_i)$	$c_i$	$c_i\varepsilon(x_i)$
$\Delta t$	Acquisition	Delay generator	2.00E-9 s	1	2.00E-9
		Pulse time	5.00E-9 s	1	5.00E-9
Combined Uncertainty (s)					5.39E-9
$\delta\varepsilon$	Experiment	Particle trajectory	0.0050 mm/s	1	5.00E-3
		Combined Uncertainty (mm/s)			

Combining the four uncertainty parameters,  $\alpha$ ,  $\Delta X$ ,  $\Delta t$ , and  $\delta\varepsilon$  the total uncertainty in  $\varepsilon_u$  can be determined. Table 6 shows the four parameters and the sensitivity of  $\varepsilon_u$  to them. The largest contributing factor to  $\varepsilon_u$  was the magnification factor, which accounted for 66% of the uncertainty. Although the uncertainty in the magnification was not the largest of the four parameters, it was seen that  $\varepsilon_u$  was the most sensitive to the magnification parameter. The uncertainty in the magnification factor arose primarily from the uncertainty in the reference target diameter. Obtaining a more precise calibration target, or determining the true uncertainty of the target points are the first things that should be taken into consideration when trying to minimize the experimental uncertainty.

Table 6: Total velocity uncertainty and the major error sources for the Shadow-PTV setup.

Parameter	Error Source	$\varepsilon(x_i)$	$c_i$	$c_i\varepsilon(x_i)$
$\alpha$	Magnification Factor	3.82E-5 mm/pix	4826 pix/s	0.1636
$\Delta X$	Image Displacement	0.03 pix	6.35 mm/(s×pix)	0.20
$\Delta t$	Image Interval	5.39E-09 s	-0.022 mm/s <sup>2</sup>	1.52E-10
$\delta\varepsilon$	Experiment	0.0050 mm/s	1	0.0050
Combined Uncertainty, $\varepsilon_u$ , (mm/s)				0.27



### 4.3.2 Uncertainty in particle position and measurement time

For PIV methods, the measurement position of a tracer particle is affected by the uniformity of the tracers in a correlation window as well as the center of the correlation window. PTV methods only rely on the identification of the center of the tracer particle. An uncertainty of 0.1 pix was used as uncertainty in detection of the center location for the tracer (I.T.Young et al. 1993). The conversion from image space to physical space also played a role in the measurement position with the uncertainty in  $\alpha$  determined above. The sensitivity factor towards  $\alpha$  was taken as the particle diameter in pixels. The uncertainty in measurement time is affected by the same factors as the time interval; the delay generator, and the pulse time uncertainties. Table 7 highlights the uncertainty sources and sensitivity for the measurement position and measurement time. The spatial resolution played the largest role (96% contribution) to the uncertainty in the particle position. The total uncertainty in the measurement time was orders of magnitude lower than the experimental time intervals as was deemed not important to mitigate further.

Table 7: Position and time uncertainty sources and magnitudes for the PTV system.

Parameter	Category	Error Source	$u(x_i)$	$C_i$	$C_i u(x_i)$
x	Acquisition	Particle Center	0.1 pix	0.0024 mm/pix	2.42E-4
		Magnification	3.82E-5 mm/pix	2 pix	7.64E-5
Combined Uncertainty, $\epsilon_x$ , (mm)					2.52E-4
t	Acquisition	Delay generator	2.00E-9 s	1	2.00E-9
		Pulse time	5.00E-9 s	1	5.00E-9
Combined Uncertainty, $\epsilon_t$ , (s)					5.39E-9

The largest contributing factor the total uncertainty was from determining the tracer velocity. More specifically, from the magnification of the system due to uncertainties in the calibration target. Not only did the uncertainty of the target affect the magnification, but the magnification was the leading contributor to the uncertainty in the particle displacement between frames. The target uncertainty contributed to 87% of the total uncertainty in velocity. The sensitivity to the magnification also played a large role in the uncertainty due to the small displacement of the tracers near the wall and time interval between image pairs. Table 8 shows the total uncertainty in the velocity, position and

time at the wall location for the PTV measurement system at each  $Re_b$ . The uncertainty in velocity decreases as the  $Re_b$  decreases due to the increase in  $\Delta t$  which lowers the sensitivity to the magnification.

Table 8: Total experimental uncertainty of the Shadow-PTV measurement system.

$Re_b$	$\varepsilon_u$ (mm/s)	$\varepsilon_x$ (mm)	$\varepsilon_t$ (s)
450	2		
350	0.8		
250	0.3	3E-4	6E-9
150	0.2		
50	0.1		

The uncertainties  $\varepsilon_u$ , and  $\varepsilon_x$  in the turbulent channel was determined using the same approach as presented above. Since the imaging frequency was the same for all turbulent flow experiments, there was only one uncertainty value for all tests. The uncertainties  $\varepsilon_u$ , and  $\varepsilon_x$  was determined to be 6 mm/s and 0.9  $\mu\text{m}$  respectively. The uncertainty in  $\alpha$  and  $\Delta X$  each contributed to 50% of the velocity uncertainty. The uncertainty in  $\alpha$  came mostly from the uncertainty in the calibration target because the micro-PTV setup used the same calibration target as the shadow-PTV setup. The sensitivity to the  $\Delta X$  parameter was higher in the micro-PTV setup due to the lower  $\Delta t$  of 100  $\mu\text{s}$ . The uncertainty in the particle position was mostly affected by the spatial resolution decrease.

#### 4.4 Repeatability of the laminar flow loop

Verification of the repeatability of the measurement system was done by taking two data sets over the smooth surface at the same  $Re_b$ . The surface was removed from the module between tests simulating the changing of surfaces when switching to the SHS. These tests were done at  $Re_b$  of 250. Figure 37 below shows the mean streamwise velocity profile,  $u$ , as a function of the wall-normal position normalized by the channel height,  $h = 2$  mm. The mean velocity profile was obtained using a sliding average with a bin size of 0.01 mm (5 pix).  $y = 0$  mm represents the top of the channel where the test surface was located. From  $y/h = 0$  to  $y/h = 0.15$ , the results overlap and afterwards there was an increasing deviation up to 0.05 m/s at the midstream.

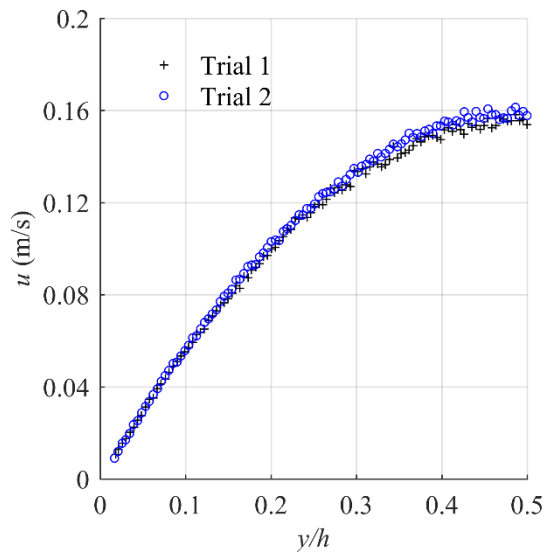


Figure 37: Mean streamwise velocity profiles at  $Re_b = 250$  over a smooth surface for repeatability verification.

The agreement of the data through multiple tests in the near wall region was more important because data in the near wall region will be used to determine slip lengths and slip velocities. From these results, the repeatability of the motor and syringe was able to consistently operate at desired  $Re_b$ .

# 5 Laminar channel flow over a randomly textured superhydrophobic surface

## 5.1 Introduction

The primary goal of the research was to investigate the critical pressure at which the performance of NeverWet (NW) (Rustoleum) decreases. The secondary goal of this research was to study the effect of bulk Reynolds number,  $Re_b$ , on the slip velocity,  $u_s$ , and  $l_s$  in the laminar regime. The last goal of the research was to develop a small scale flow loop for future surfaces to be tested on before being scaled up to larger sizes. Due to the difficulty of manufacturing large scale surfaces, testing at a small scale can be performed to determine optimal designs before upscaling for other applications. The laminar channel provided an inexpensive way to test various patterned SHS designs at this scale. Commercial spray coating NW has been studied due to its inexpensive cost, its scalability, its repeatable fabrication process, and its short fabrication time requirements. The NW surfaces have previously been studied under the turbulent flow condition (Aljallis et al. 2014; Zhang et al. 2015; Hokmabad 2015; Abu Rowin et al. 2017). It has been shown that pressures above atmospheric have an effect on performance characteristics of SHSs (Gose et al. 2018). The increase in pressure causes compression of the air layer toward the surface causing an exposure of surface roughness to the fluid that would not be seen at atmospheric pressure (Lei et al. 2010; Ling et al. 2016; Ling et al. 2017). For this reason, the study used pressures below atmospheric in an effort to avoid the air layer compression. The flow was characterized with a shadow particle tracking velocimetry (shadow-PTV) system that obtained the velocity profile at  $Re_b = 50$  to  $Re_b = 450$ , determined based on the average velocity, corresponding to channel pressures below atmospheric, hereafter denoted  $P_c$ , between 1373 - 1435 Pa.

## 5.2 Results and discussion

At each  $Re$ , measurements from the surface to the half channel height were taken to determine the velocity profile. Figure 38 shows the mean streamwise velocity profile versus the normalized wall normal position for each of the tested  $Re_b$  over the smooth surface. The data points shown are obtained by using a sliding average with a bin size of 0.01 mm (5 pix). The solid lines shown are

second order empirical equations derived from the Navier-Stokes equations for channel flow with no-slip boundary conditions on the bottom, side, and top walls fit on the data with the least squares model. The least square fit at each  $Re_b$  was done by varying  $\partial P/\partial x$  which changes the magnitude of the mean velocity. For all of the tests except  $Re_b = 400$  the mean velocity profile has a smooth profile that matches well with the empirical equation. At  $Re_b = 400$ , there appears to be some noise, most noticeable at the mid channel section, which results in a small finite velocity at the wall. This was believed to be due to a larger spread in the data at the higher  $Re_b$ . More images would provide a better representation of the mean velocity by reducing the effect of outlying velocity values. Using a larger bin size over the data nearer to the center of the channel would reduce the noise; however, the larger bin size would take away from the resolution of the region of interest, near the wall. There also exists non-zero values for the slip velocities,  $-1.03 \mu\text{m/s}$  ( $-0.43 \text{ pix/s}$ ) to  $1.6 \text{ mm/s}$  ( $726.70 \text{ pix/s}$ ), and slip lengths, of  $0.0011 \text{ mm}$  ( $0.50 \text{ pix}$ ) to  $0.003 \text{ mm}$  ( $1.24 \text{ pix}$ ). However, both the non-zero values of slip velocity and slip length over the smooth surface lie within the determined experimental uncertainty of  $0.3 - 2 \text{ mm/s}$  and  $0.4 \mu\text{m}$  respectively. The figures presented hereafter of the velocity profile do not have error bars for visual clarity. The remaining figures or data points that do not have error bars associated with them are because the error bars are not larger than the point size.

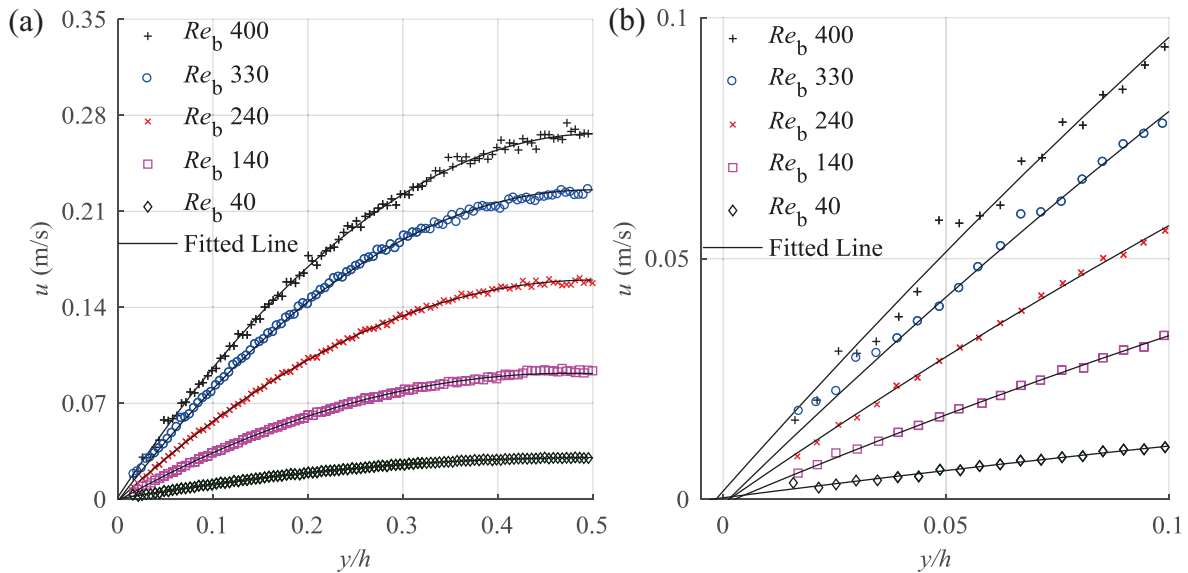


Figure 38: (a) Mean velocity profiles over a smooth surface for half channel at  $Re_b = 40, 140, 240, 330,$  and  $400$ . (b) Mean velocity profiles over a smooth surface in the near wall region ( $y < 0.2 \text{ mm}$ ) at  $Re_b = 40, 140, 240, 330,$  and  $400$ .

Figure 39a shows the mean velocity profiles vs the wall-normal position normalized by the channel height for the SHS at all  $Re_b$ . Again, the mean velocity profile was obtained with a sliding average using the aforementioned bin size. The solid lines shown are fit using the least square method with a second order empirical equation derived for channel flow. The equation has no-slip boundary conditions on the bottom, and side walls and a slip boundary condition over the top wall. In the middle of the channel there was more variation in the data compared to values below  $y/h = 0.2$  for  $Re_b = 350$  and  $Re_b = 450$ .

Figure 39b shows the mean velocity profile focused on the near wall region to highlight  $u_s$  and  $l_s$  with respect to the LRS, ARS, and SRS. As expected, the slip velocity at the LRS was higher than at the ARS for all  $Re_b$  while the slip velocity at the SRS was lower than the ARS for all  $Re_b$ . There was a trend showing an increase in the  $Re_b$  increases the slip velocity with a maximum  $u_s = 25$  mm/s. At  $Re_b > 350$  the slip length remains within 17% of each other and for  $Re_b < 350$  the slip lengths remain within a 2% range of each other. At lower  $Re_b$  a constant slip length was seen which has also been reported by Yamada et al. (2011). The exact slip lengths and slip velocities based on the ARS wall location can be seen in Table 9.

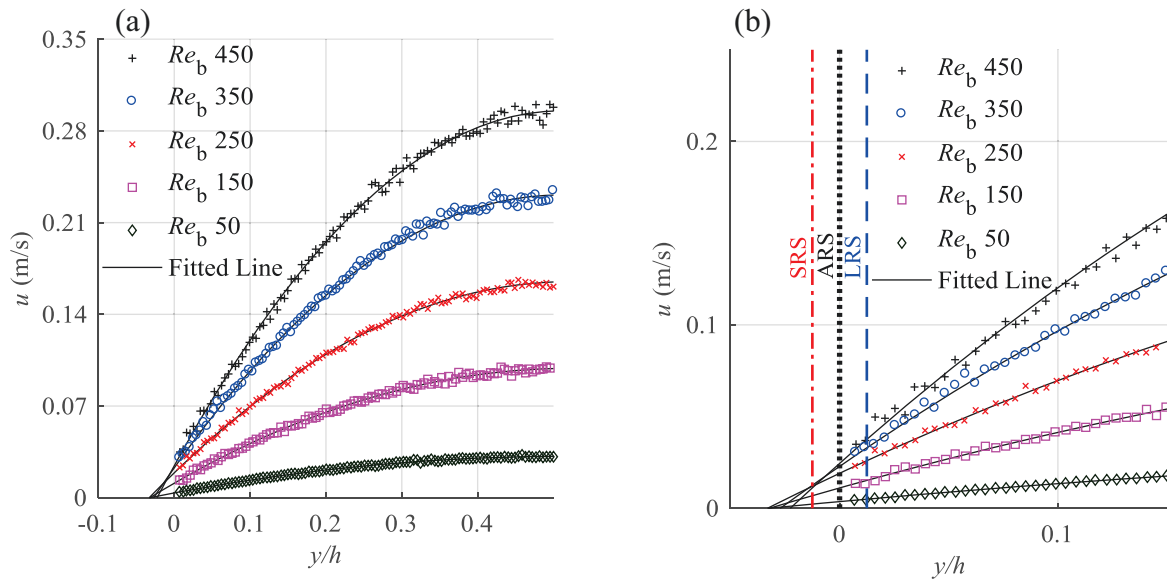


Figure 39: (a) Velocity profiles over the SHS at  $Re_b = 50, 150, 250, 350,$  and  $450$ . (b) Near wall region with the SRS (dash dot red line), ARS (dotted black line), and LRS (dashed blue line).

Table 9: PTV measurement results over the SHS at  $Re_b = 50, 150, 250, 350,$  and  $450$ .

Re	$u_s$ at ARS (m/s)	$l_s$ ( $\mu\text{m}$ ) $\pm 0.3$
450	$0.025 \pm 0.002$	48.8
350	$0.0223 \pm 0.0008$	59.0
250	$0.0195 \pm 0.0003$	71.6
150	$0.0111 \pm 0.0002$	69.9
50	$0.0036 \pm 0.0001$	70.5

The relationship between  $u_s$  and  $Re_b$  can be seen below in Figure 40 at each of the three wall locations. At  $Re_b < 350$  there was a linear trend showing an increase in  $Re_b$  leads to an increase in  $u_s$ . At  $Re_b > 350$  the increase in  $u_s$  as  $Re_b$  increased was smaller than the previous trend, and at the SRS location, showed a decreasing trend. The divergence from the linear trend that was seen below  $Re_b = 350$  was believed to be attributed to a combination of the negative channel pressure and the increased mean streamwise velocity.

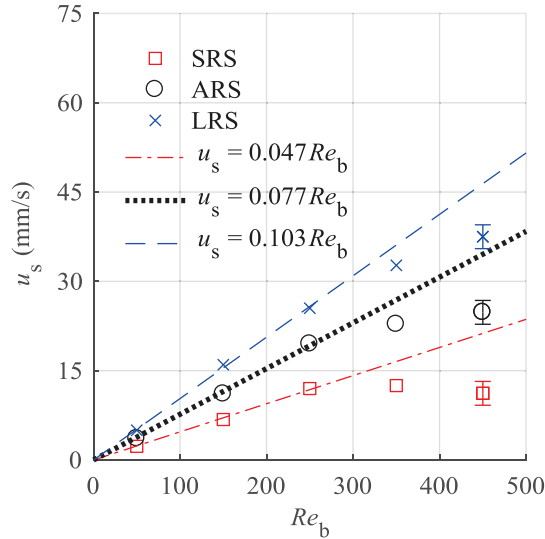


Figure 40: Slip velocity versus  $Re_b$  at the three wall locations (SRS, ARS, and LRS) over the SHS. A linear fit over the first three data points show the performance of the SHS with an intact air layer.

Figure 41 shows trend between  $DR$  and  $Re_b$  at the three wall locations. In each of the three cases, there was a trend that showed the  $DR$  ability of the surface declined significantly after  $Re_b > 250$ .

For  $Re_b < 250$  at the LRS location the  $DR$  was between 22% - 23% while at higher  $Re$  the  $DR$  falls as low as 18%. At the ARS location, the  $DR$  was ~16% at  $Re_b < 250$  and drops by 5% at the largest  $Re_b$ . The same 5% maximum decrease in  $DR$  was seen at the SRS location with a maximum  $DR$  of 10%.

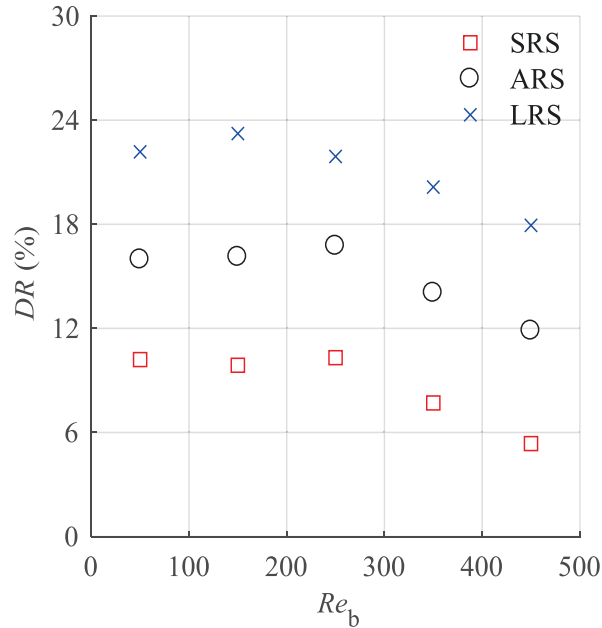


Figure 41: The trend between  $DR$  and  $Re_b$  over a SHS at the three wall locations (SRS, ARS, and LRS).

The trend showing a loss in drag reducing ability of the SHS at higher  $Re_b$  was due to a combination of the increased negative pressures in the channel and higher shear forces as  $Re_b$  increased. This was most evident in the slip length values which were fairly constant under  $Re_b = 250$  and decreased drastically above  $Re_b = 250$ . The negative pressure caused the air layer to be pulled further away from the surface, and after a pressure and shear force threshold, partial detachment of the air layer will occur and will be washed away with the flow (Dilip et al. 2014; Dilip et al. 2015). After this threshold the surface will show a decrease in drag reducing abilities, no longer exhibit drag reducing abilities, or show an increase in drag. The damage to or removal of the air layer is one of the major challenges that SHSs face before commercial use can be implemented.



# 6 Turbulent channel flow over randomly patterned superhydrophobic surfaces with varying roughness

## 6.1 Introduction

The purpose of this investigation was to determine the influence surface roughness had on the performance of a randomly patterned SHS in the turbulent flow regime. The secondary purpose of the study was to analyze the effect  $k_{rms}^+$  had on the turbulent statistics. The surfaces are classified based on their nondimensionalized root mean squared roughness,  $k_{rms}^+$ , value and are referred to as SHS<sub>0.35</sub>, SHS<sub>0.23</sub>, SHS<sub>0.18</sub>, and SHS<sub>0.14</sub>. Randomly textured SHSs with varying roughness have been studied by Ling et al. (2016). The flow was characterized with a micro particle tracking velocimetry (micro-PTV) system that obtained the velocity profile at  $Re_b = 8000$ , corresponding to  $Re_\tau = 241$  over the smooth surface.

## 6.2 Measurement over the smooth surface

Firstly to ensure the validity of the experimental setup, data was collected over a smooth surface and verified with a DNS study of turbulent channel flow by Kasagi et al. (1990) at a  $Re_\tau = 211$ . After obtaining the velocity of the tracer particles as discussed in Chapter 3.2.2, an averaging was performed to obtain the mean velocity profile. Velocities of the tracer particle were captured up to  $y^+ = 0.68$  (8.46  $\mu\text{m}$ ) from the wall over the smooth surface. Figure 42a shows the raw data and the average over the smooth surface with a bin size of  $y^+ = 0.25$ . The particles shown have a track length above 10 to reduce noise caused by lost particles during the PTV algorithm. The data has a range of velocities at each  $y^+$  location with the size of the range decreasing closer to the wall. This was due to higher velocities at the center of the channel and therefore a larger number of particles with a larger range of velocities. The high density of data points reduce biasing of the average by noise. Figure 42b shows the mean velocity profile with a least squares linear fit over the data in the viscous sublayer. From the fitted line, it was evident that the velocity reaches near zero at the wall location.

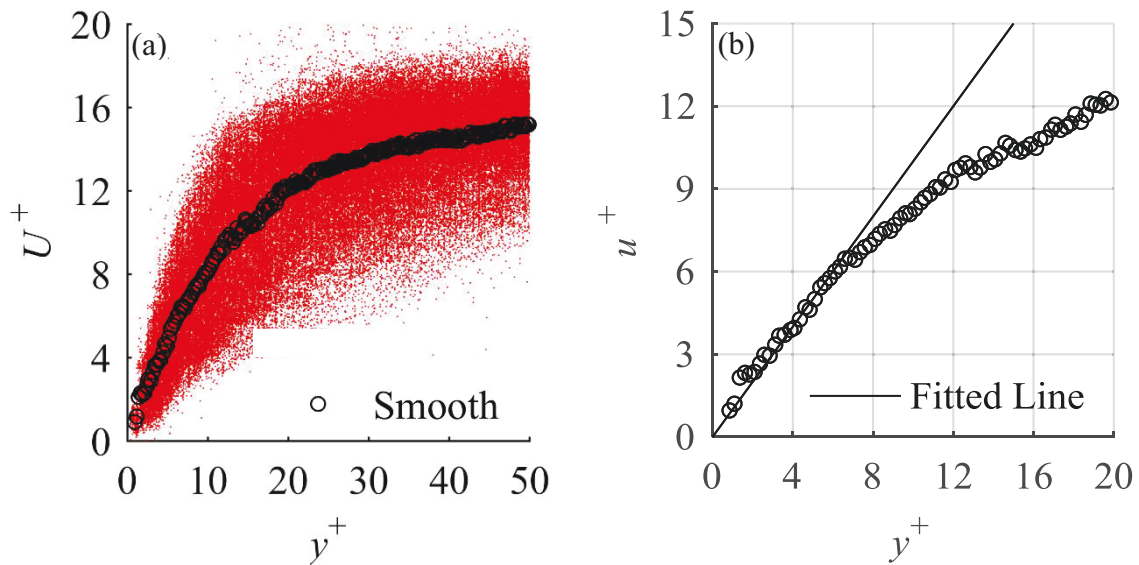


Figure 42: (a) Instantaneous velocity of tracer particles over a smooth surface and the sliding average with a bin size of  $y^+ = 0.25$ . (b) Linear fit over the sliding average in the near wall region ( $y^+ < 5$ ) for the smooth surface.

The friction velocity,  $u_{\tau 0} = 0.075$  m/s, was estimated using Clauser's method (Clauser 1956) and was confirmed by comparing to the  $u_{\tau}$  determined through calculating the slope in the linear region of the velocity profile ( $y < 0.06$  mm) to obtain the shear stress,  $\tau_w$ , and ultimately  $u_{\tau 0}$  (0.0765 m/s). The estimated value was within 2% of the  $u_{\tau}$  as determined through the slope of the fitted line. The smooth surface was compared with both the law of the wall  $u^+ = y^+$  and the log-law regions  $U^+ = y^+/\kappa + B$  which can be seen in Figure 43 where the numerical work has been added for reference. The values of  $\kappa$  and  $B$  were in agreement with the expected values at 0.39 and 5.2, respectively. The experimental data overlaps identically with the DNS results in both the viscous sublayer and log-law region. The linear trend of the data after  $y^+ = 30$  show that the turbulent channel was fully developed in the measurement domain.

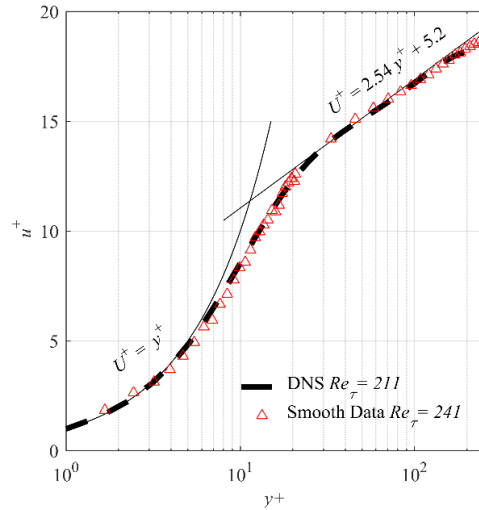


Figure 43: A comparison between the experimental data over a smooth surface ( $Re_\tau = 241$ ) to the turbulent channel flow equations with DNS by Kasagi et al. (1990) at  $Re_\tau = 211$  added for reference.

### 6.3 Measurement over the superhydrophobic surfaces

The mean velocities for each surface was obtained with a sliding averaging over the tracer particle velocities at a bin size of  $y^+ = 0.25$ . Figure 44(a, c, e, g) shows the raw data and the mean velocity profile over the four SHSs. The velocity of the tracer particles captured over the SHS were up to  $y^+ = 2.8$  ( $y = 0.03$  mm) from the wall. Again, the particles shown have a track length greater than 10 to reduce the noise caused by lost particles in the PTV algorithm. There are few outlying data points from the high-density core of the velocity profile for all surfaces attributed to the fluctuating instantaneous velocities seen in turbulent flow. Figure 44(b, d, f, h) show the mean velocity profiles of SHS and the smooth surface for comparison. The mean velocity profiles as well as any other parameter specific to a surface are normalized by the respective  $u_\tau$  obtained using the aforementioned linear fit method applied to the smooth surface. For SHS<sub>0.23</sub>, SHS<sub>0.18</sub>, and SHS<sub>0.14</sub>, there was evident finite velocities ( $0.8 < U^+ < 3.1$ ) at the wall, determined in Chapter 4.2, while the no-slip boundary condition existed over the smooth surface at  $y^+ = 0$ . For SHS<sub>0.35</sub>, there was a small slip velocity  $U^+ = 0.3$  at the wall. Away from the wall ( $y^+ > 5$ ) there was an increase in the mean velocity for every surface when compared to the smooth surface. As the surface roughness decreased there was an increase in the difference between the mean velocity of the smooth and SHSs.

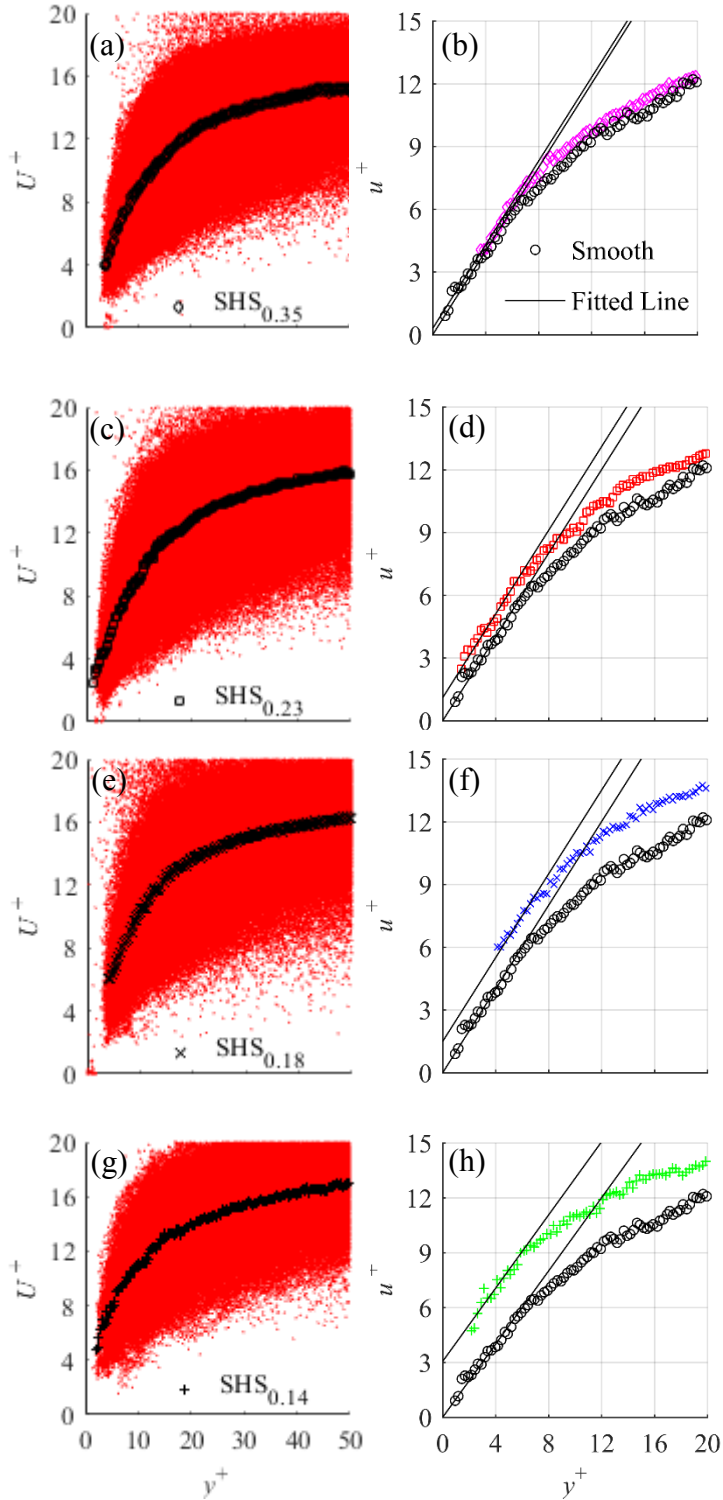


Figure 44: Instantaneous velocity of individual tracers over (a) SHS<sub>0.35</sub>, (c) SHS<sub>0.23</sub>, (e) SHS<sub>0.18</sub>, and (g) SHS<sub>0.14</sub> with a sliding average using a bin size of  $y^+ = 0.25$ . Figures (b), (d), (f), (h) show the mean velocity profile with a linear fit over the sliding average in the near wall region ( $y^+ < 5$ ) for surfaces SHS<sub>0.35</sub>, SHS<sub>0.23</sub>, SHS<sub>0.18</sub>, and SHS<sub>0.14</sub>, respectively, with the mean velocity profile of the smooth surface added for comparison.

Figure 45a below shows the semi-log plot of the average velocity against the normalized wall normal location for the four SHSs and the smooth surface. The DNS of a smooth surface at  $Re_\tau = 211$  is added along with the turbulent equations for the linear viscous sublayer and the log-law layer for reference. In the linear viscous sublayer the streamwise velocity was seen to shift upward vertically. Decreasing the surface roughness resulted in a higher vertical shift when compared to the smooth data and DNS study. This trend was also seen in the log-law layer. Min & Kim (2004) have reported these trends where the net effect of streamwise and spanwise slip cause a vertical shift compared to the smooth surface. The magnitude of the spanwise slip was seen by comparing  $u^+ - u_s^+$  versus  $y^+$ , shown in Figure 45b. The downward shift in  $u^+ - u_s^+$  as reported by Min & Kim (2004) show evidence of spanwise slip velocities most evident over SHS<sub>0.14</sub>. The magnitude of the spanwise slip velocities over the other three SHSs were not noticeable as the profiles matched the smooth surface and DNS.

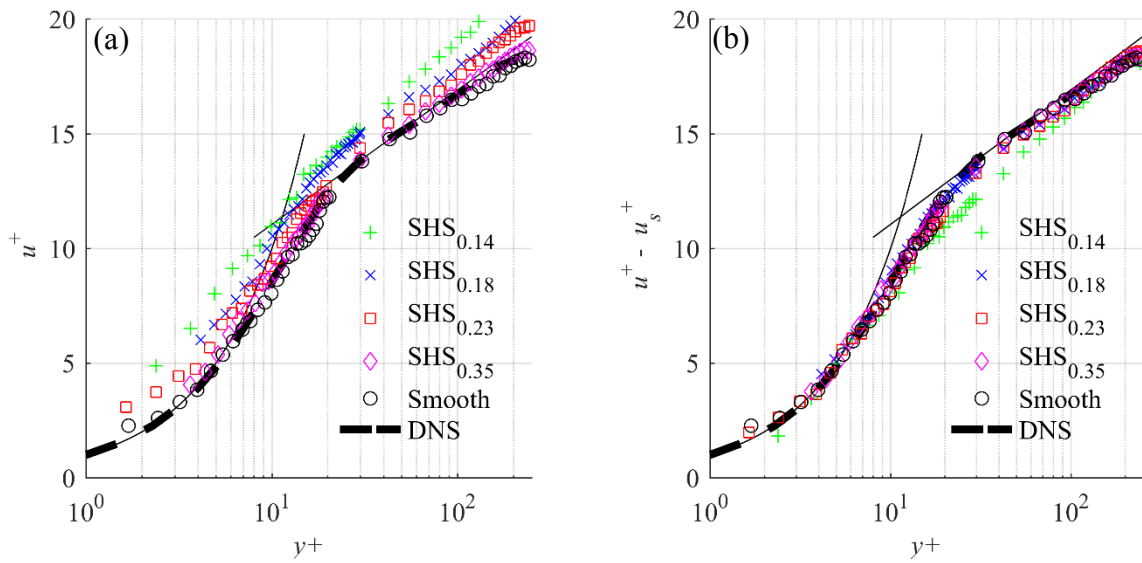


Figure 45: Semi-log plot of the averaged velocity profile of the SHSs (a) without subtraction of  $u_s^+$  (b) with subtraction of  $u_s^+$ .

The  $u_s$  as a function of the nondimensionalized root mean squared roughness is shown in Figure 46. All surfaces showed slip with the highest  $u_s$  of 208 mm/s seen over SHS<sub>0.14</sub> and the lowest  $u_s$  of 25 mm/s over SHS<sub>0.35</sub>. There was a clear trend of an inverse second order between  $u_s$  and  $k_{rms}^+$ . As  $k_{rms}^+$  increases the size of the shear free regions decrease due to the larger peaks interrupting and breaking them as reported by Alame & Mahesh (2018) and Reholon & Ghaemi (in press). The relationship shown in the figure does not work beyond the data range because extrapolation of the

equation shows a surface with a lower  $k_{rms}^+$  yields a higher  $u_s$  but there must be a minimum roughness threshold to maintain a stable air layer over the surface. The same trend was found between  $l_s$  and  $k_{rms}^+$ , which was expected due to the linear velocity profile in the viscous sublayer. Drag reduction over the SHS was estimated from the reduction of the velocity gradient,  $du/dy$ , and therefore  $\tau_w$ , as  $DR = (\tau_w - \tau_{w0})/\tau_{w0}$ . A clear trend of DR as a function of the SHS roughness was noticed, where the DR increases with the reduction in roughness as shown in Figure 47. A maximum DR of 21% was seen over SHS<sub>0.14</sub> and a drag increase by 19% was seen over SHS<sub>0.35</sub>. There was a second order trend between DR and  $k_{rms}^+$  showing that  $k_{rms}^+ > 0.21$  leads to a drag increase. For the aforementioned reasons, this trend is only valid within the surface roughness range of the figure. The results showed surfaces with higher roughness can cause a drag increase which was also seen by Ling et al. (2016).

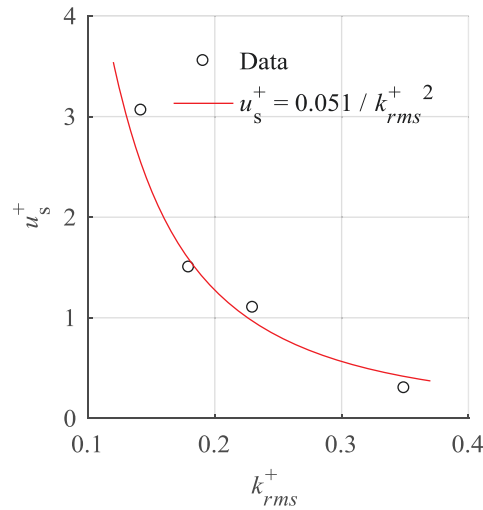


Figure 46: The nondimensional slip velocity over the SHSs as a function of the nondimensionalized root mean squared roughness.

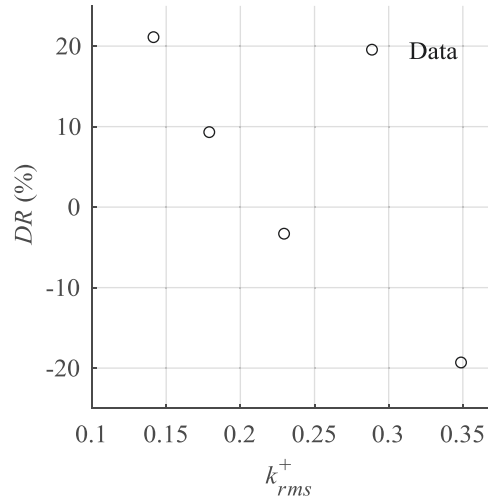


Figure 47: Drag reduction percentage as a function of the nondimensionalized root mean squared roughness.

Table 10 summarizes the parameters over the four SHSs and the smooth surface in both nondimensionalized and dimensionalized form. From the results obtained it was clear that by decreasing the  $k_{rms}^+$  of the surface the  $DR$  increases caused by an increase in  $u_s^+$ , and  $l_s^+$ , and consequently a decrease in  $u_\tau$ . The study found that a surface fabricated through this method should have a maximum  $k_{rms}^+$  of 0.21, otherwise the surface will cause a drag increase. The lower limit of  $k_{rms}^+$  before a decrease in the performance of the surface was not seen. A study of the turbulent statistics was attempted but could not be completed. The turbulent statistics can be found in Chapter 9.1.2.

Table 10: Summarized results of the four SHSs in turbulent flow.

Surface	$u_\tau$ (m/s)	$Re_\tau$	$u_s^+, u_s$ (m/s)	$u_s/u_b$	$l_s^+, l_s$ ( $\mu\text{m}$ )	$\tau_w$	$DR(\%)$
SHS <sub>0.14</sub>	0.068	218	3.1, 0.21	0.163	3.1, 42	4.6	21
SHS <sub>0.18</sub>	0.073	234	1.5, 0.11	0.068	1.5, 19	5.3	9
SHS <sub>0.23</sub>	0.079	250	1.1, 0.09	0.046	1.1, 13	6.1	-4
SHS <sub>0.35</sub>	0.084	269	0.3, 0.03	0.018	0.3, 3	7.0	-19
Smooth	0.077	246	-	-	-	5.9	-

## 7 Conclusions

Drag reduction is an area of study due to the environmental and economic benefits. Fabrication of SHSs as a drag reducing method is of interest because of its customizability, and minimal environmental impact. Two experiments studying randomly patterned SHSs were carried out in the laminar and turbulent regime.

In the laminar experiments the effect of the channel pressure on the slip velocity and drag reduction over a commercially available spray coating, NeverWet, was studied. The surfaces were subjected to flow conditions corresponding to  $50 < Re_b < 450$  in a closed loop channel. Images were recorded with a shadow-PTV system and processed with Davis 8.3. To evaluate uncertainty of the measurement system the flow over a smooth surface at five different  $Re_b$  was performed and the no slip condition at the detected wall location was confirmed. Three wall locations were identified and denoted as the LRS, ARS, and SRS. This was done by mapping the highest intensity locations across the surface (caused by reflected light) of the images in the expected wall range give the roughness profile. The experiments showed slip velocities and drag reduction at all flow conditions. The  $u_s$  was seen to increase linearly as  $Re_b$  increased until  $Re_b > 250$  and afterwards increased but at a lower rate. Before this threshold, the drag reduction was constant at 16% and afterwards decreased to as low as 11% at  $Re_b = 450$ . The slip length was on average  $71 \mu\text{m}$  at  $Re_b < 250$  and was reduced to a low of  $49 \mu\text{m}$  at higher flow conditions. It was concluded that as  $Re_b$  increased, the combination of higher shear forces and lower channel pressures caused the air layer to shift further away from the surface and allowed for partial detachment and removal.

The experiments in the turbulent regime used SHSs that were fabricated through a sandblasting, etching, and chemical deposition of PTFE process. The surfaces were visualized through SEM imaging and the roughness was determined through profilometry. Four surfaces of varying roughness, SHS<sub>0.35</sub>, SHS<sub>0.23</sub>, SHS<sub>0.18</sub>, and SHS<sub>0.14</sub>, were identified based on their  $k_{rms}^+$ . The drag reducing capabilities of the surfaces were examined as well as the effect the roughness had on the drag reduction. The turbulent channel was equipped with a micro-PTV system which captured 2000 images every second for six seconds at a rate of 10 kHz. The wall location of each surface was identified based on the intensity distribution of reflected light using images taken from the micro-PTV setup. Experiments over a smooth surface at  $Re_\tau = 241$  provided a baseline and were



verified with a DNS study at  $Re_\tau = 211$  by Kasagi et al. (1990). The  $u_{\tau 0}$  was determined by taking an average using a bin size of  $y^+ = 0.25$  over the instantaneous velocities and applying a linear fit in the near wall region ( $y^+ < 5$ ). It was determined to be within 2% of the estimation through Clausers' method at  $u_{\tau 0} = 0.0765$  m/s. The velocity profile of the SHSs was obtained by applying a sliding average with a bin size of  $y^+ = 0.25$  over the instantaneous velocities. The velocity profiles were compared to the smooth surface and there was a finite velocity at the wall and an increase in the mean velocity at every instance. By comparing the semilog plot of  $u^+$  versus  $y^+$  it was seen that every surface had slip in the streamwise direction; however, by comparing  $u^+ - u_s^+$  versus  $y^+$  it was determined that SHS<sub>0.14</sub> was the only surface to have slip in the spanwise direction. The relation between  $u_s^+$  and the roughness was seen to be  $u_s^+ = 0.051 / (k_{rms}^+)^2$  but is only believed to be valid for  $0.14 < k_{rms}^+ < 0.35$  because it is known a minimum roughness (not seen in the experiments) is required to support an air layer. The drag reduction of the surfaces was calculated to be -19%, -4%, 9%, and 21% for surfaces SHS<sub>0.35</sub>, SHS<sub>0.23</sub>, SHS<sub>0.18</sub>, and SHS<sub>0.14</sub>, respectively, based on the difference in wall shear stress compared to the smooth surface. The maximum  $k_{rms}^+$  before drag increase occurred was at 0.21.

## 7.1 Recommendations for future work

Considering the results of these experiments and the literature, the following recommendations for future work are listed below.

- Effect of roughness: Decrease the surface roughness of the SHSs so the minimum roughness required to hold an air layer can be seen. Investigate the impact of surface roughness on turbulent intensities.
- Stability and longevity of SHSs: A weakness of SHSs, as shown in this study, is the stability and performance under adverse pressures and shear rates. Designs that can withstand high pressures and a method to replenish the air are needed before SHSs can be applied on a larger scale.
- Manufacturing of SHSs: Currently most organized patterned SHSs are not made through methods suitable for production on a large scale. Cheaper and reliable manufacturing methods need to be developed for the future of this technology.

## References

- Abu Rowin, W., J. Hou, and S. Ghaemi. 2017. "Inner and Outer Layer Turbulence over a Superhydrophobic Surface with Low Roughness Level at Low Reynolds Number." *Physics of Fluids* 29 (9). doi:10.1063/1.5004398.
- Adamczyk, A. A., and L. Rimai. 1988. "2-Dimensional Particle Tracking, Velocimetry (PTV): Technique and Image Processing Algorithms." *Experiments in Fluids* 6: 373–80. doi:10.1007/BF00206543.
- Alamé, K., and K. Mahesh. 2018. "Wall-Bounded Flow over a Realistically Rough Superhydrophobic Surface." *Journal of Fluid Mechanics*, in press.
- Aljallis, E., A. Sarshar, R. Datla, V. Sikka, A. Jones, and C. Choi. 2013. "Experimental Study of Skin Friction Drag Reduction on Superhydrophobic Flat Plates in High Reynolds Number Boundary Layer Flow." *Physics of Fluids* 25 (2). doi:10.1063/1.4791602.
- American Bureau of Shipping. 2014. *Ship Energy Efficiency Measures Advisory*. Online. [https://ww2.eagle.org/content/dam/eagle/advisories-and-debriefs/ABS\\_Energy\\_Efficiency\\_Advisory.pdf](https://ww2.eagle.org/content/dam/eagle/advisories-and-debriefs/ABS_Energy_Efficiency_Advisory.pdf).
- Aussillous, P., and D. Quéré. 2004. "Shapes of Rolling Liquid Drops." *Journal of Fluid Mechanics* 512: 133–51. doi:10.1017/S0022112004009747.
- Baek, S. J., and S. J. Lee. 1996. "A New Two-Frame Particle Tracking Algorithm Using Match Probability." *Experiments in Fluids* 22 (1): 23–32. doi:10.1007/BF01893303.
- Barthlott, W., and C. Neinhuis. 1997. "Purity of the Sacred Lotus, or Escape from Contamination in Biological Surfaces." *Planta* 202 (1): 1–8. doi:10.1007/s004250050096.
- Barthlott, W., C. Neinhuis, D. Cutler, F. Ditsch, I. Meusel, I. Theisen, and H. Wilhelmi. 1998. "Classification and Terminology of Plant Epicuticular Waxes." *Botanical Journal of the Linnean Society* 126 (3): 237–60. doi:10.1006/bojl.1997.0137.
- Bhushan, B., Y. C. Jung, A. Niemiets, and K. Koch. 2009. "Lotus-like Biomimetic Hierarchical Structures Developed by the Self-Assembly of Tubular Plant Waxes." *Langmuir* 25 (3): 1659–66. doi:10.1021/la802491k.

- Byun, D., J. Hong, Saputra, J.H. Ko, Y. J. Lee, H. C. Park, B. Byun, and J. R. Lukes. 2009. "Wetting Characteristics of Insect Wing Surfaces." *Journal of Bionic Engineering* 6 (1): 63–70. doi:10.1016/S1672-6529(08)60092-X.
- Cassie, A. B. D., and S. Baxter. 1944. "Wettability of Porous Surfaces," *Transactions of the Faraday Society* 40 (5): 546–51. doi:10.1039/tf94444000546.
- Cengel, Y., and J. Cimbala. 2014. *Fluid Mechanics: Fundamentals and Applications Third Edition in SI Units*. United States: McGraw-Hill Higher Education.
- Chau, T. T., W. J. Bruckard, P. T. L. Koh, and A. V. Nguyen. 2009. "A Review of Factors That Affect Contact Angle and Implications for Flotation Practice." *Advances in Colloid and Interface Science* 150: 106–15.
- Choi, C., U. Ulmanella, J. Kim, C. Ho, and C.. Kim. 2006. "Effective Slip and Friction Reduction in Nanograted Superhydrophobic Microchannels." *Physics of Fluids* 18 (8): 1–8. doi:10.1063/1.2337669.
- Clauser, F. H. 1956. "The Turbulent Boundary Layer." *Advances in Applied Mechanics* 4 (January): 1–51. doi:10.1016/S0065-2156(08)70370-3.
- Cottin-Bizonne, C., C. Barentin, É. Charlaix, L. Bocquet, and J. L. Barrat. 2004. "Dynamics of Simple Liquids at Heterogeneous Surfaces: Molecular-Dynamics Simulations and Hydrodynamic Description." *European Physical Journal E* 15 (4): 427–38. doi:10.1140/epje/i2004-10061-9.
- Cottin-Bizonne, C., J. Barrat, L. Bocquet, and E. Charlaix. 2003. "Low-Friction Flows of Liquid at Nanopatterned Interfaces." *Nature Materials* 2: 238–40. doi:10.1038/nmat857.
- Coulson, J.M., J. F. Richardson, J. R. Backhurst, and J. H. Harker. 1995. *Fluid Flow, Heat Transfer and Mass Transfer*. Oxford, England : Butterworth-Heinemann.
- Dilip, D., M. S. Bobji, and R. N. Govardhan. 2015. "Effect of Absolute Pressure on Flow through a Textured Hydrophobic Microchannel." *Microfluidics and Nanofluidics* 19 (6): 1409–27. doi:10.1007/s10404-015-1655-4.
- Dilip, D., N. K. Jha, R. N. Govardhan, and M. S. Bobji. 2014. "Controlling Air Solubility to Maintain 'Cassie' State for Sustained Drag Reduction." *Colloids and Surfaces A:*

- Physicochemical and Engineering Aspects* 459: 217–24. doi:10.1016/j.colsurfa.2014.07.006.
- Dimitrov, A. S., P. A. Kralchevsky, A. D. Nikolov, H. Noshi, and M. Matsumoto. 1991. “Contact Angle Measurements with Sessile Drops and Bubbles.” *Journal of Colloid And Interface Science* 145 (1): 279–82. doi:10.1016/0021-9797(91)90120-W.
- Farshad, F. F., and T. C. Pesacreta. 2003. “Coated Pipe Interior Surface Roughness as Measured by Three Scanning Probe Instruments.” *Anti-Corrosion Methods and Materials* 50 (1): 6–16. doi:10.1108/00035590310456243.
- Fukagata, K., K. Iwamoto, and N. Kasagi. 2002. “Contribution of Reynolds Stress Distribution to the Skin Friction in Wall-Bounded Flows.” *Physics of Fluids* 14 (11): L73–76. doi:10.1063/1.1516779.
- Gogte, S., P. Vorobieff, R. Truesdell, A. Mammoli, F. van Swol, P. Shah, and C. J. Brinker. 2005. “Effective Slip on Textured Superhydrophobic Surfaces.” *Physics of Fluids* 17 (5): 1–4.
- Goodwyn, P. P., Y. Maezono, N. Hosoda, and K. Fujisaki. 2009. “Waterproof and Translucent Wings at the Same Time: Problems and Solutions in Butterflies.” *Naturwissenschaften* 96 (7): 781–87. doi:10.1007/s00114-009-0531-z.
- Gose, J. W., K. Golovin, M. Boban, J. M. Mabry, A. Tuteja, M. Perlin, and S. L. Ceccio. 2018. “Characterization of Superhydrophobic Surfaces for Drag Reduction in Turbulent Flow.” *Journal of Fluid Mechanics* 845: 560–80. doi:10.1017/jfm.2018.210.
- Gupta, R., V. Vaikuntanathan, and D. Sivakumar. 2016. “Superhydrophobic Qualities of an Aluminum Surface Coated with Hydrophobic Solution NeverWet.” *Colloids and Surfaces A: Physicochemical and Engineering Aspects* 500: 45–53. doi:10.1016/j.colsurfa.2016.04.017.
- Hassan, Y. A., and R. E. Canaan. 1991. “Full-Field Bubbly Flow Velocity Measurements Using a Multiframe Particle Tracking Technique.” *Experiments in Fluids* 12 (1–2): 49–60. doi:10.1007/BF00226565.
- Hellsten, Martin. 2001. “Drag-Reducing Surfactants.” *Journal of Surfactants and Detergents* 4 (1): 65–70.
- Hokmabad, B. V. 2015. “Turbulent Flow over a Superhydrophobic Surface with Isotropic Slip.” MSc Thesis, Department of Mechanical Engineering, University of Alberta.

- International Chamber of Shipping. 2017. “Shipping and World Trade.” <http://www.ics-shipping.org/shipping-facts/shipping-and-world-trade>.
- ITTC. 2008. “Uncertainty Analysis Particle Imaging Velocimetry.” In *ITTC Recommended Procedures and Guidelines*.
- Jahanmiri, M. 2011. “Particle Image Velocimetry : Fundamentals and Its Applications.” Göteborg, Chalmers University of Technology.
- Jelly, T. O., S. Y. Jung, and T. A. Zaki. 2014. “Turbulence and Skin Friction Modification in Channel Flow with Streamwise-Aligned Superhydrophobic Surface Texture.” *Physics of Fluids* 26 (9). doi:10.1063/1.4894064.
- Joanny, J. F., and P. G. De Gennes. 1984. “A Model for Contact Angle Hysteresis.” *The Journal of Chemical Physics* 81 (1): 552–62. doi:10.1063/1.447337.
- Joseph, P., C. Cottin-Bizonne, J. M. Benoît, C. Ybert, C. Journet, P. Tabeling, and L. Bocquet. 2006. “Slippage of Water Past Superhydrophobic Carbon Nanotube Forests in Microchannels.” *Physical Review Letters* 97 (15): 1–4. doi:10.1103/PhysRevLett.97.156104.
- Jung, Y. C., and B. Bhushan. 2010. “Biomimetic Structures for Fluid Drag Reduction in Laminar and Turbulent Flows.” *Journal of Physics: Condensed Matter* 22 (3): 035104. doi:10.1088/0953-8984/22/3/035104.
- Kashaninejad, N., N. T. Nguyen, and W. K. Chan. 2012. “Eccentricity Effects of Microhole Arrays on Drag Reduction Efficiency of Microchannels with a Hydrophobic Wall.” *Physics of Fluids* 24 (11). doi:10.1063/1.4767539.
- Kavalenka, M. N., F. Vüllers, S. Lischker, C. Zeiger, A. Hopf, M. Röhrig, B. E. Rapp, M. Worgull, and H. Hölscher. 2015. “Bioinspired Air-Retaining Nanofur for Drag Reduction.” *Applied Materials & Interfaces* 7: 10651–55. doi:10.1021/acsami.5b01772.
- Koch, K., B. Bhushan, and W. Barthlott. 2008. “Diversity of Structure, Morphology and Wetting of Plant Surfaces.” *Soft Matter* 4 (10): 1943–63. doi:10.1039/b804854a.
- Koch, K., A. Dommisse, and W. Barthlott. 2006. “Chemistry and Crystal Growth of Plant Wax Tubules of Lotus (*Nelumbo Nucifera*) and Nasturtium (*Tropaeolum Majus*) Leaves on Technical Substrates.” *Crystal Growth and Design* 6 (11): 2571–78. doi:10.1021/cg060035w.

- Kreuz, P., W. Arnold, and A. B. Kesel. 2001. "Acoustic Microscopic Analysis of the Biological Structure of Insect Wing Membranes with Emphasis on Their Waxy Surface." *Annals of Biomedical Engineering* 29 (12): 1054–58. doi:10.1114/1.1424921.
- Kristoffersen, R., H. I. Andersson, N. Kasagi, K. Horiuti, Y. Miyake, T. Miyauchi, and Y. Nagano. 1993. "DNS Database of Turbulence and Heat Transfer." Online. <http://thtlab.jp/>.
- Krüß. 2004. "Effect of Drop Volume on Static Contact Angles." [https://www.kruss-scientific.com/fileadmin/user\\_upload/website/literature/kruss-tn310-en.pdf](https://www.kruss-scientific.com/fileadmin/user_upload/website/literature/kruss-tn310-en.pdf).
- Kurada, S., G. W. Rankin, and K. Sridhar. 1993. "Particle-Imaging Techniques for Quantitative Flow Visualization: A Review." *Optics and Laser Technology* 25 (4): 219–34.
- Lauga, E, M. P. Brenner, and H. A. Stone. 2005. "Microfluidics: The No-Slip Boundary Condition." In *Handbook of Experimental Fluid Dynamics*. New-York: Springer.
- Lazar, E., B. Deblauw, N. Glumac, C. Dutton, and G. Elliott. n.d. "A Practical Approach to PIV Uncertainty Analysis." *27th AIAA Aerodynamic Measurement Technology and Ground Testing Conference*, 1–22.
- Lei, L., H. Li, J. Shi, and Y. Chen. 2010. "Diffraction Patterns of a Water-Submerged Superhydrophobic Grating under Pressure." *Langmuir* 26 (5): 3666–69. doi:10.1021/la903150h.
- Lien, K., J. P. Monty, M. S. Chong, and A. Ooi. 2004. "The Entrance Length for Fully Developed Turbulent Channel Flow." In *15th Australasian Fluid Mechanics Conference*, 1–4. Sydney, Australia.
- Ling, H., J. Katz, M. Fu, and M. Hultmark. 2017. "Effect of Reynolds Number and Saturation Level on Gas Diffusion in and out of a Superhydrophobic Surface." *Physical Review Fluids* 2 (12): 1–17. doi:10.1103/PhysRevFluids.2.124005.
- Ling, H., S. Srinivasan, K. Golovin, G. H. McKinley, A. Tuteja, and J. Katz. 2016. "High-Resolution Velocity Measurement in the Inner Part of Turbulent Boundary Layers over Super-Hydrophobic Surfaces." *Journal of Fluid Mechanics* 801: 670–703. doi:10.1017/jfm.2016.450.
- Martini, A., A. Roxin, R. Q. Snurr, Q. Wang, and S. Lichter. 2008. "Molecular Mechanisms of

- Liquid Slip.” *J. Fluid Mech* 600: 257–69. doi:10.1017/S0022112008000475.
- Min, Taegee, and John Kim. 2004. “Effects of Hydrophobic Surface on Skin-Friction Drag.” *Physics of Fluids* 16 (7): 1–5. doi:10.1063/1.1755723.
- Neinhuis, C., and W. Bartlott. 1997. “Characterisation and Distribution of Water-Repellent, Self-Cleaning Plant Surfaces.” *Ann. Botany* 79: 667–77. doi.org/10.1006/anbo.1997.0400
- Nguyen, S. H. T., H. K. Webb, J. Hasan, M. J. Tobin, R. J. Crawford, and E. P. Ivanova. 2013. “Dual Role of Outer Epicuticular Lipids in Determining the Wettability of Dragonfly Wings.” *Colloids and Surfaces B: Biointerfaces* 106: 126–34. doi:10.1016/j.colsurfb.2013.01.042.
- Nishio, S., and S. Murata. 2003. “A Numerical Approach to the Evaluation of Error Vector Appearance Possibility in PIV.” In *Proceedings of 5th International Symposium on Particle Image Velocimetry*, 3321.1-3321.9.
- Nobach, H. 2004. “Accuracy of Sub-Pixel Interpolation in PIV and PTV Image Processing.” In *12th Int. Symp. on Appl. of Laser Techn. to Fluid Mechanics*. Darmstadt, Germany.
- Okamoto, K., S. Nishio, T. Saga, and T. Kobayashi. 2000. “Standard Images for Particle-Image Velocimetry.” *Measurement Science and Technology* 11 (6): 685–91. doi:10.1088/0957-0233/11/6/311.
- Ou, J., B. Perot, and J. P. Rothstein. 2004. “Laminar Drag Reduction in Microchannels Using Ultrahydrophobic Surfaces.” *Physics of Fluids* 16 (12): 4635–43.
- Park, C. I., H. E. Jeong, S. H. Lee, H. S. Cho, and K. Y. Suh. 2009. “Wetting Transition and Optimal Design for Microstructured Surfaces with Hydrophobic and Hydrophilic Materials.” *Journal of Colloid and Interface Science* 336 (1): 298–303. doi:10.1016/j.jcis.2009.04.022.
- Perkins, H. J. 1970. “The Formation of Streamwise Vorticity in Turbulent Flow.” *Journal of Fluid Mechanics* 44 (4): 721–740. doi:10.1017/S0022112070002112.
- Prakash, S.S., C. J. Brinker, A. J. Hurd, and S. M. Rao. 1995. “Silica Aerogel Films Prepared at Ambient Pressure by Using Surface Derivatization to Induce Reversible Drying Shrinkage.” *Nature* 374 (6521): 439–43.
- Pritchard, P. J., R. W. Fox, and A. T. McDonald. 2011. *Introduction to Fluid Mechanics*. 8th ed. United States: John Wiley & Sons, Inc. doi:10.1212/WNL.0b013e3182315259.

- Raffel, M., C. E. Willert, S. T. Wereley, and J. Kompenhans. 2007. *Particle Image Velocimetry: A Practical Guide*. *Particle Image Velocimetry*. Vol. 2nd. doi:10.1097/JTO.0b013e3182370e69.
- Rastegari, A., and R. Akhavan. 2013. “Lattice Boltzmann Simulations of Drag Reduction by Super-Hydrophobic Surfaces.” In *Proceedings of 14th European Turbulence Conference*.
- Rastegari, A., and R. Akhavan. 2015. “On the Mechanism of Turbulent Drag Reduction with Super-Hydrophobic Surfaces.” *Journal of Fluid Mechanics* 773: R4.1-R4.14. doi:10.1017/jfm.2015.266.
- Reholon, D., and S. Ghaemi. 2018. “Plastron Morphology and Drag of a Superhydrophobic Surface in Turbulent Regime.” *Phys. Rev. Fluids*. *in press*.
- Sendner, C., D. Horinek, L. Bocquet, and R. R. Netz. 2009. “Interfacial Water at Hydrophobic and Hydrophilic Surfaces: Slip, Viscosity, and Diffusion.” *Langmuir* 25 (18): 10768–81. doi:10.1021/la901314b.
- Shafirin, E. G., and W. A. Zisman. 1960. “Constitutive Relations in the Wetting of Low Energy Surfaces and the Theory of the Retraction Method of Preparing Monolayers.” *The Journal of Physical Chemistry* 64 (5): 519–24. doi:10.1021/j100834a002.
- Shapiro, Midshipman 1/C Thomas A. 2004. “The Effect of Surface Roughness on Hydrodynamic Drag and Turbulence.” Vol. 327. United States Naval Academy, Annapolis, Maryland.
- Song, D., R.J. Daniello, and J. P. Rothstein. 2014. “Drag Reduction Using Superhydrophobic Sanded Teflon Surfaces.” *Experiments in Fluids* 55 (8). doi:10.1007/s00348-014-1783-8.
- Steck, D. A. 2015. *Classical and Modern Optics*. 1st ed. Oregon Center for Optics and Department of Physics, University of Oregon.
- Stegeman, Y. W. 1996. *Particle Tracking Velocimetry. DCT Rapporten*. Vol. 1995.100. Eindhoven: Technische Universiteit Eindhoven.
- Sun, J., and B. Bhushan. 2012. “Structure and Mechanical Properties of Beetle Wings: A Review.” *RSC Advances* 2 (33): 12606–23. doi:10.1039/c2ra21276e.
- Thomsen, F. 2008. “Practical Contact Angle Measurement ( 4 ).” *KRUSS Technical Note: TN314e*. Hamburg, Germany.

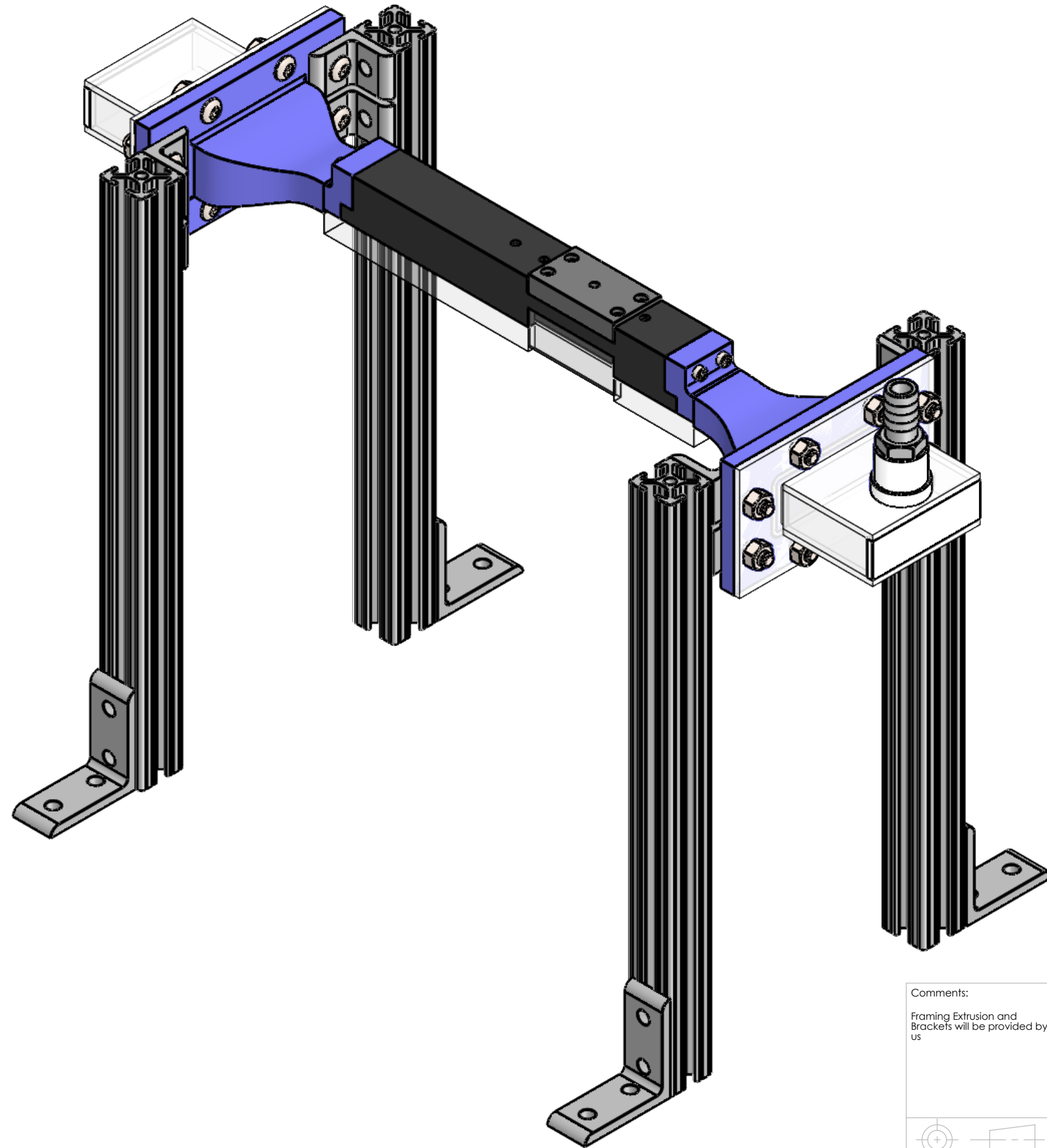


- Tretheway, D. C., and C. D. Meinhart. 2002. "Apparent Fluid Slip at Hydrophobic Microchannel Walls." *Physics of Fluids* 14 (3). doi:10.1063/1.1432696.
- Türk, S., G. Daschiel, A. Stroh, Y. Hasegawa, and B. Frohnäpfel. 2014. "Turbulent Flow over Superhydrophobic Surfaces with Streamwise Grooves." *Journal of Fluid Mechanics* 747. Cambridge University Press: 186–217. doi:10.1017/jfm.2014.137.
- Tuteja, A., W. Choi, M. Ma, J. M. Mabry, S. A. Mazzella, G. C. Rutledge, G. H. McKinley, and R. E. Cohen. 2007. "Designing Superoleophobic Surfaces." *Science* 318 (5856): 1618–22. doi:10.1126/science.1148326.
- Walsh, M., and A. Lindemann. 1984. "Optimization and Application of Riblets for Turbulent Drag Reduction." In *22nd Aerospace Sciences Meeting*, 1–10. Aerospace Sciences Meetings. American Institute of Aeronautics and Astronautics. doi:10.2514/6.1984-347.
- Wang, S., and L. Jiang. 2007. "Definition of Superhydrophobic States." *Advanced Materials* 19 (21): 3423–24. doi:10.1002/adma.200700934.
- Wang, Y., X. Liu, H. Zhang, and Z. Zhou. 2015. "Superhydrophobic Surfaces Created by a One-Step Solution-Immersion Process and Their Drag-Reduction Effect on Water." *RSC Advances* 5. Royal Society of Chemistry: 18909–14. doi:10.1039/C5RA00941C.
- Wenzel, R. N. 1936. "Resistance of Solid Surfaces to Wetting by Water." *Journal of Industrial and Engineering Chemistry (Washington, D. C.)* 28: 988–94. doi:10.1021/ie50320a024.
- Yamada, T., C. Hong, O. J. Gregory, and M. Faghri. 2011. "Experimental Investigations of Liquid Flow in Rib-Patterned Microchannels with Different Surface Wettability." *Microfluidics and Nanofluidics* 11 (1): 45–55. doi:10.1007/s10404-011-0771-z.
- Young, I.T., R. Zagers, L.J. van Vliet, J. Mullikin, F. Boddeke, and H. Netten. 1993. "Depth-of-Focus in Microscopy." In *Proceedings of the 8th Scandinavian Conference on Image Analysis*, 493–498.
- Young, T. 1805. "An Essay on the Cohesion of Fluids." *Philosophical Transactions of the Royal Society of London* 95: 65–87. doi:10.1098/rstl.1805.0005.
- Zhang, J., H. Tian, Z. Yao, P. Hao, and N. Jiang. 2015. "Mechanisms of Drag Reduction of Superhydrophobic Surfaces in a Turbulent Boundary Layer Flow." *Experiments in Fluids* 56



(9). Springer Berlin Heidelberg: 1–13. doi:10.1007/s00348-015-2047-y.

Zhang, Ji., Z. Yao, and P. Hao. 2016. “Drag Reductions and the Air-Water Interface Stability of Superhydrophobic Surfaces in Rectangular Channel Flow.” *Physical Review E* 94: 1–7. doi:10.1103/PhysRevE.94.053117.

## 8 Appendix A – Laminar channel drawing package



SOLIDWORKS Educational Product. For Instructional Use Only

Comments: Framing Extrusion and Brackets will be provided by us	UNLESS OTHERWISE SPECIFIED: DIMENSIONS ARE IN MM TOLERANCES: ANGULAR: $\pm 0.5^\circ$ LINEAR X = $\pm 0.5$ X.X = $\pm 0.1$ X.XX = $\pm 0.025$	DRAWN BY: Daren Wilkinson	 The Department of Mechanical Engineering UNIVERSITY OF ALBERTA
	 SURFACE FINISH $0.6 \mu\text{m}$ ✓ DO NOT SCALE DRAWING	Friday, October 05, 2018 2:35:36 AM	
MATERIAL:	FILE NAME: Upsidedown_Encompassing Assembly	Supervisor: Sina Ghaemi	SIZE <b>B</b>
		SCALE: 1:2	REV 1 SHEET 1 OF 2

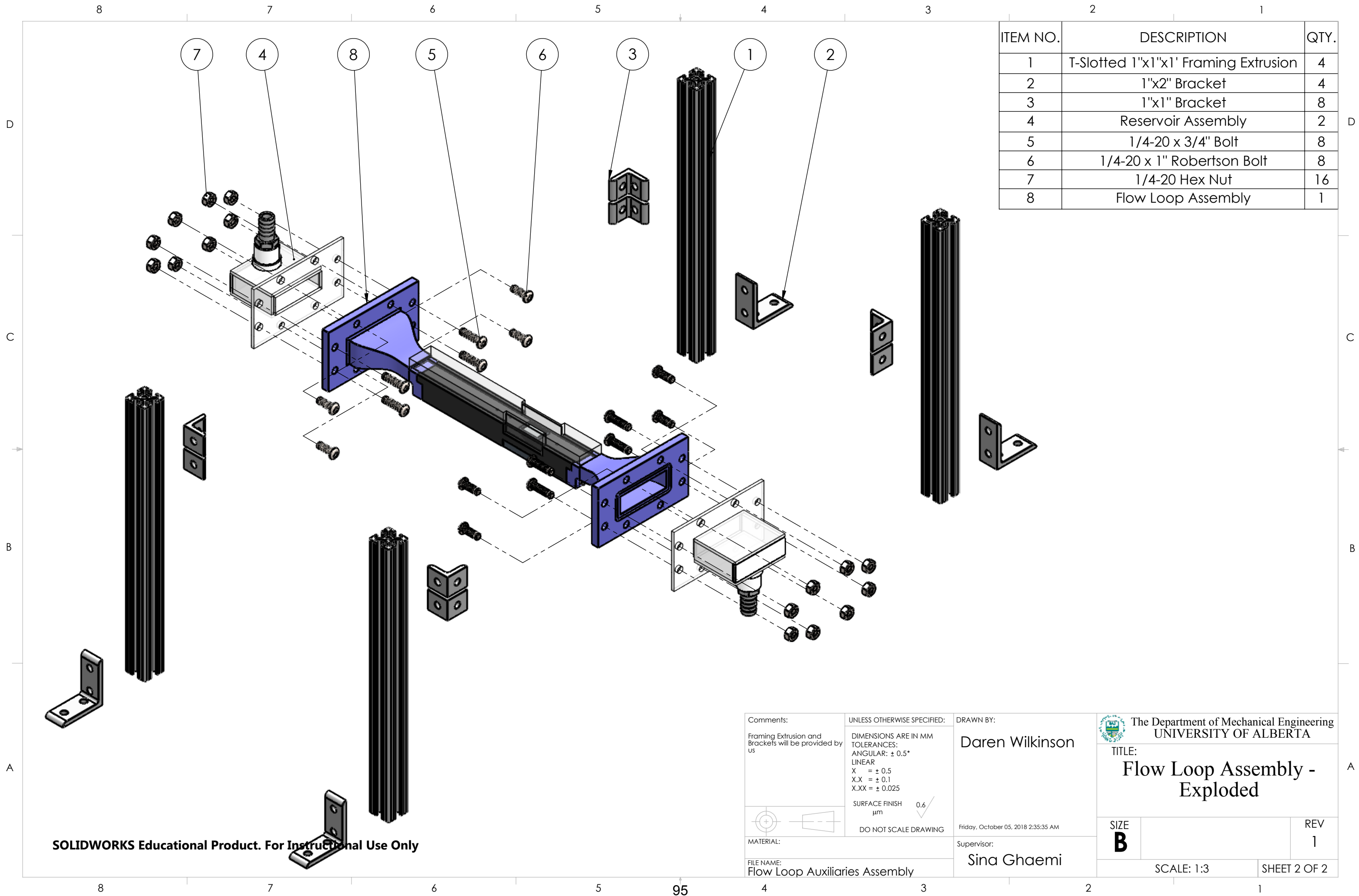
8 7 6 5 4 3 2 1

D  
C  
B  
A

D  
C  
B  
A

8 7 6 5 4 3 2 1

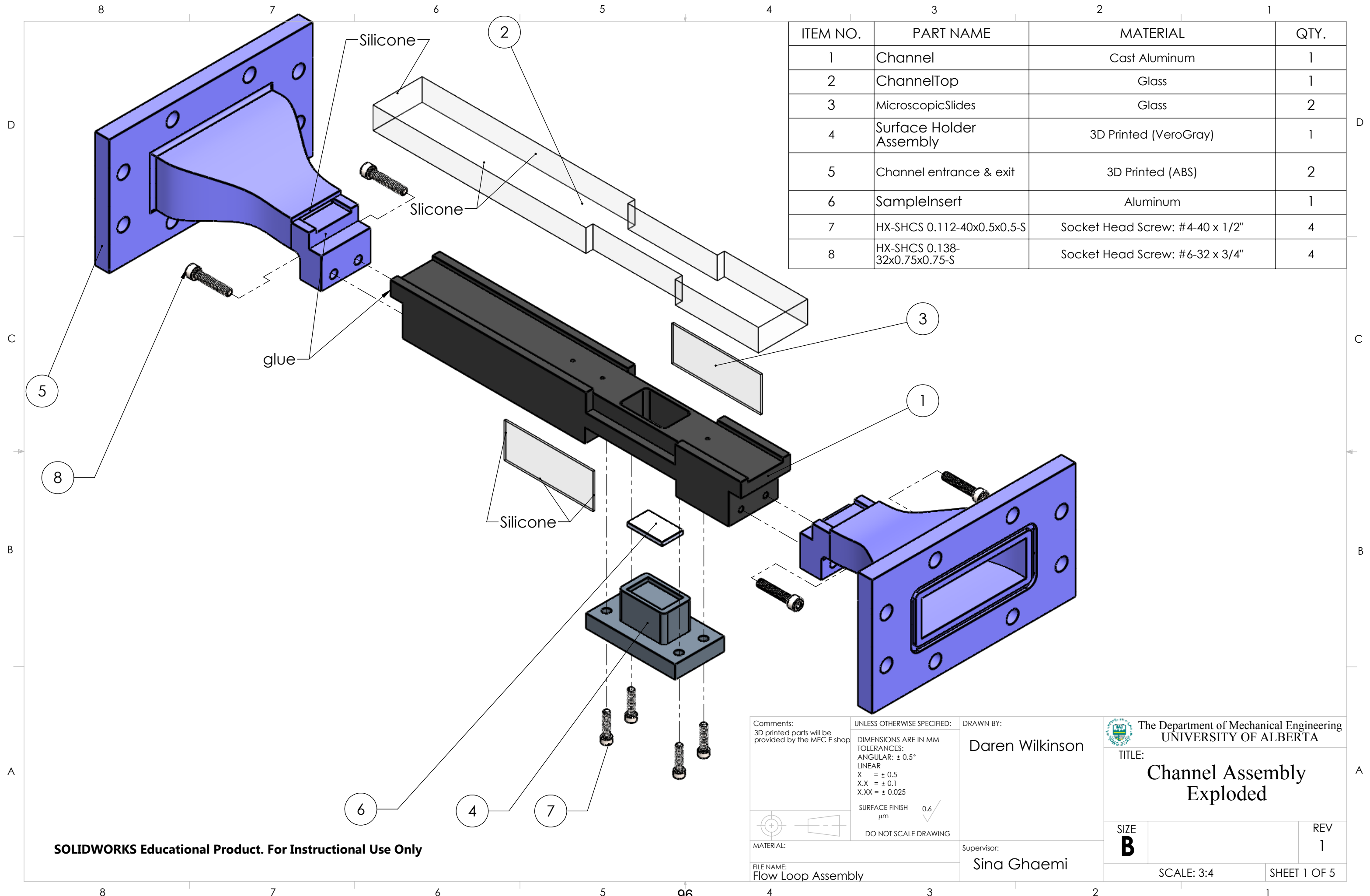
94



ITEM NO.	DESCRIPTION	QTY.
1	T-Slotted 1"x1"x1' Framing Extrusion	4
2	1"x2" Bracket	4
3	1"x1" Bracket	8
4	Reservoir Assembly	2
5	1/4-20 x 3/4" Bolt	8
6	1/4-20 x 1" Robertson Bolt	8
7	1/4-20 Hex Nut	16
8	Flow Loop Assembly	1

Comments: Framing Extrusion and Brackets will be provided by us	UNLESS OTHERWISE SPECIFIED: DIMENSIONS ARE IN MM TOLERANCES: ANGULAR: ± 0.5° LINEAR X = ± 0.5 X.X = ± 0.1 X.XX = ± 0.025  SURFACE FINISH 0.6 μm ✓ DO NOT SCALE DRAWING	DRAWN BY: Daren Wilkinson	The Department of Mechanical Engineering UNIVERSITY OF ALBERTA
		Friday, October 05, 2018 2:35:35 AM	
MATERIAL: FILE NAME: Flow Loop Auxiliaries Assembly	Supervisor: Sina Ghaemi	SIZE <b>B</b>	REV 1
		SCALE: 1:3	SHEET 2 OF 2

SOLIDWORKS Educational Product. For Instructional Use Only



ITEM NO.	PART NAME	MATERIAL	QTY.
1	Channel	Cast Aluminum	1
2	ChannelTop	Glass	1
3	MicroscopicSlides	Glass	2
4	Surface Holder Assembly	3D Printed (VeroGray)	1
5	Channel entrance & exit	3D Printed (ABS)	2
6	SampleInsert	Aluminum	1
7	HX-SHCS 0.112-40x0.5x0.5-S	Socket Head Screw: #4-40 x 1/2"	4
8	HX-SHCS 0.138-32x0.75x0.75-S	Socket Head Screw: #6-32 x 3/4"	4

Comments:  
3D printed parts will be provided by the MEC E shop

UNLESS OTHERWISE SPECIFIED:  
DIMENSIONS ARE IN MM  
TOLERANCES:  
ANGULAR: ± 0.5°  
LINEAR  
X = ± 0.5  
X.X = ± 0.1  
X.XX = ± 0.025

SURFACE FINISH 0.6  
µm ✓

DO NOT SCALE DRAWING

MATERIAL:

FILE NAME:  
Flow Loop Assembly

DRAWN BY:  
Daren Wilkinson

Supervisor:  
Sina Ghaemi

The Department of Mechanical Engineering  
UNIVERSITY OF ALBERTA

TITLE:  
**Channel Assembly Exploded**

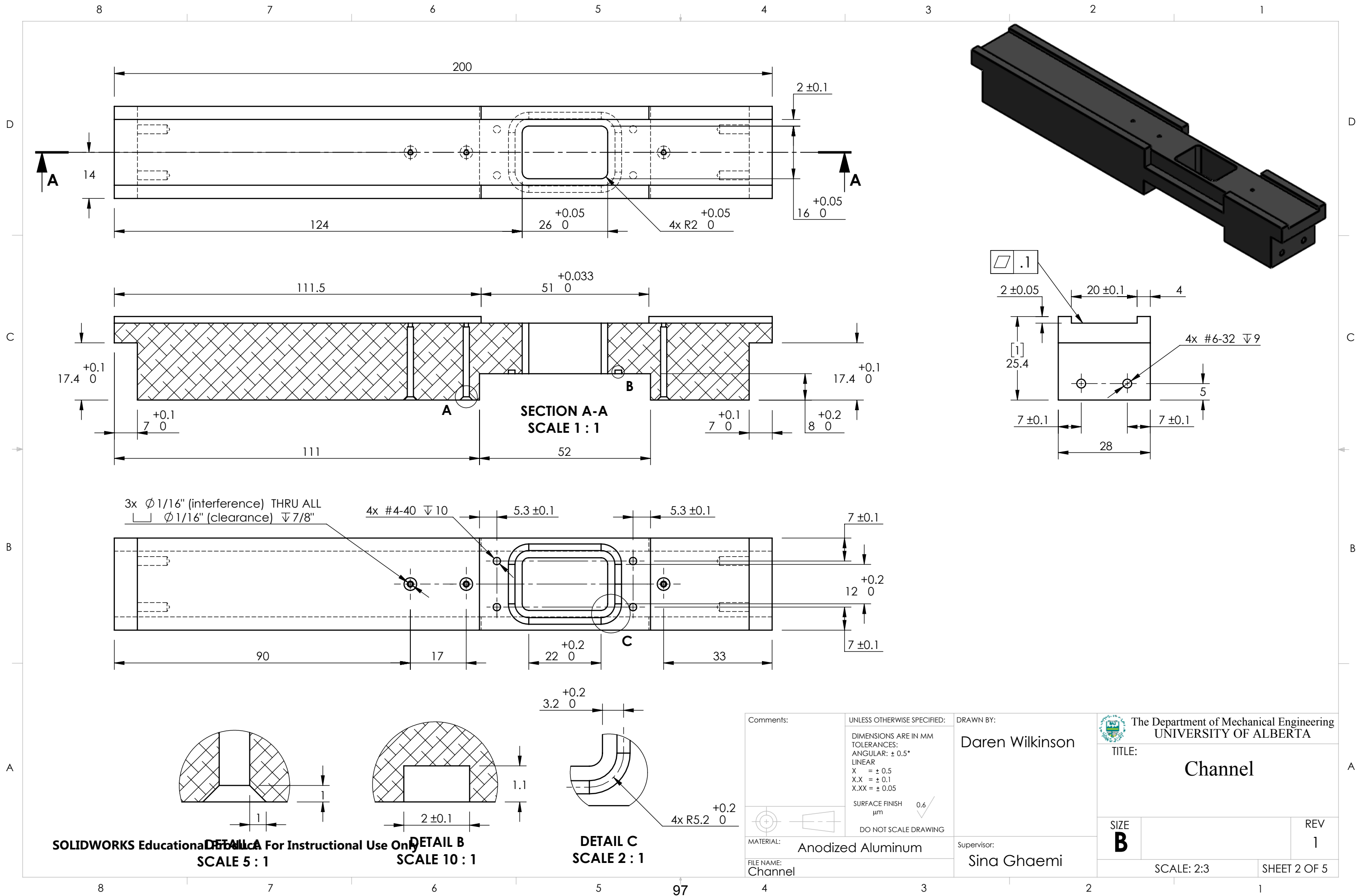
SIZE **B**

SCALE: 3:4

REV 1

SHEET 1 OF 5

SOLIDWORKS Educational Product. For Instructional Use Only



SOLIDWORKS Educational Edition For Instructional Use Only

Comments:	UNLESS OTHERWISE SPECIFIED: DIMENSIONS ARE IN MM TOLERANCES: ANGULAR: $\pm 0.5^\circ$ LINEAR X = $\pm 0.5$ X.X = $\pm 0.1$ X.XX = $\pm 0.05$ SURFACE FINISH $\mu\text{m}$ 0.6 ✓ DO NOT SCALE DRAWING	DRAWN BY: Daren Wilkinson	The Department of Mechanical Engineering UNIVERSITY OF ALBERTA TITLE: <b>Channel</b> SIZE <b>B</b> REV 1 SCALE: 2:3 SHEET 2 OF 5
MATERIAL: Anodized Aluminum	Supervisor: Sina Ghaemi		
FILE NAME: Channel			

8 7 6 5 4 3 2 1

D

D

C

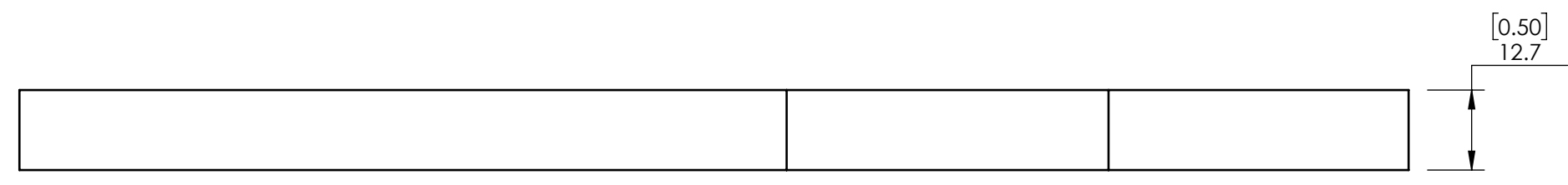
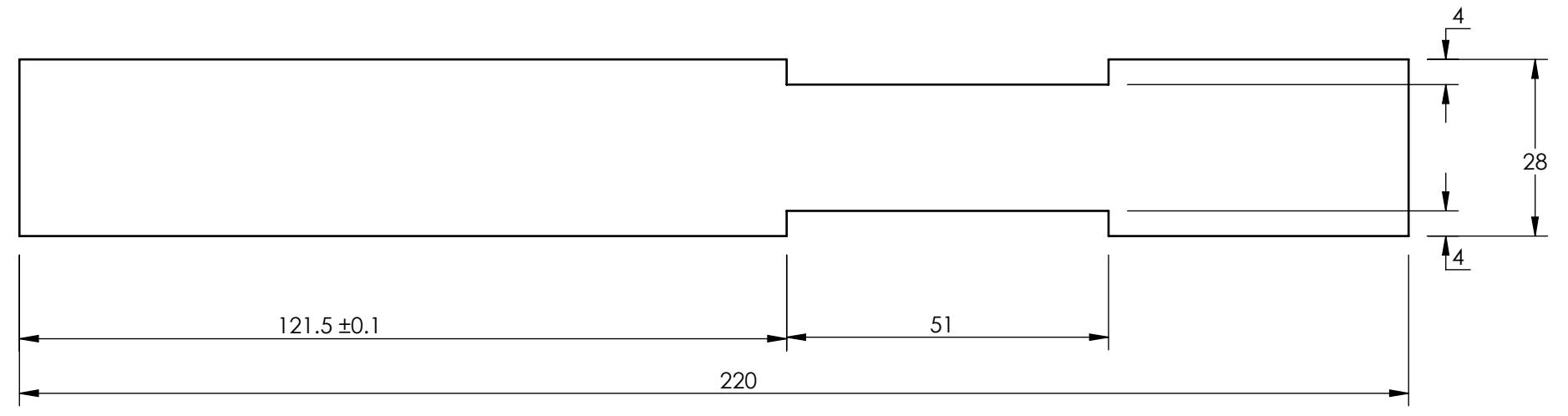
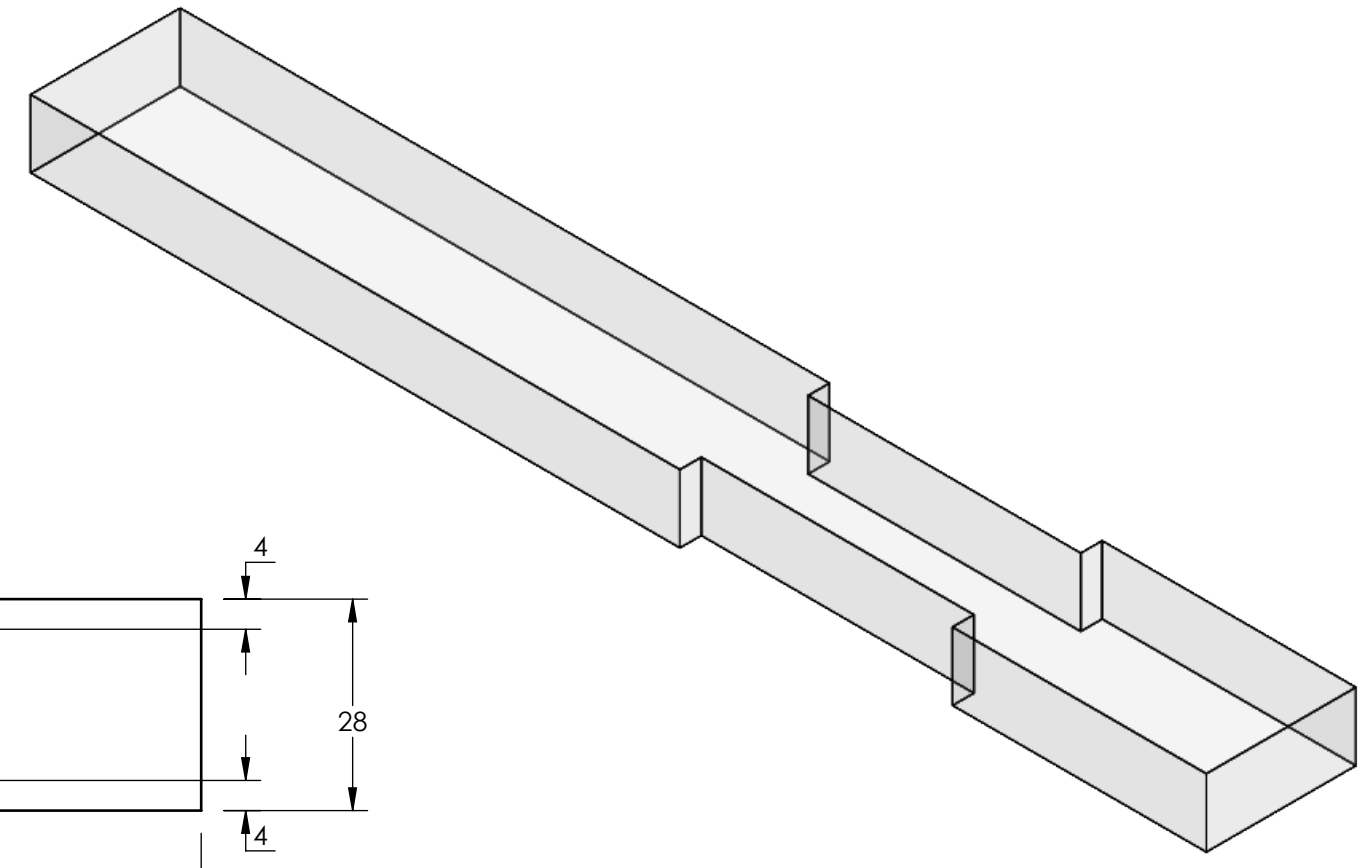
C

B



B

A

A



SOLIDWORKS Educational Product. For Instructional Use Only

Comments:	UNLESS OTHERWISE SPECIFIED:	DRAWN BY:	The Department of Mechanical Engineering UNIVERSITY OF ALBERTA	
	DIMENSIONS ARE IN MM TOLERANCES: ANGULAR: ± 0.5° LINEAR X = ± 0.5 X.X = ± 0.1 X.XX = ± 0.025	Daren Wilkinson	TITLE: <b>Glass Top</b>	
 	SURFACE FINISH μm	Supervisor:	SIZE	REV
	0.6 ✓ DO NOT SCALE DRAWING	Sina Ghaemi	<b>B</b>	1
MATERIAL: Glass	FILE NAME: ChannelTop	SCALE: 1:2		SHEET 3 OF 5

8 7 6 5 4 3 2 1

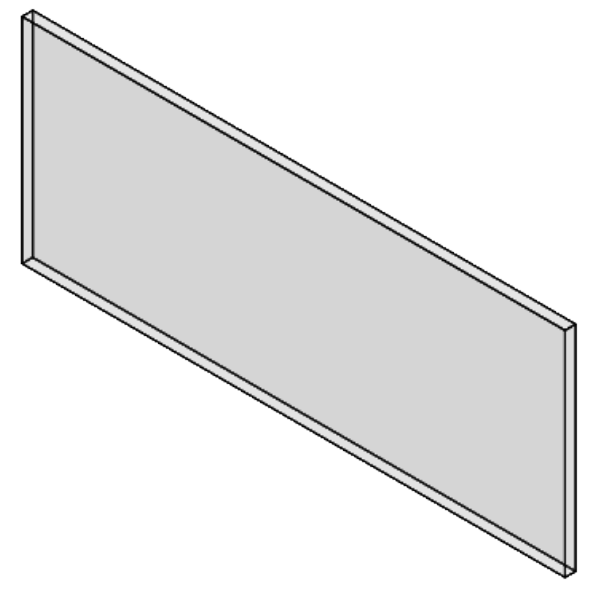
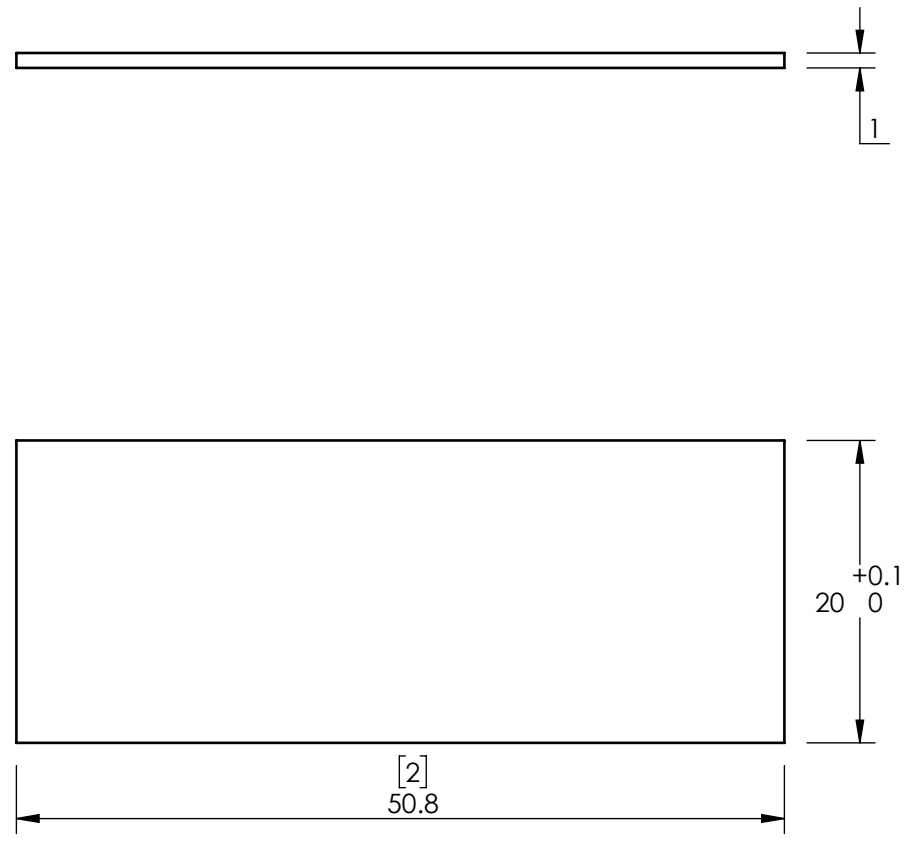
98





8 7 6 5 4 3 2 1

D  
C  
B  
A

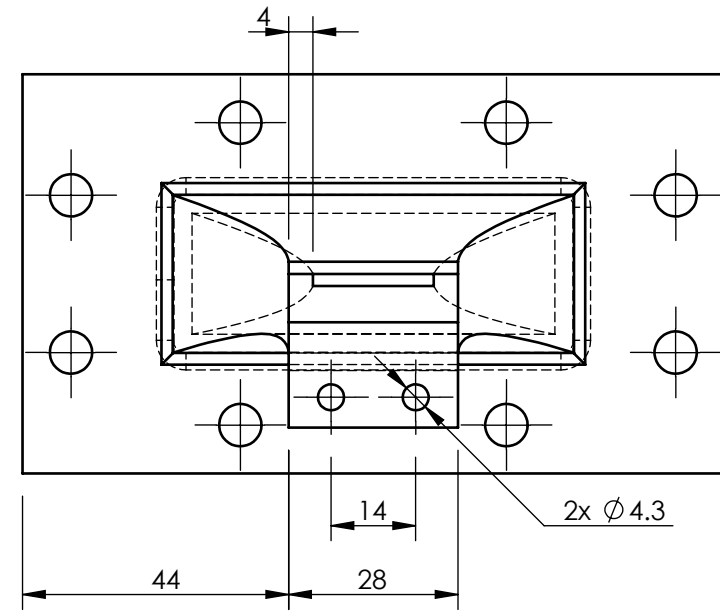
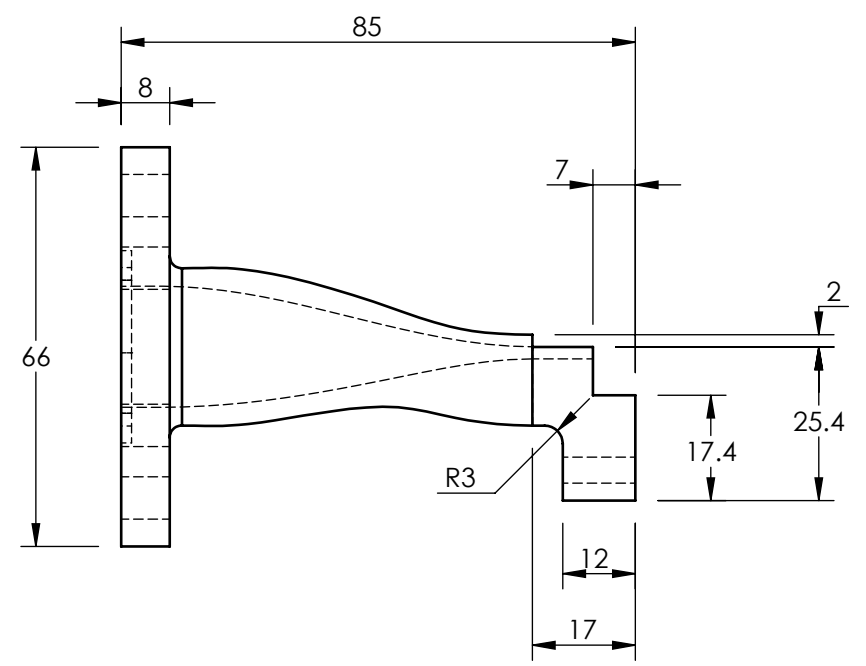
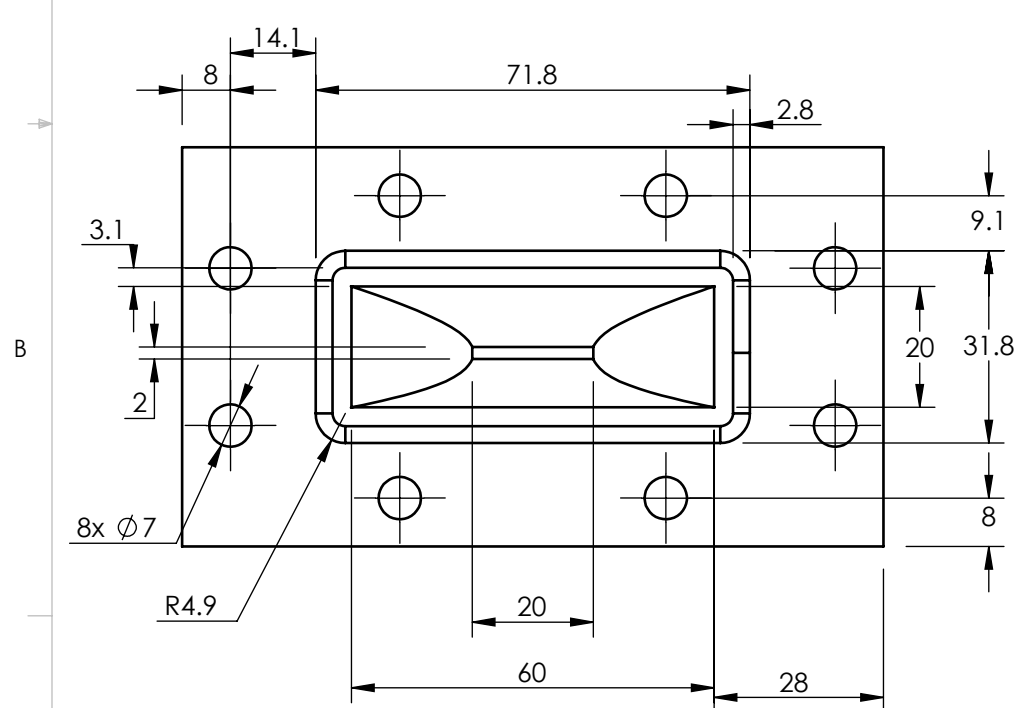
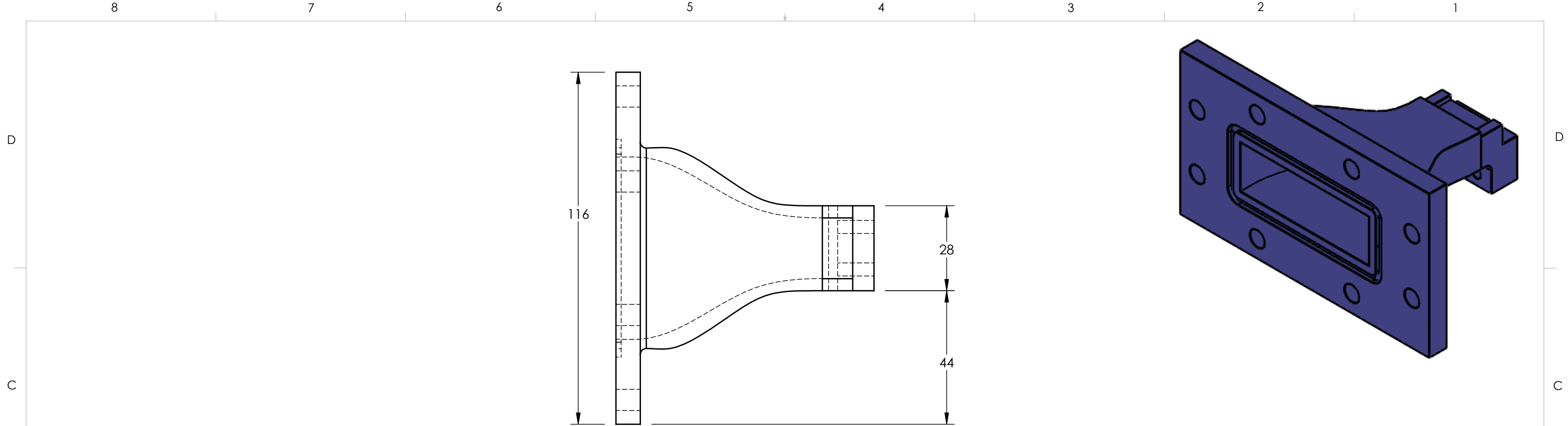
D  
C  
B  
A



SOLIDWORKS Educational Product. For Instructional Use Only

Comments:	UNLESS OTHERWISE SPECIFIED:	DRAWN BY:	 The Department of Mechanical Engineering UNIVERSITY OF ALBERTA	
	DIMENSIONS ARE IN MM TOLERANCES: ANGULAR: ± 0.5° LINEAR X = ± 0.5 X.X = ± 0.1 X.XX = ± 0.025  SURFACE FINISH 0.6 μm ✓ DO NOT SCALE DRAWING	Daren Wilkinson	TITLE: <b>Microscope Slide</b>	
	MATERIAL: Glass	Supervisor:	SIZE <b>B</b>	REV 1
FILE NAME: MicroscopicSlides		Sina Ghaemi	SCALE: 2:1	SHEET 4 OF 5

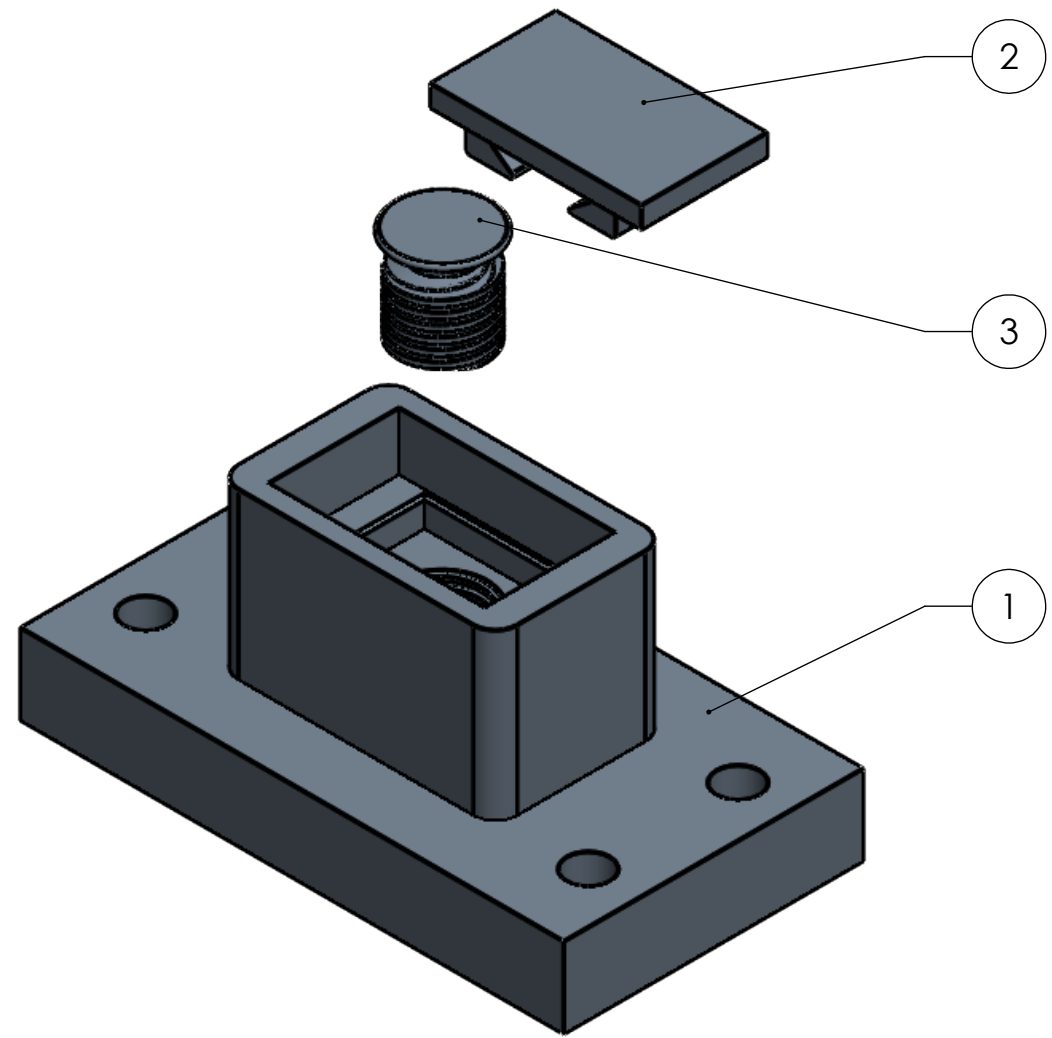
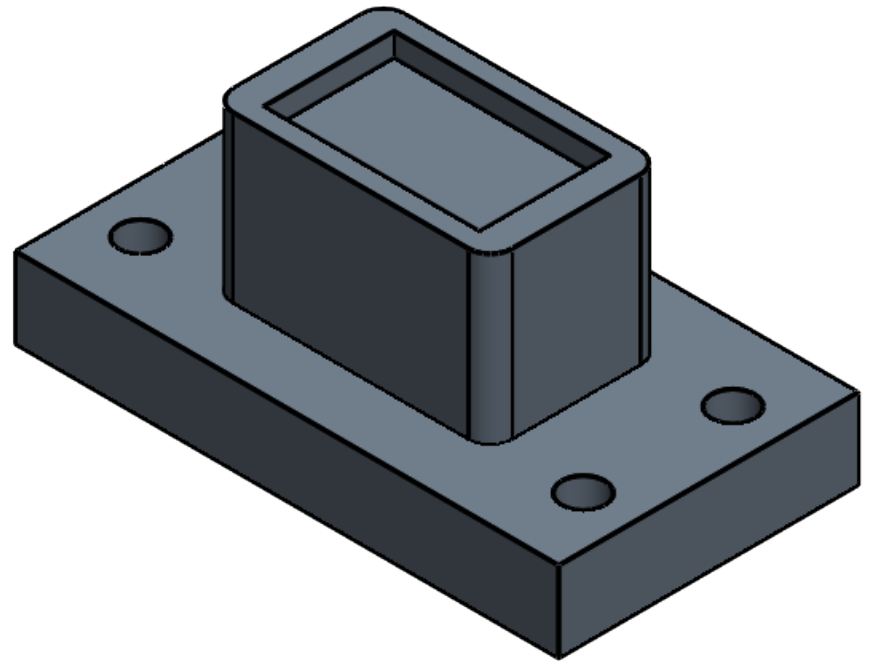
7 6 5 99 4 3 2 1



Comments:	UNLESS OTHERWISE SPECIFIED:	DRAWN BY:	The Department of Mechanical Engineering UNIVERSITY OF ALBERTA	
	DIMENSIONS ARE IN MM TOLERANCES: ANGULAR: $\pm 0.5^\circ$ LINEAR X = $\pm 0.5$ X.X = $\pm 0.1$ X.XX = $\pm 0.025$ SURFACE FINISH $0.6 \mu\text{m}$ DO NOT SCALE DRAWING	Daren Wilkinson	TITLE: <b>Channel Entrance &amp; Exit</b>	
MATERIAL: <b>ABS</b> FILE NAME: Nozzle_Diffuser	Supervisor:	Sina Ghaemi	SIZE <b>B</b>	REV 1
			SCALE: 4:5	SHEET 5 OF 5

SOLIDWORKS Educational Product. For Instructional Use Only

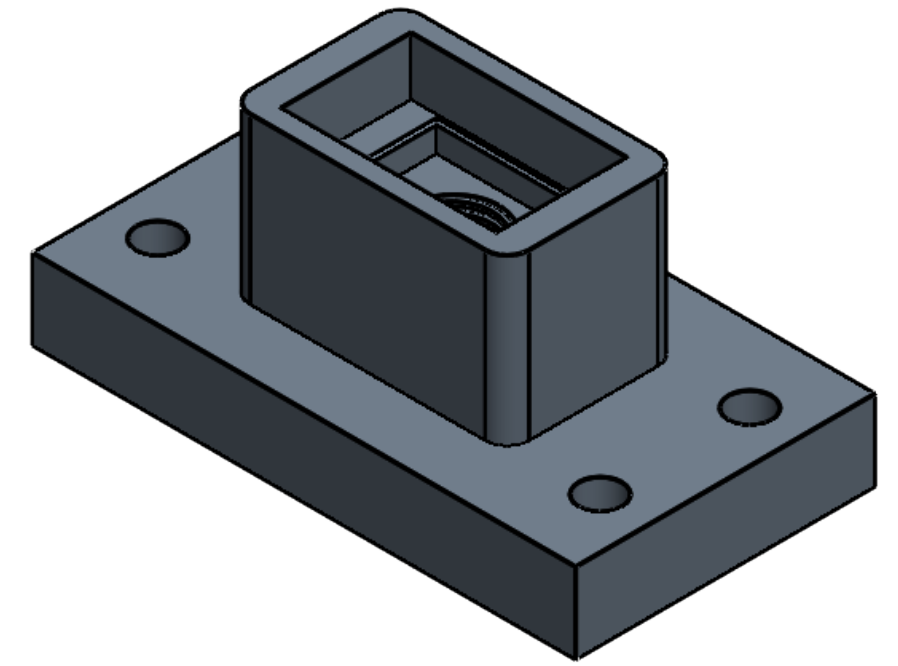
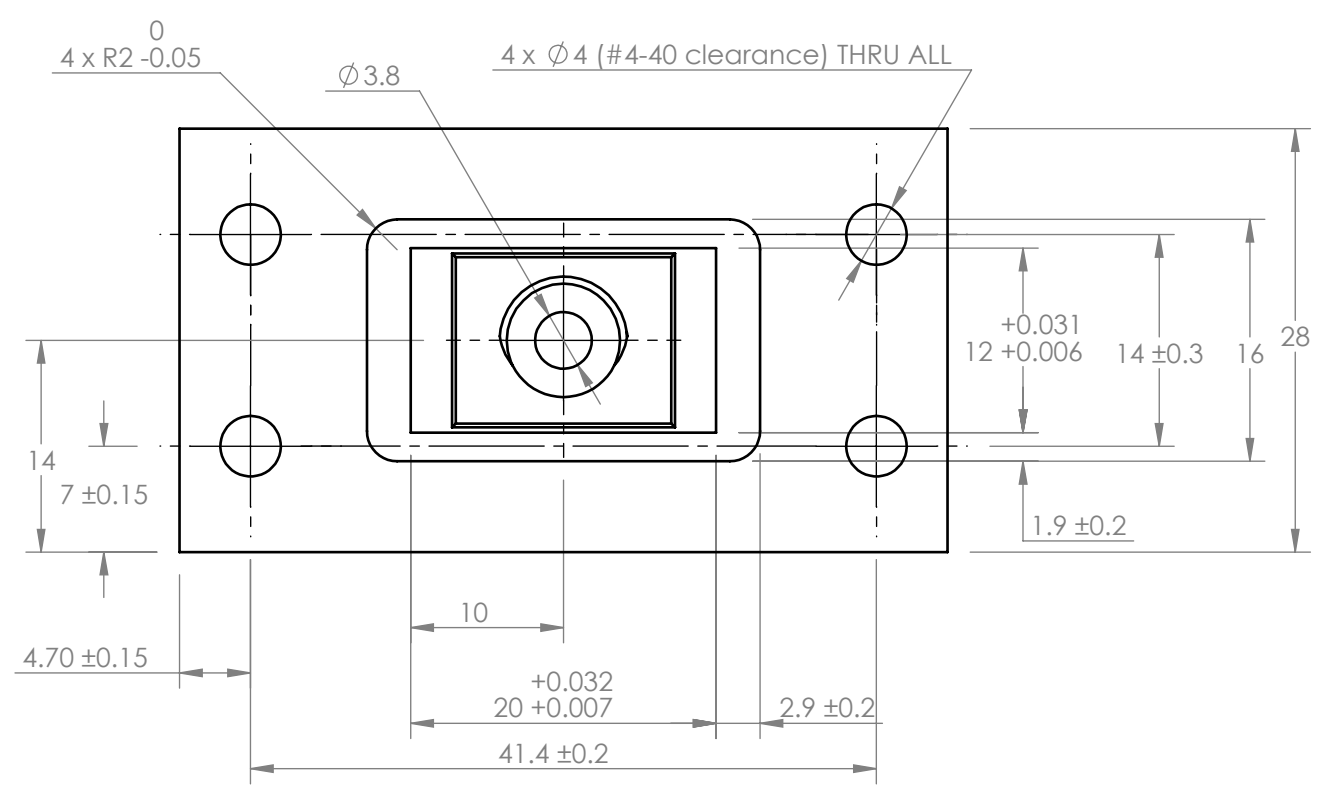
ITEM NO.	PART NAME	DESCRIPTION	QTY.
1	Surafce holder	3D Printed (VeroGray)	1
2	Stage	3D Printed (VeroGray)	1
3	Stagescrew	3D Printed (VeroGray)	1



Comments:	UNLESS OTHERWISE SPECIFIED:	DRAWN BY:	 The Department of Mechanical Engineering UNIVERSITY OF ALBERTA	
	DIMENSIONS ARE IN MM TOLERANCES: ANGULAR: $\pm 0.5^\circ$ LINEAR X = $\pm 0.5$ X.X = $\pm 0.1$ X.XX = $\pm 0.05$  SURFACE FINISH $0.6 \mu\text{m}$ ✓ DO NOT SCALE DRAWING	Daren Wilkinson		TITLE: Sample Holder Assembly
MATERIAL:		Supervisor:	SIZE <b>B</b>	REV 1
FILE NAME: Surface_Holder_Assembly		Sina Ghaemi	SCALE: 2:1	
			SHEET 1 OF 4	

8 7 6 5 4 3 2 1

D



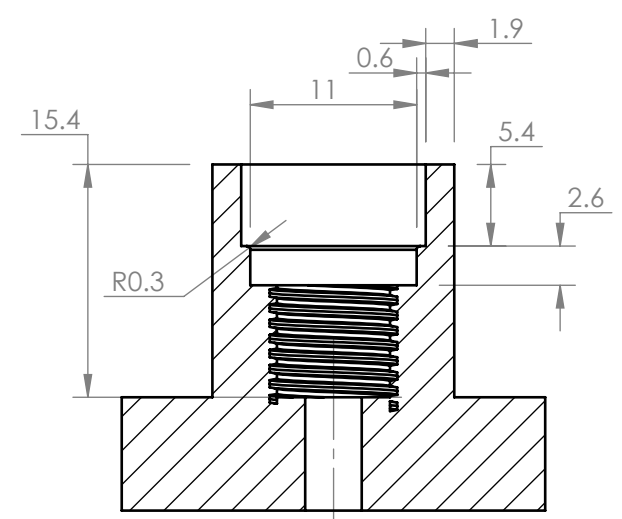
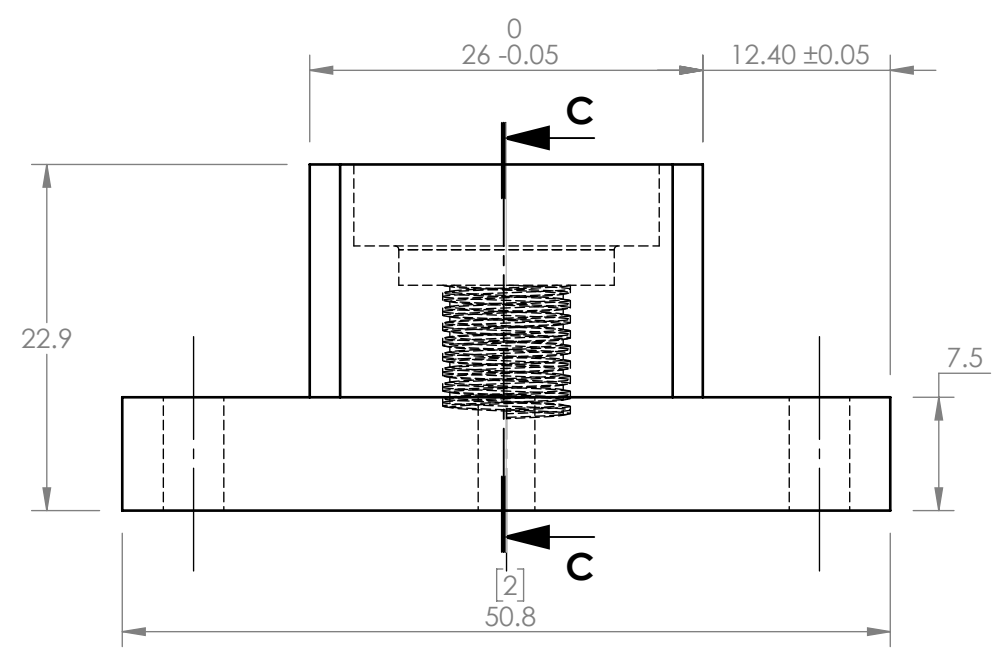
D

C

C

B

B

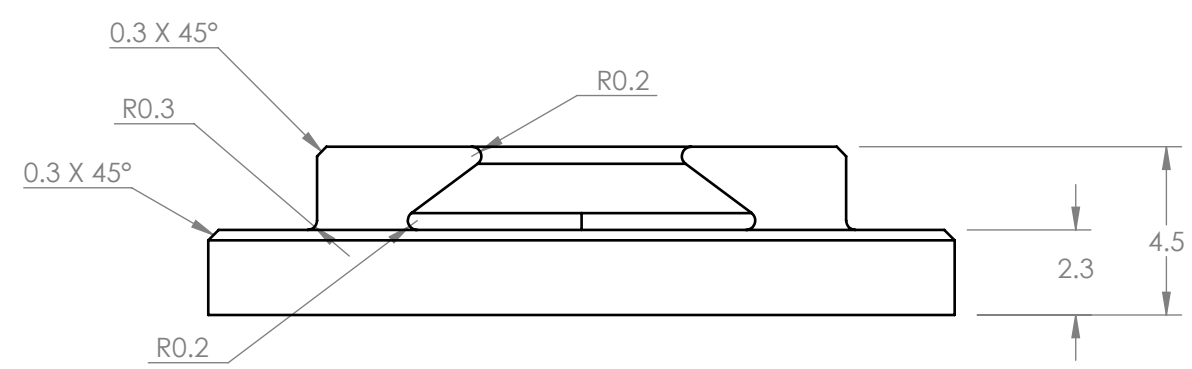
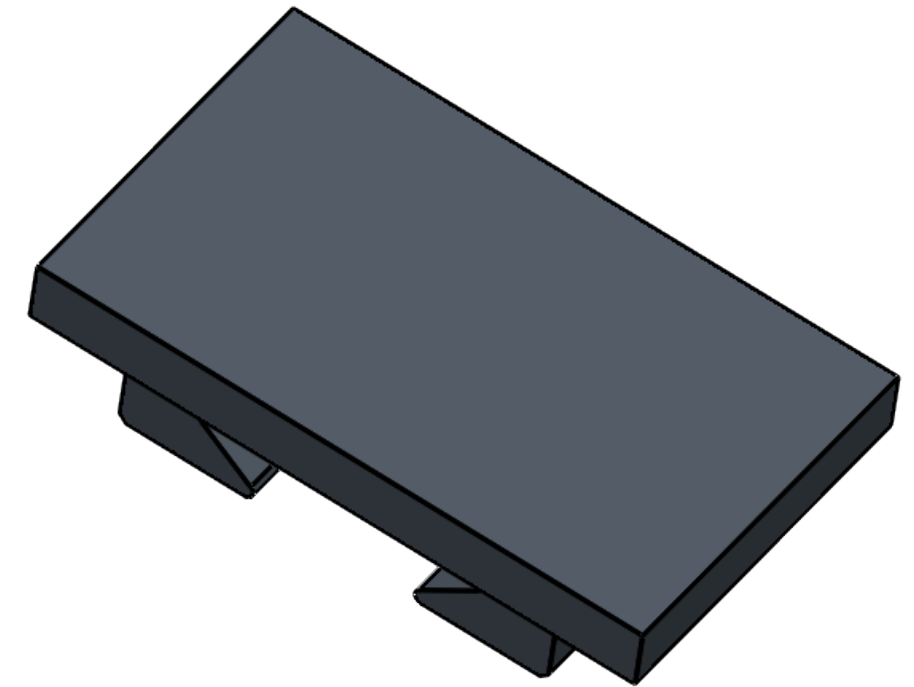
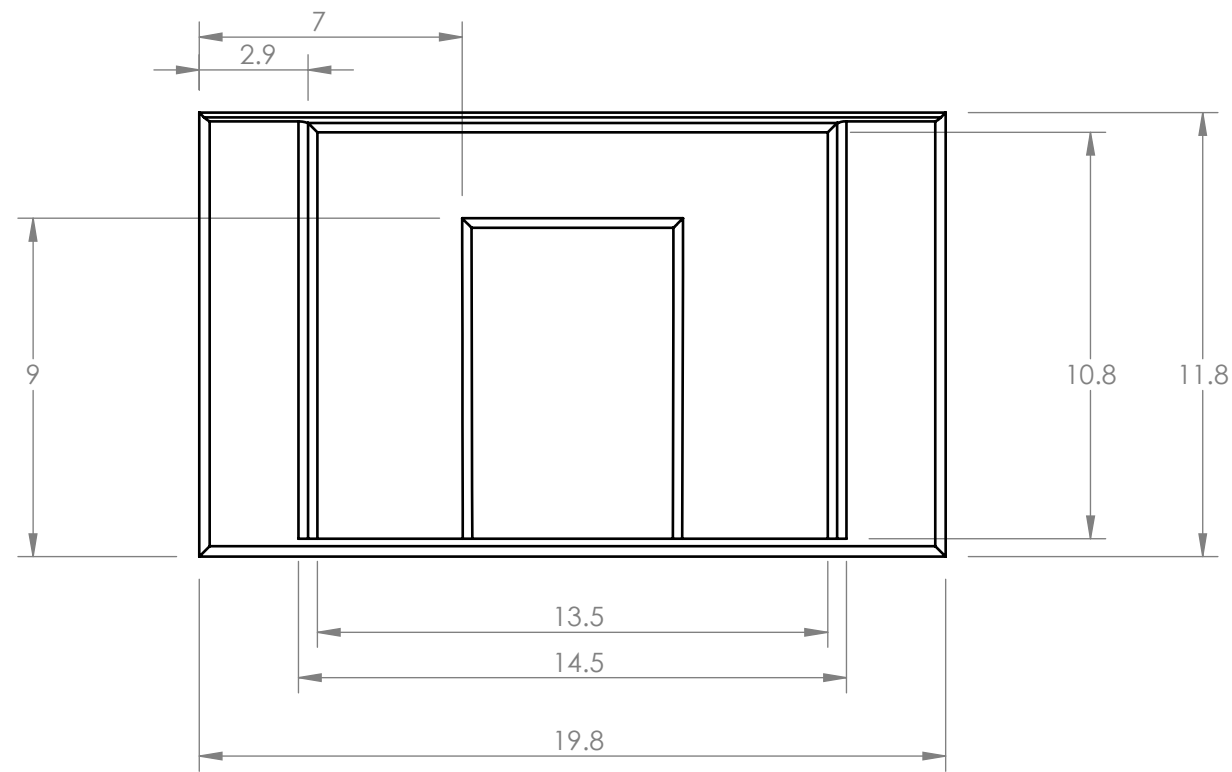


SECTION C-C

SOLIDWORKS Educational Product. For Instructional Use Only

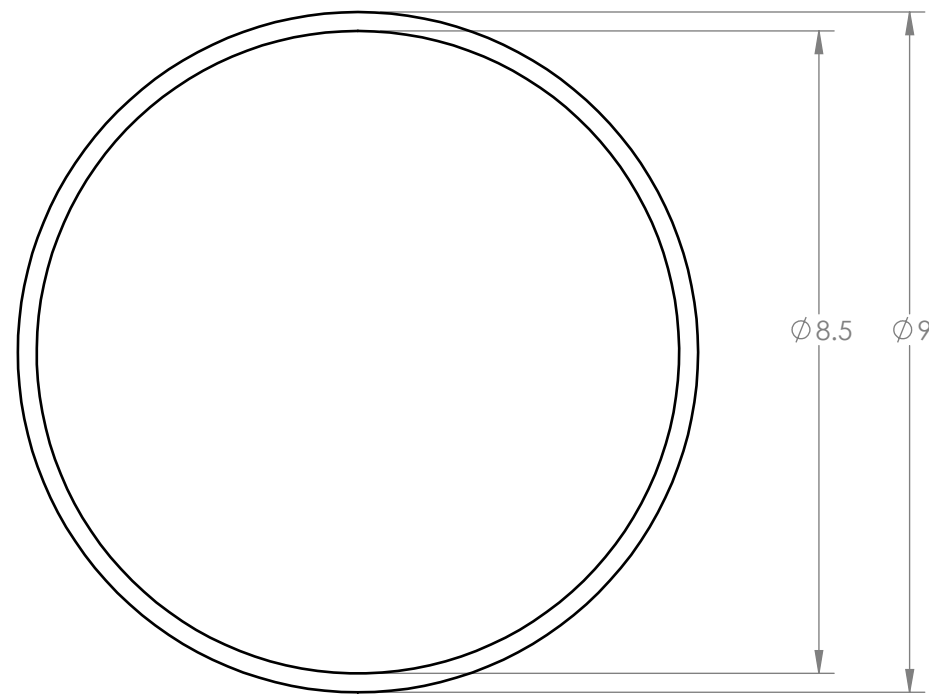
Comments: Part is to be 3D printed with VeroGray in MecE shop	UNLESS OTHERWISE SPECIFIED: DIMENSIONS ARE IN MM TOLERANCES: ANGULAR: ± 0.5° LINEAR X = ± 0.5 X.X = ± 0.1 X.XX = ± 0.05 SURFACE FINISH 0.6 μm ✓ DO NOT SCALE DRAWING	DRAWN BY: Daren Wilkinson	The Department of Mechanical Engineering UNIVERSITY OF ALBERTA	
	MATERIAL: VeroGray FILE NAME: Surafce holder	Supervisor: Sina Ghaemi	TITLE: Sample Holder	
		SIZE <b>B</b>	REV 1	SCALE: 2:1 SHEET 2 OF 4

8 7 6 5 102 4 3 2 1

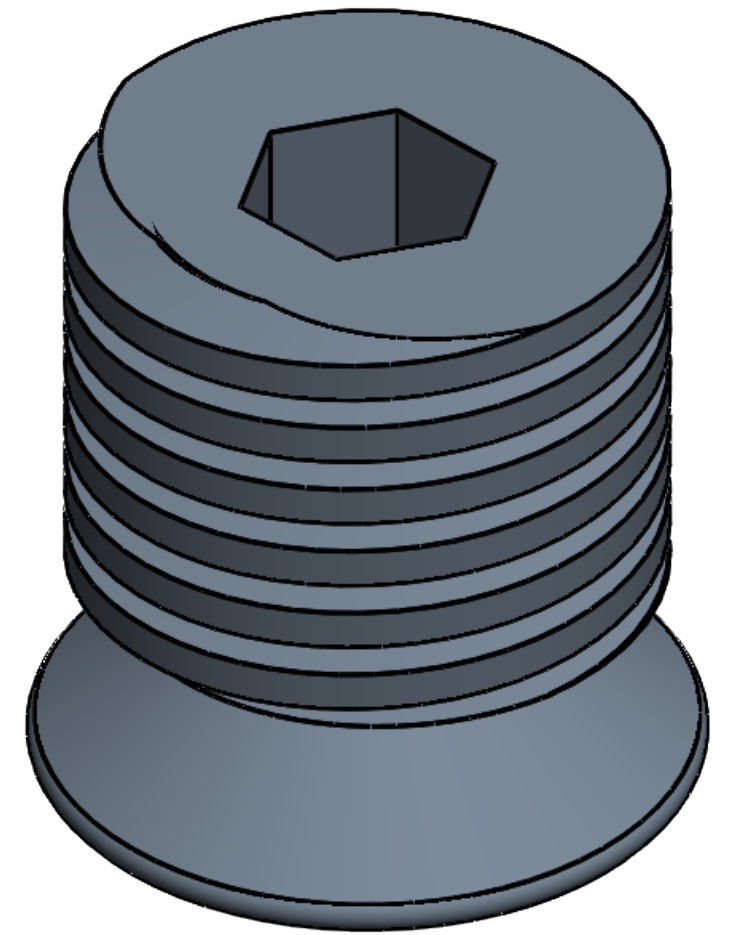
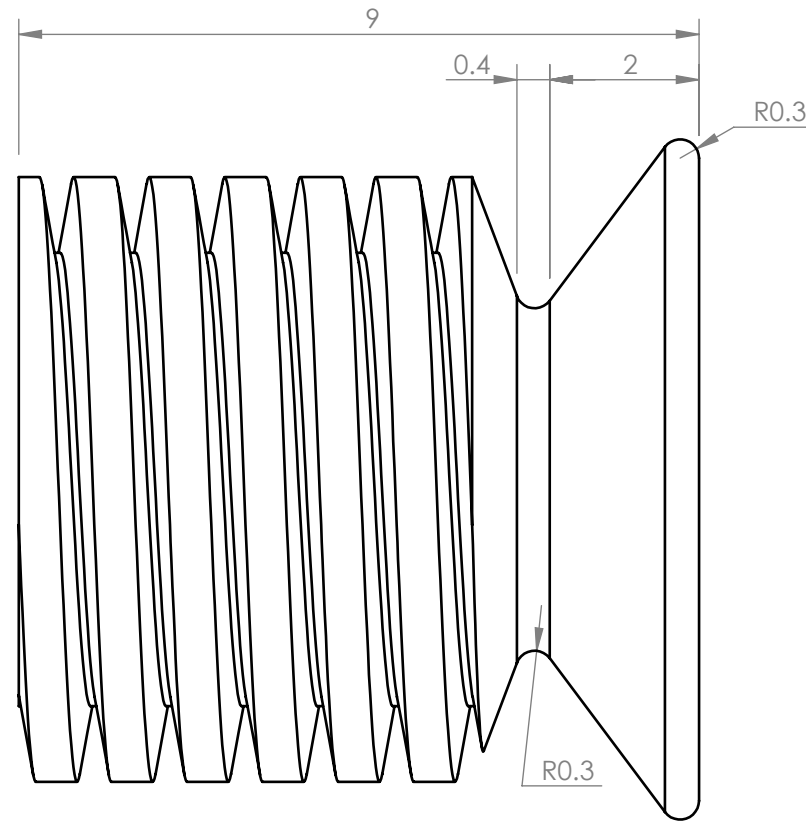
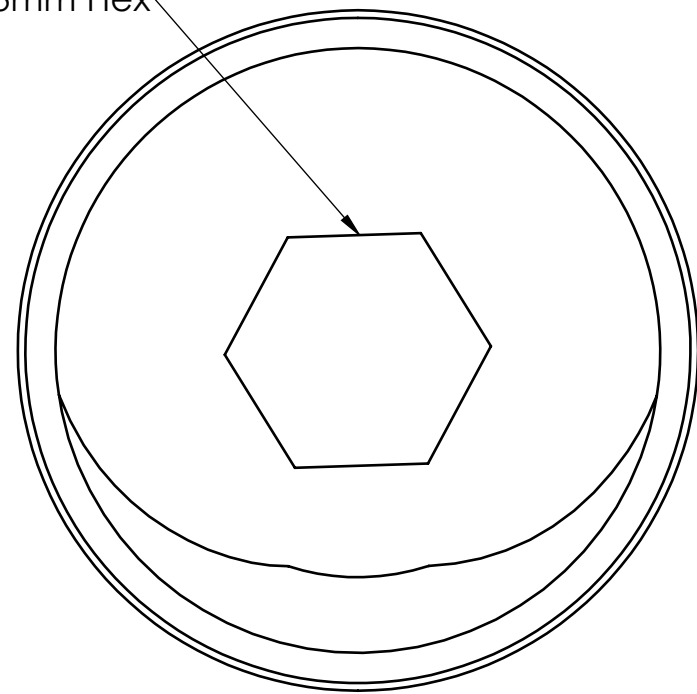




SOLIDWORKS Educational Product. For Instructional Use Only

Comments: Part is to be 3D printed with VeroGray in MecE shop	UNLESS OTHERWISE SPECIFIED: DIMENSIONS ARE IN MM TOLERANCES: ANGULAR: $\pm 0.5^\circ$ LINEAR X = $\pm 0.5$ X.X = $\pm 0.1$ X.XX = $\pm 0.05$	DRAWN BY: Daren Wilkinson	The Department of Mechanical Engineering UNIVERSITY OF ALBERTA	
	SURFACE FINISH $0.6 \mu\text{m}$ ✓ DO NOT SCALE DRAWING	Supervisor: Sina Ghaemi	TITLE: <h1 style="text-align: center;">Stage</h1>	
MATERIAL: VeroGray FILE NAME: StageWithoutScrew	SIZE <b>B</b>	SCALE: 5:1	REV 1	SHEET 3 OF 4

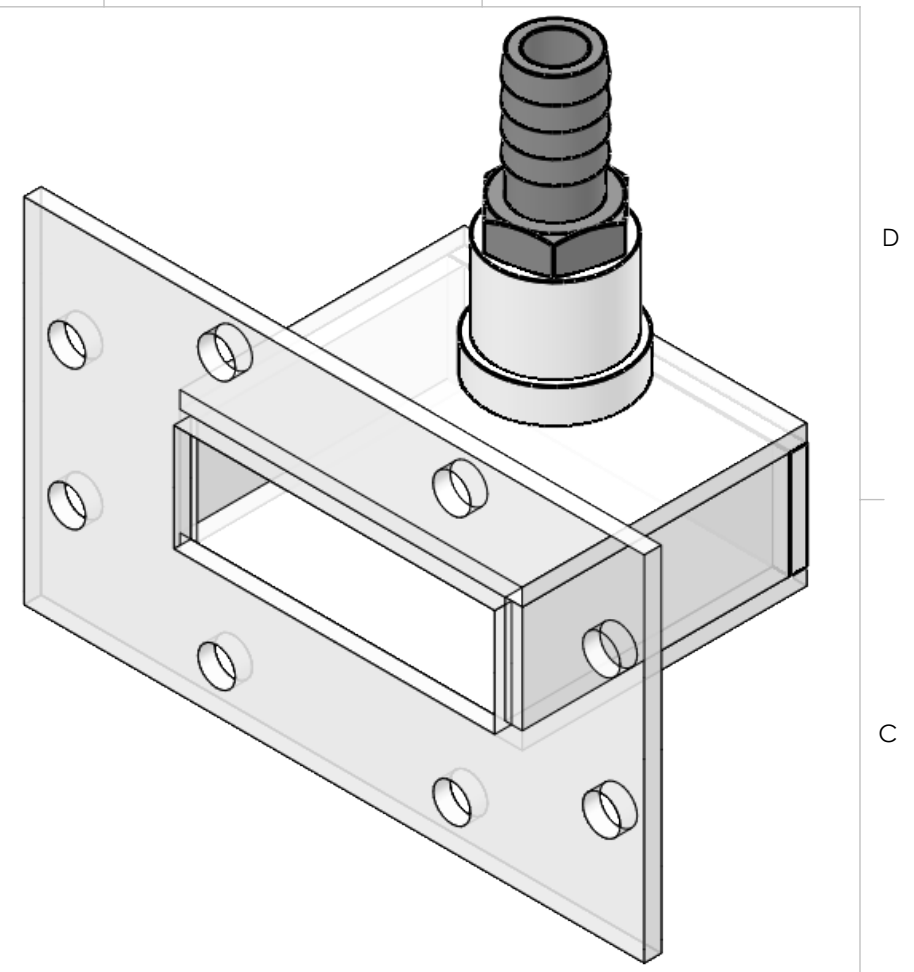
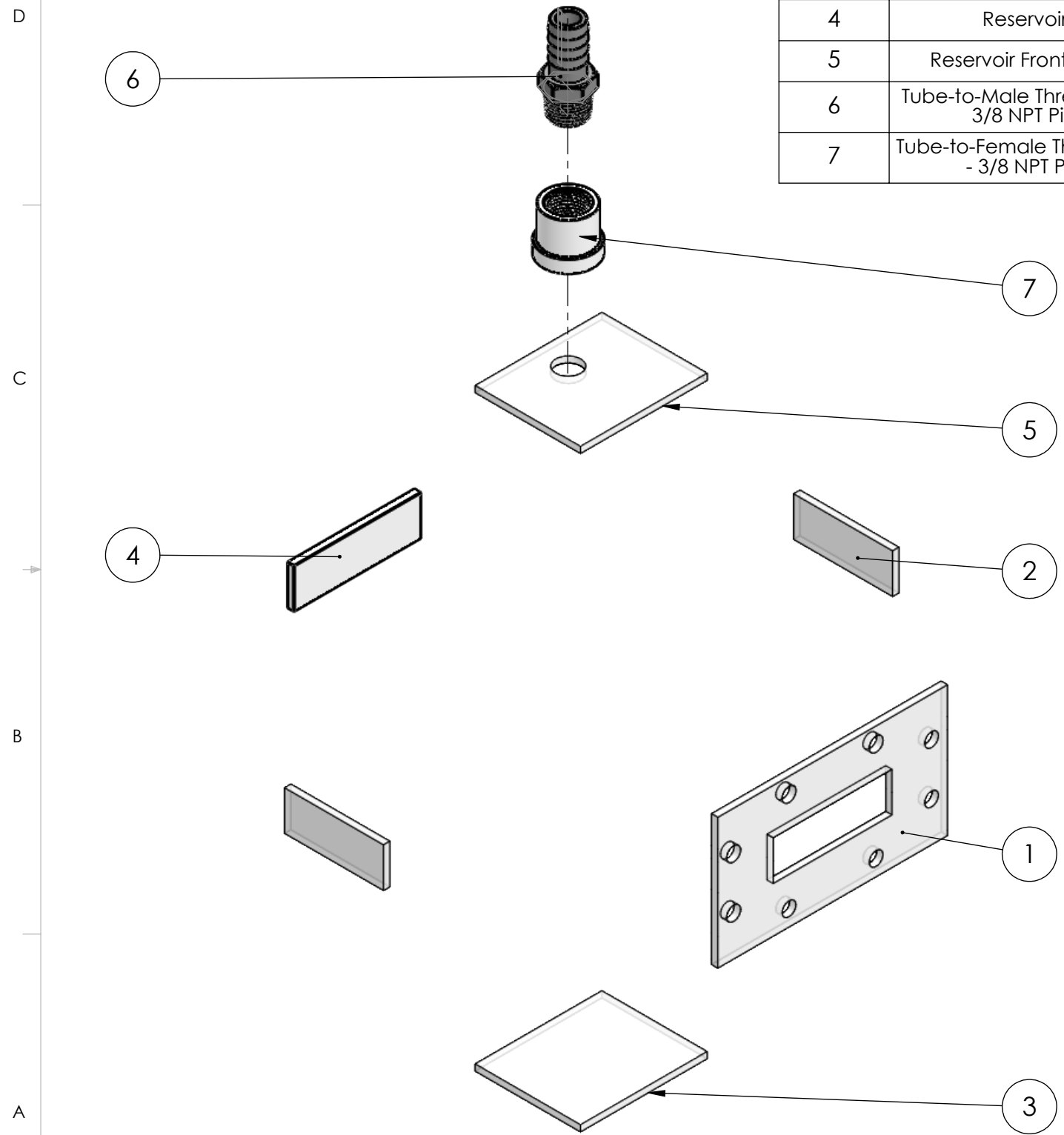


Allen Key 3mm Hex



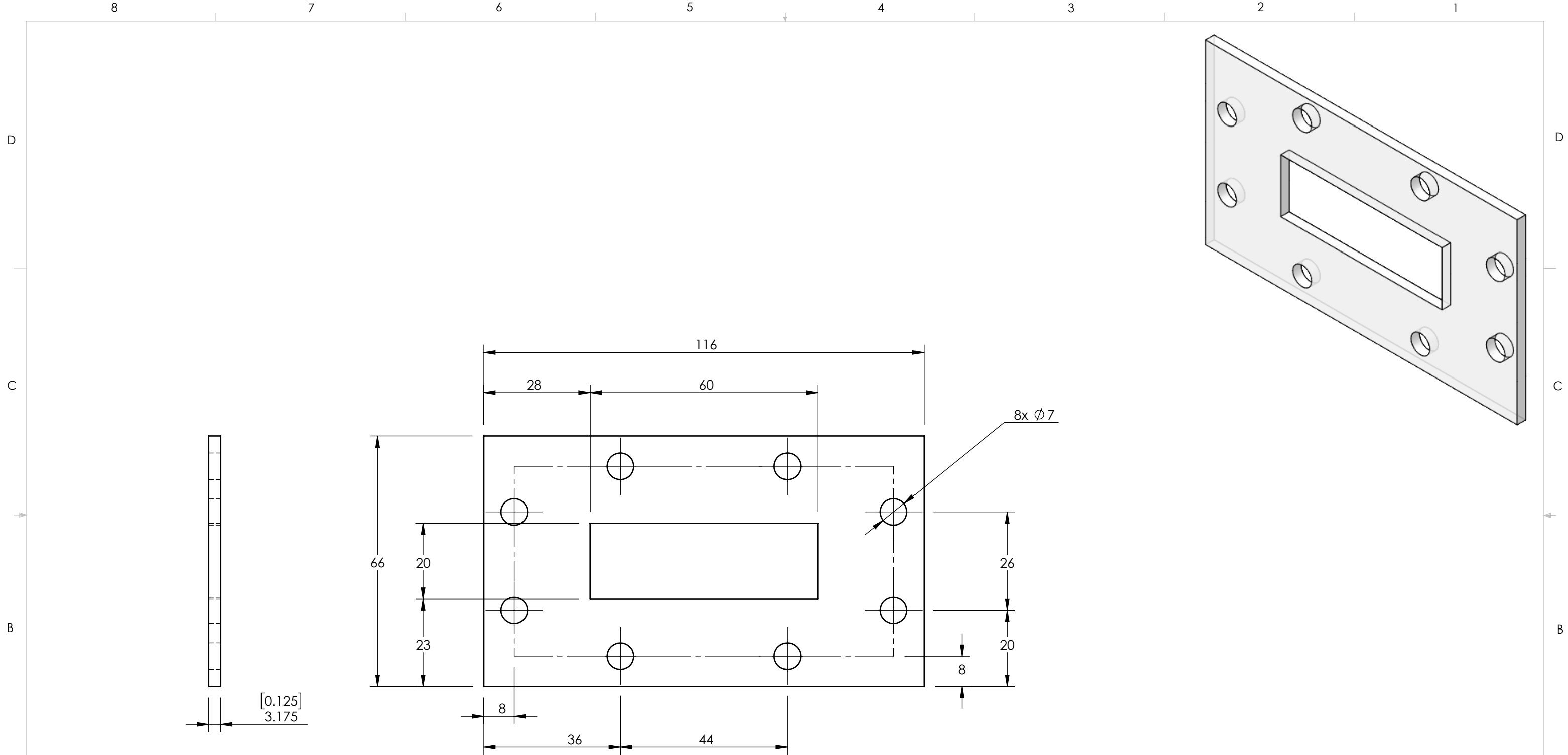
Comments: Part is to be 3D printed with VeroGray in MecE shop	UNLESS OTHERWISE SPECIFIED: DIMENSIONS ARE IN MM TOLERANCES: ANGULAR: $\pm 0.5^\circ$ LINEAR X = $\pm 0.5$ X.X = $\pm 0.1$ X.XX = $\pm 0.05$	DRAWN BY: Daren Wilkinson	 The Department of Mechanical Engineering UNIVERSITY OF ALBERTA	
	 SURFACE FINISH $0.6 \mu\text{m}$ ✓ DO NOT SCALE DRAWING	MATERIAL: VeroGray FILE NAME: Stagescrew	Supervisor: Sina Ghaemi	TITLE: <h1 style="text-align: center;">Screw</h1>
		SIZE <b>B</b>	SCALE: 10:1	REV 1
			SHEET 4 OF 4	

ITEM NO.	DESCRIPTION	MATERIAL	QTY.
1	Reservoir Front	Polycarbonate	1
2	Reservoir Side	Polycarbonate	2
3	Reservoir Front / Bottom 1	Polycarbonate	1
4	Reservoir Back	Polycarbonate	1
5	Reservoir Front / Bottom 2	Polycarbonat	1
6	Tube-to-Male Threaded Fitting - 3/8 NPT Pipe Size	Nylon	1
7	Tube-to-Female Threaded Fitting - 3/8 NPT Pipe Size	Polycarbonat	1




Scale 1:1

Comments: Tube-to-Male Threaded Fitting will be provided by us.	UNLESS OTHERWISE SPECIFIED: DIMENSIONS ARE IN MM TOLERANCES: ANGULAR: $\pm 0.5^\circ$ LINEAR X = $\pm 0.5$ X.X = $\pm 0.1$ X.XX = $\pm 0.025$ SURFACE FINISH $\mu\text{m}$ 0.6 ✓ DO NOT SCALE DRAWING	DRAWN BY: Daren Wilkinson	The Department of Mechanical Engineering UNIVERSITY OF ALBERTA
		MATERIAL:	
FILE NAME: Reservoir Assembly	Supervisor: Sina Ghaemi	SIZE <b>B</b>	REV 1
		SCALE: 1:2	SHEET 1 OF 6



SOLIDWORKS Educational Product. For Instructional Use Only

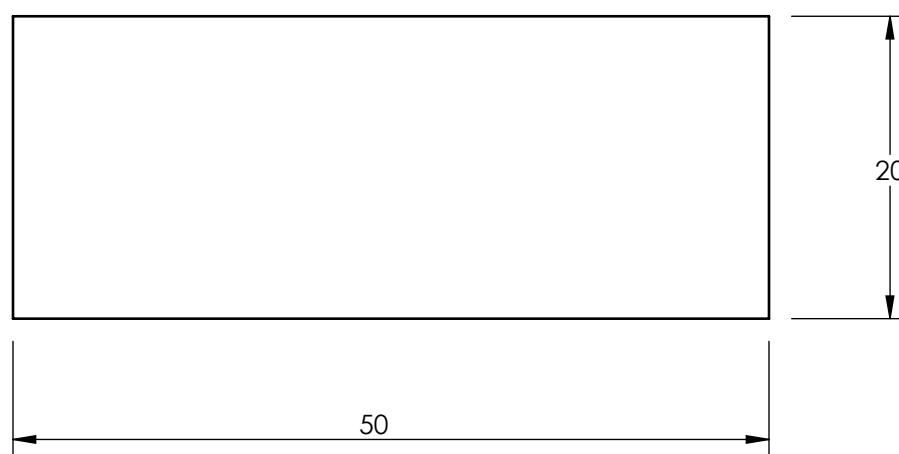
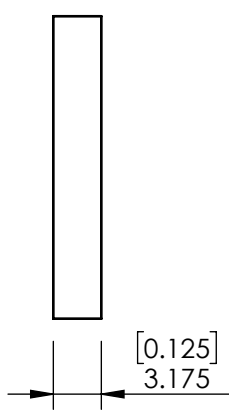
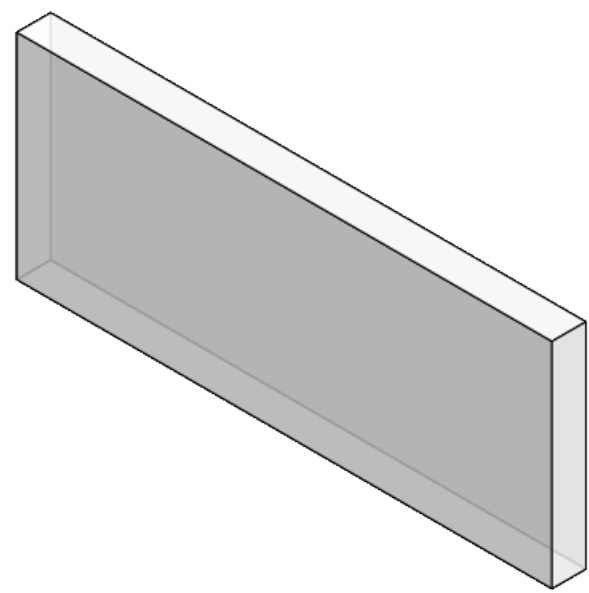
Comments:	UNLESS OTHERWISE SPECIFIED:	DRAWN BY:	 The Department of Mechanical Engineering UNIVERSITY OF ALBERTA	
	DIMENSIONS ARE IN MM TOLERANCES: ANGULAR: $\pm 0.5^\circ$ LINEAR X = $\pm 0.1$ X.X = $\pm 0.1$ X.XX = $\pm 0.025$  SURFACE FINISH $0.6 \mu\text{m}$ ✓ DO NOT SCALE DRAWING	Daren Wilkinson		TITLE: <b>Reservoir Front</b>
MATERIAL:	Polycarbonate	Supervisor:	SIZE <b>B</b>	REV 1
FILE NAME: Reservoir_front		Sina Ghaemi	SCALE: 1:1	
			SHEET 2 OF 6	





8 7 6 5 4 3 2 1

D  
C  
B  
A

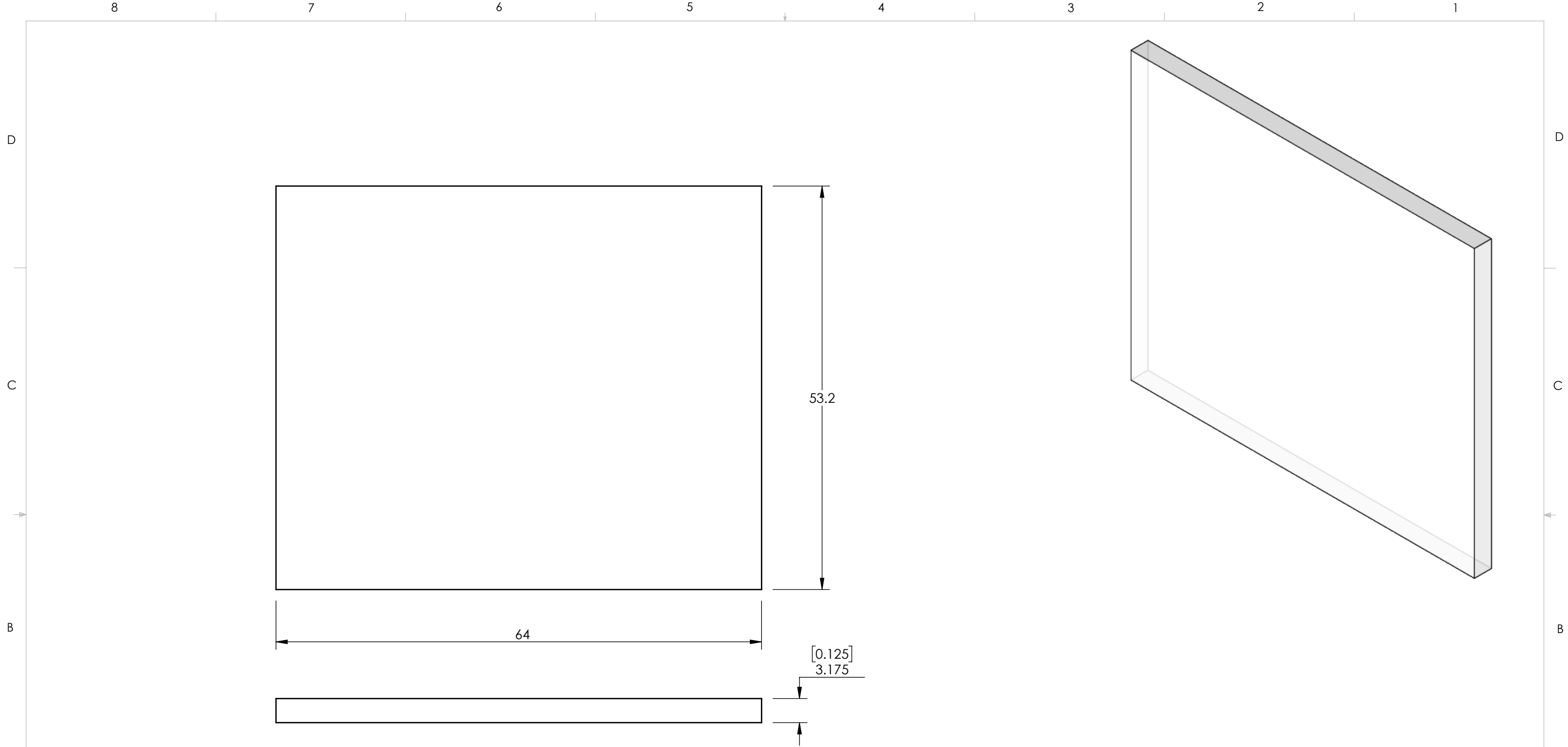
D  
C  
B  
A



SOLIDWORKS Educational Product. For Instructional Use Only

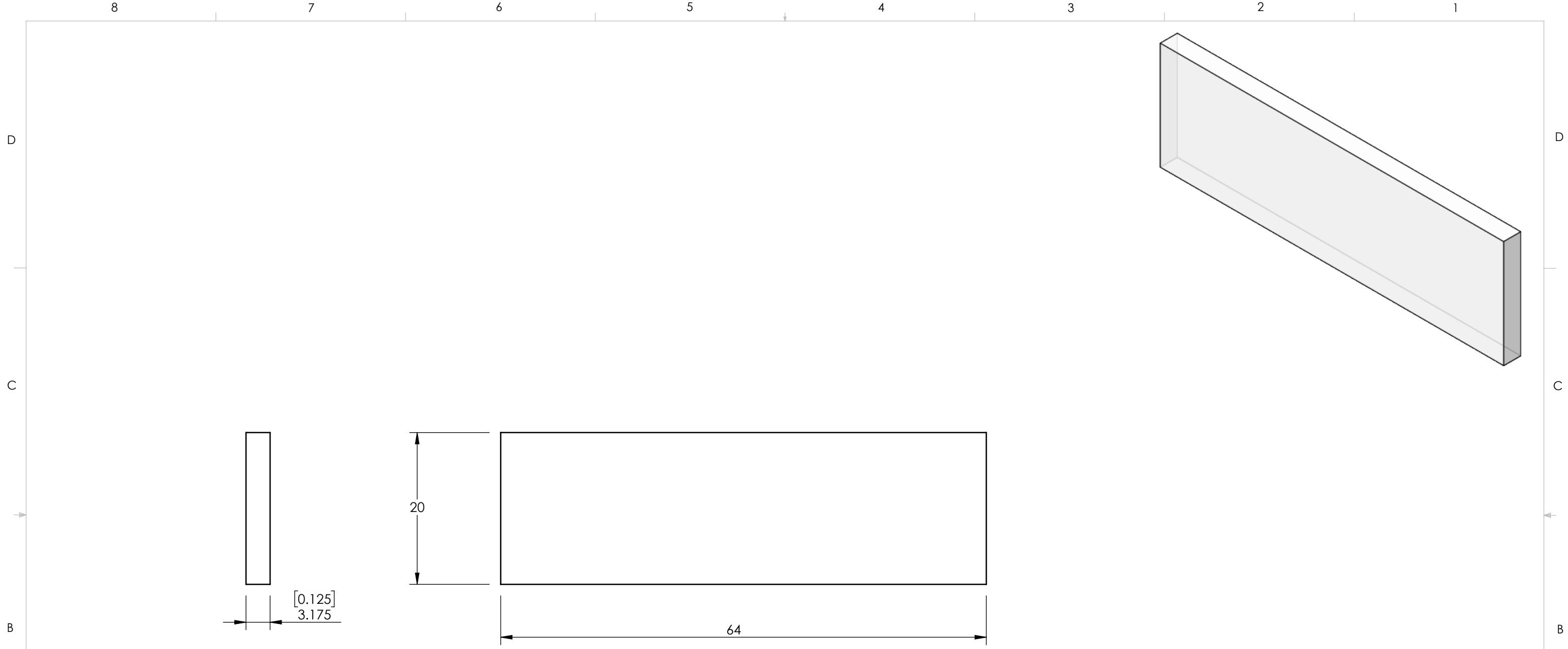
Comments:	UNLESS OTHERWISE SPECIFIED:	DRAWN BY:	The Department of Mechanical Engineering UNIVERSITY OF ALBERTA	
	DIMENSIONS ARE IN MM TOLERANCES: ANGULAR: ± 0.5° LINEAR X = ± 0.1 X.X = ± 0.1 X.XX = ± 0.025  SURFACE FINISH 0.6 μm ✓ DO NOT SCALE DRAWING	Daren Wilkinson	TITLE: <b>Reservoir Side</b>	
 	MATERIAL:	Supervisor:	SIZE	REV
	Polycarbonate	Sina Ghaemi	<b>B</b>	1
FILE NAME: Reservoir_sides			SCALE: 2:1	SHEET 3 OF 6



8 7 6 5 107 4 3 2 1



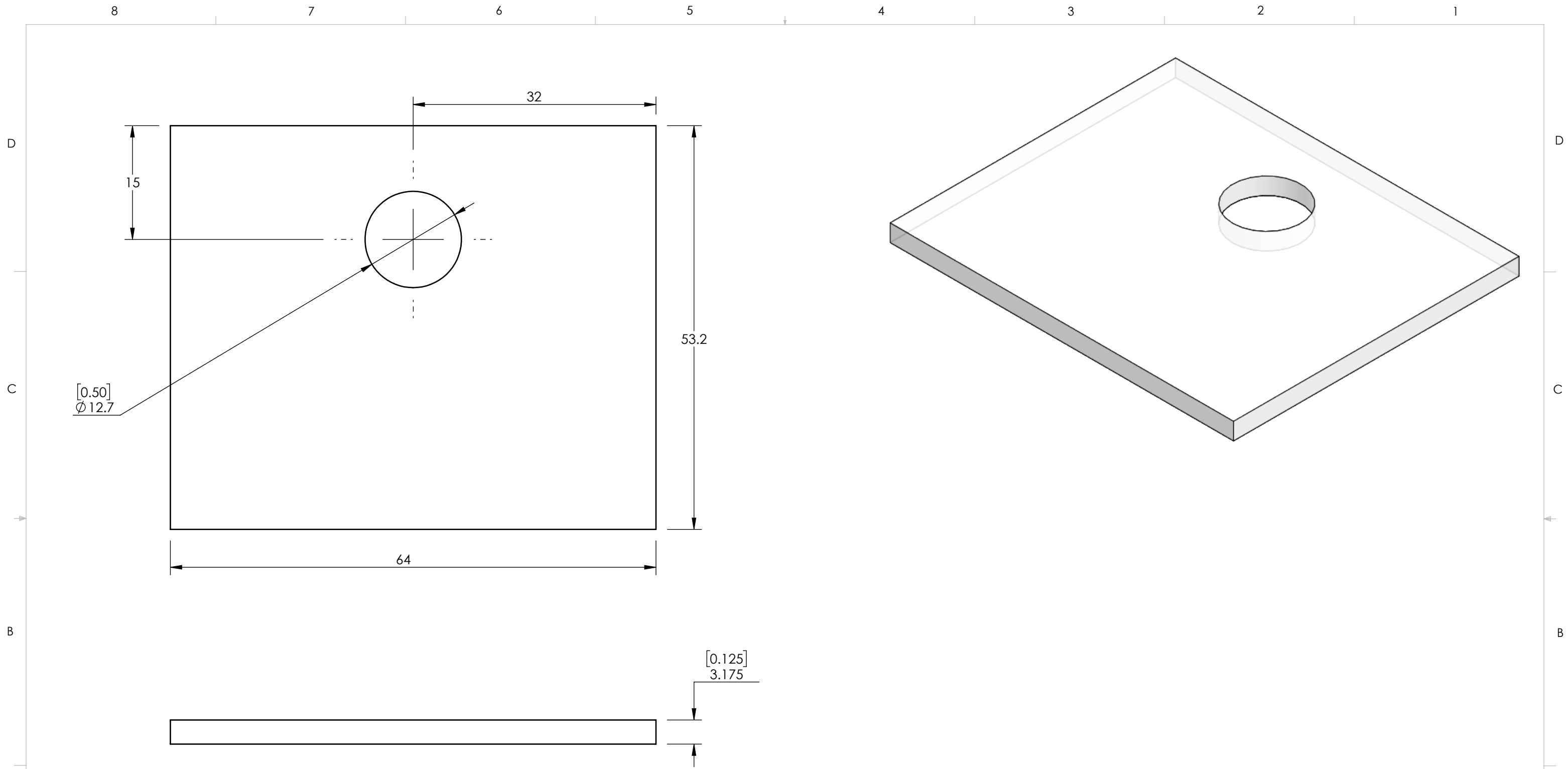
SOLIDWORKS Educational Product. For Instructional Use Only

Comments:	UNLESS OTHERWISE SPECIFIED:	DRAWN BY:	 The Department of Mechanical Engineering UNIVERSITY OF ALBERTA	
	DIMENSIONS ARE IN MM TOLERANCES: ANGULAR: $\pm 0.5^\circ$ LINEAR X = $\pm 0.1$ X.X = $\pm 0.1$ X.XX = $\pm 0.025$  SURFACE FINISH $0.6 \checkmark$ $\mu\text{m}$ DO NOT SCALE DRAWING	Daren Wilkinson		TITLE: Reservoir Top / Bottom 1
	MATERIAL:	Supervisor:	SIZE	REV
FILE NAME:	Polycarbonate	Sina Ghaemi	<b>B</b>	1
108	4	3	SCALE: 2:1	
			SHEET 4 OF 6	






Comments:	UNLESS OTHERWISE SPECIFIED:	DRAWN BY:	 The Department of Mechanical Engineering UNIVERSITY OF ALBERTA	
	DIMENSIONS ARE IN MM TOLERANCES: ANGULAR: $\pm 0.5^\circ$ LINEAR X = $\pm 0.1$ X.X = $\pm 0.1$ X.XX = $\pm 0.025$  SURFACE FINISH $0.6 \mu\text{m}$ ✓ DO NOT SCALE DRAWING	Daren Wilkinson		TITLE: <b>Reservoir Back</b>
	MATERIAL:	Supervisor:	SIZE	REV
FILE NAME:	Polycarbonate	Sina Ghaemi	<b>B</b>	1
Reservoir_back			SCALE: 2:1	SHEET 5 OF 6

SOLIDWORKS Educational Product. For Instructional Use Only



SOLIDWORKS Educational Product. For Instructional Use Only

Comments:	UNLESS OTHERWISE SPECIFIED:	DRAWN BY:	 The Department of Mechanical Engineering UNIVERSITY OF ALBERTA	
	DIMENSIONS ARE IN MM TOLERANCES: ANGULAR: $\pm 0.5^\circ$ LINEAR X = $\pm 0.1$ X.X = $\pm 0.1$ X.XX = $\pm 0.025$  SURFACE FINISH $\mu\text{m}$ 0.6 ✓ DO NOT SCALE DRAWING	Daren Wilkinson		TITLE: Reservoir Top / Bottom 2
 	MATERIAL:	Supervisor:	SIZE	REV
FILE NAME:	Polycarbonate	Sina Ghaemi	<b>B</b>	1
Reservoir_t_b_2			SCALE: 2:1 SHEET 6 OF 6	

## 9 Appendix B – Other works

This section will present works were that were attempted during the studies but were not able to be investigated further for various reasons.

### 9.1.1 Superhydrophobic surfaces

Patterned microposts with gas fractions of 80%, 85%, and 90% were fabricated at the University of Alberta Nanofab facility. The posts were coated with Trichloro(1H,1H,2H,2H-perfluorooctyl)silane in vacuum chamber to increase hydrophobicity. The patterned posts were also etched to provide needle-like structures on the top which can be seen in Figure 49. Both sets, etched or not, had contact angles of  $144^\circ$  -  $148^\circ$  with higher gas fractions performing slightly better. The drag reducing performance of the surfaces were to be tested, however, the surfaces could not support an air layer at pressures  $> 300$  Pa. The surfaces also became wetted after a short duration and lost hydrophobicity after becoming reaching the wetted state several times. This was believed to be due to the hydrophobic coating only bonding to the outer layer of molecules of the surface and if the bond was broken that portion was no longer hydrophobic. As the literature suggested, the surfaces with the needle-like structures held an air layer longer and at slightly higher pressures than the surfaces without the etching.

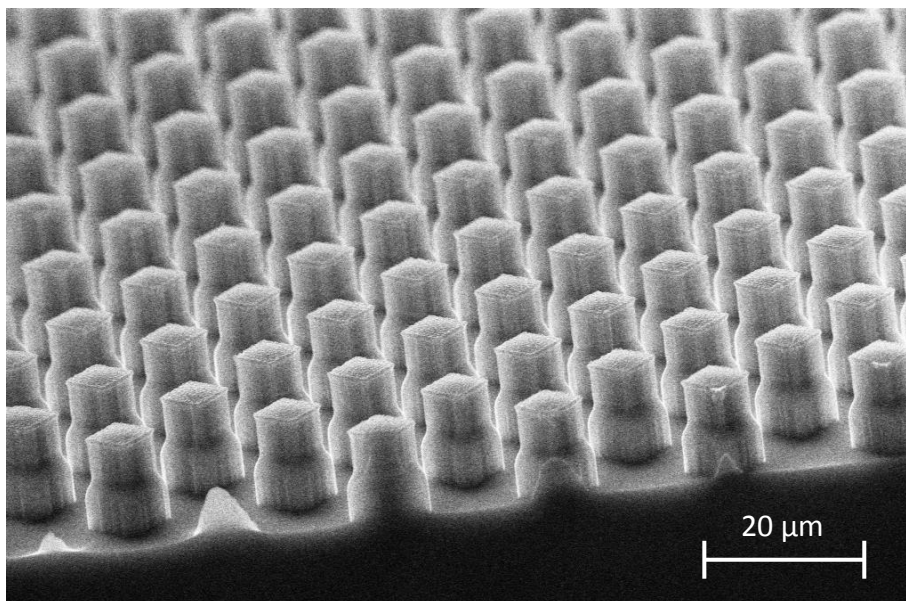


Figure 48: A SEM image of microposts with a gas fraction of 90%.

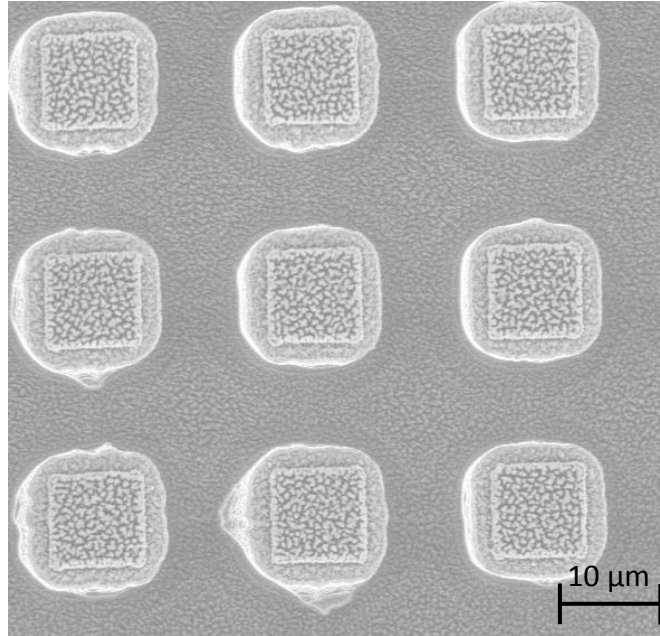


Figure 49: A SEM image of etched microposts with a gas fraction of 90%.

### 9.1.2 Turbulent statistics analysis

A goal of the second portion of the research was to analyze the turbulent statistics of the four SHSs and see the influence of the surface roughness. The turbulent statistics are shown in Figure 50 normalized by  $u_{\tau 0}$ . It can be seen from Figure 50 below that the magnitude of the turbulent statistics for  $v^2$  was small and therefore was susceptible to noise. The reason for the increase of  $v^2$  over SHS<sub>0.18</sub> compared to the other surfaces was not found. This could be from processing in Davis or caused from the experimental setup when that surface was tested. The convergence of the data was confirmed to see if a sufficient number of images were taken. The images collected were over a 1200  $\mu$ s span and fluctuations of the pump would mean more images are required to before reaching convergence. Collecting smaller image sets over a longer experimental time would also reduce the noise caused by experimental variance such as pump fluctuations. The convergence plot at  $y^+ = \lambda$  over SHS<sub>0.35</sub> for  $u^2$  can be seen in Figure 51. It was evident that the turbulent statistics converged within the number of images collected over the acquisition time to the mean value of 8.47.

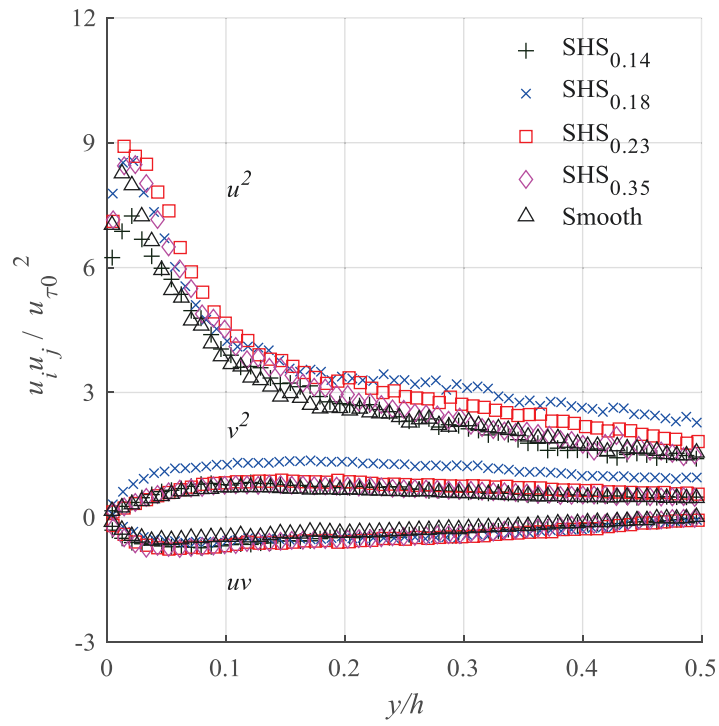


Figure 50: Turbulent statistics over SHS<sub>0.35</sub>, SHS<sub>0.23</sub>, SHS<sub>0.18</sub>, and SHS<sub>0.14</sub>.

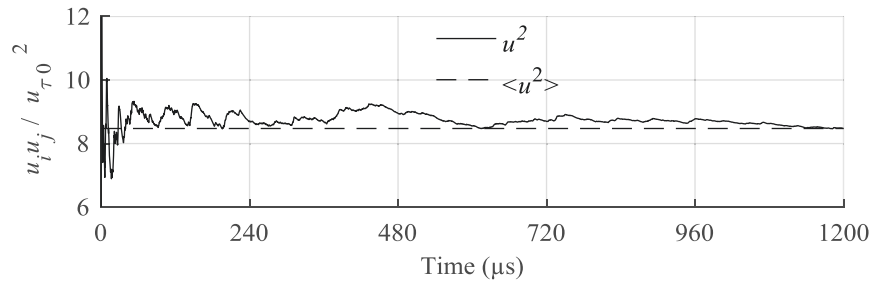


Figure 51: Convergence plot of the turbulent statistics at  $y^+ = \lambda$  over SHS<sub>0.35</sub>.